Design and Operation of a Counter-Rotating Aspirated Compressor Blowdown Test Facility

by
David V. Parker

B.S., Mechanical Engineering (2003)
University of New Hampshire

Submitted to the Department of Aeronautics and Astronautics in partial fulfillment of the degree of

Master of Science

at the
MASSACHUSETTES INSTITUTE OF TECHNOLOGY

June 2005

Author .....
Department of Aeronautics and Astronautics
May 20, 2005

Certified by .....
Alan H. Epstein
R.C. Maclaurin Professor of Aeronautics and Astronautics
Thesis Supervisor

Certified by .....
Jaime Peraire
Professor of Aeronautics and Astronautics
Chair, Committee on Graduate Students

Design and Operation of a Counter-Rotating Aspirated Compressor Blowdown Test Facility

by
David V. Parker

Submitted to the Department of Aeronautics and Astronautics on
May 20, 2005 in partial fulfillment of the degree of
Master of Science

Abstract

A unique counter-rotating aspirated compressor was tested in a blowdown facility at the Gas Turbine Laboratory at MIT. The facility expanded on experience from previous blowdown turbine and blowdown compressor experiments. Advances in thermocouple and facility designs enabled efficiency estimates through total temperature and total pressure measurements. The facility was designed to provide at least 100 ms of available test time, approximately a factor of five greater than previous blowdown compressor facilities.

The adiabatic core efficiency of the compressor was estimated with an uncertainty of 0.8% and the corrected flow was estimated with an uncertainty of 1.0%. The compressor was tested at several operating conditions and two speed lines were partially mapped. The maximum measured total pressure ratio across the two stages was 3.02 to 1. The measured adiabatic efficiency for that point was 0.885.

The span-wise total pressure, total temperature, and efficiency profiles were compared to the predicted profiles for runs with the corrected speeds of the two rotors at 90% of design and 100% design. There appears to be reasonable agreement between the predictions and the measurements.

Thesis Supervisor: Dr. Alan H. Epstein
Title: R.C. Maclaurin Professor of Aeronautics and Astronautics

Acknowledgments

The author would like to thank Prof. Alan H Epstein, Dr. Gerald Guenette, and Prof. Jack Kerrebrock for the opportunity to work on this project. Also, they were invaluable resources for insight and guidance when looking for solutions to problems. Without their experience with blowdown facilities this project would not have succeeded. Also, Dr. Fritz Neumayer and Dr. Ali Merchant deserve thanks for their work on the data acquisition system and the rotors, respectively.

Thanks to JF Onnee for spending long days working in the lab, thinking through problems, and getting through this process.

A special thanks to Jack Costa, James Letendre, and Victor Dubrowski for their tireless work in the lab. The instruments were partially the result of many hours Mr. Costa spent staring through the microscope soldering wires. Similarly, Mr. Dubrowski's skills with a Bridgeport and lathe where highly valued while manufacturing the instruments. Finally, Mr. Letendre showed the author how to safely and effectively work in the lab.

On a personal note the author would like to thank his family, who have always supported and pushed him; Debbie, she is an amazing blessing and support; and his church for the friendship and community that they have provided.

Finally, the author would like to thank Dr. S. Walker, program manager at the Defense Advanced Research Program Agency, for funding this research.

Table of Contents

Table of Figures

Table of Tables

Nomenclature

η	adiabatic efficiency
ρ	density
δ	fraction of mass flow
γ	ratio of specific heats
σ	rotor solidity
Ω	rotor speed (rad/sec)
κ	thermal conductivity
π	total pressure ratio
μ	viscosity
τ_b	blowdown time constant
τ_c	total temperature ratio
A_C	area of annulus entering compressor
C_P	specific heat at a constant pressure
C_V	specific heat at a constant volume
D	diameter
D_F	diffusion factor
M	Mach number
$\dot{m}$	mass flow
N	rotor speed (Hz)
N_C	corrected speed
P	power
P_T	total pressure
P_{T_ref}	reference total pressure (1 atm)
R_{air}	gas constant of air
Re	Reynolds' number
Rg	gas constant of the gas mixture
T_T	total temperature
T_{T_ref}	reference total temperature (288 K)
V	volume
v	velocity
W_C	corrected mass flow

1 Introduction

1.1 Motivation of Work

In axial compressors the total pressure rise across a stage is directly related to the wheel speed and the turning of the flow. As the wheel speed is increased the velocity of the flow relative to the blade increases, increasing the Mach number. Increasing the Mach number too much can lead to unacceptable losses in efficiency. The limit on turning the flow is typically related to boundary layer separation [1]. A useful measure for relating the pressure rise, relative velocities, and turning in a compressor is the Diffusion Factor, first defined by Lieblein et al. [1] as:

$$D = 1 - \frac{V_2}{V_1} + \frac{|v_2 - v_1|}{2 \cdot \sigma \cdot V_1} \qquad \text{Eqn (1.1) [2]}$$

In equation 1.1 station '1' is entering the blade row and station '2' is exiting the blade row; V_i is the velocity relative to the blade, v_i is the circumferential velocity, and σ is the solidity of the blade row. The diffusion factor can be thought of as a relationship between the maximum velocity on the suction surface of the blade and the velocity of the fluid at the trailing edge of the blade. Losses increase dramatically when the diffusion factor exceeds 0.6 [2, 3].

It has been recognized since at least as early as 1950 that counter-rotation is a method for dramatically increasing the turning of the flow across the rotor. The fundamental problem with counter-rotation is that it results in supersonic relative Mach numbers in the second rotor. The advantage of counter-rotation is increasing the pressure ratio for the two stages; or the pressure ratio of current technology can be achieved while lowering the wheel speeds of the two rotors. Recently, reducing engine noise has received attention. A significant component of the noise generated by engines comes from the first stage fan. There has been a push within industry to reduce fan noise by reducing wheel speed through counter-rotation [4]. In the early 1950's Curtiss-Wright attempted, unsuccessfully, to produce a highly loaded counter-rotating compressor [1].

Since the mid 1990s investigators at MIT have been investigating the use of aspiration, removing low-momentum flow from boundary layers, to increase the pressure ratio per stage and extend the diffusion factor design space [6]. To date three aspirated compressors have been built and tested; one 'low-speed stage' that was tested at the MIT Gas Turbine Lab, one 'high-speed stage' that was tested at the NASA-Glenn Research Center, and a counter-rotating fan stage that is the subject of this current work.

1.2 Contents of This Work

One goal for this project was to measure the adiabatic efficiency of a counter-rotating aspirated compressor using a blowdown test facility. To accomplish this meant designing a new facility, rotors, and instruments. This thesis discusses the design of the facility (Chapters 2-3), the design and manufacture of the two rotors (Chapter 4), a cursory

treatment of the instrumentation and data acquisition systems (Chapter 5), and the results from the first series of tests (Chapter 6). Chapter 7 contains recommendations for future work. For details about the facility instrumentation consult "Aerodynamic Performance Measurements in a Counter-Rotating Aspirated Compressor" [5].

Some of the content of this thesis is the work of the author while other sections are descriptions of other people's work that are necessary for a comprehensive discussion of the facility. While the facility was being designed the author was primarily responsible for the design of the flywheels and pressure screen. The author also provided support designing the remainder of the test section. The author worked on a team to establish the mechanical design of the Inlet Guide Vanes, Rotor One, and Rotor Two. Interfacing with the manufacturer and managing the production of the bladed components was spearheaded by author. The author designed the total pressure rakes and manufactured the profiles for both the total pressure rakes and the total temperature rakes. Finally the author developed a system to reduce the data to engineering units and then analyze the data.

2 Experimental Facility Design

Short duration blowdown tests of compressors and turbines have been occurring at the Gas Turbine Laboratory at MIT since the early 1970s. Much has been learned about blowdown test dynamics and the solutions to problems associated with these test facilities. This knowledge base was heavily relied upon while designing the Blowdown Counter-Rotating Aspirated Compressor Facility (CRAspC), however, counter-rotation and aspiration presented new problems to be solved on this project.

Figure 2.1 is a basic sketch of the facility. The facility consists of the supply tank (A); the fast-acting valve (B); the pressure screen (C); the rotating assemblies, with consist of motors, inertias, and rotors (D,E); the throttle (F); and the dump tank(G). The order of operations for a blowdown test is that the entire facility is evacuated, then the valve is closed and the supply tank is filled to an initial pressure. The rotors are then brought to a set speed and the valve opens in less than 50 ms. Approximately 100 ms later the test is finished when the temperature of the gas mixture drops below 250° K.

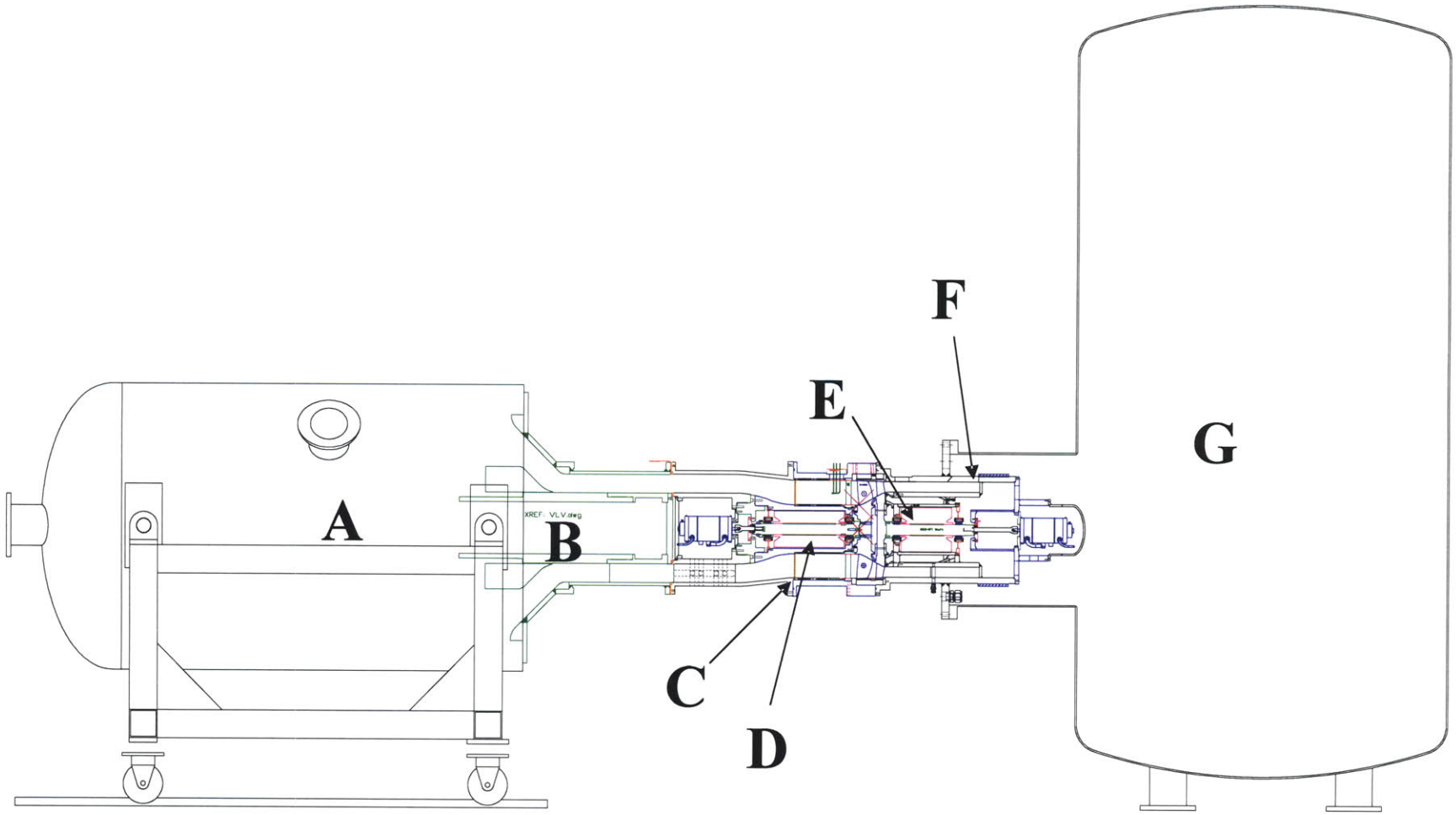

Figure 2.1: Sketch of CRAspC Blowdown Test Facility

This chapter discusses the underlying principles in the design of a blowdown compressor facility. Section 2.1 looks at the specific requirements of this facility. Section 2.2 discusses the non-dimensional groupings of variables that are used for scaling the facility and Section 2.3 discusses the some of the physical constraints on the facility that influenced the scales that the compressor was designed to.

2.1 Facility Requirements

One goal of this project was to accurately measure the important parameters of a counter-rotating aspirated compressor that would be appealing to industry. Economics and schedule dictated that the test be conducted in a blowdown facility. The requirements of the facility are enumerated below.

1. The facility must be scaled such that all pertinent non-dimensional parameters are matched during the test.
2. Non-Dimensional parameters must be constant during the test period.
3. The test must have a relatively long duration (400-500 ms) so that efficiency can be precisely measured with total temperature probes.
4. The facility was to be designed in such a manner that instrumentation capable of measuring more detailed flow phenomenon could be added at a later date.
5. All operational stresses must be kept within safe limits.
6. The compressors must be un-shrouded.

2.2 Facility Scaling Parameters

In a conventional steady-state compressor test facility inlet and exit conditions are held essentially constant. Inlet total temperature, total pressure, and mass flow do not vary (unless some dynamic phenomena is specifically investigated). The nature of blowdown experiments dictate that these parameters vary throughout the duration of the test. Previous work, by many investigators, has shown that characteristics of the fluid flow within the compressor are dictated not by dimensional, but rather, by non-dimensional parameters. These parameters are listed in Table 2.1. In blowdown experiments the facility is designed with the intent that these non-dimensional parameters, with the exception of Reynolds Number, remain relatively constant during the test. This section discusses how different facility dimensional variables affect the behavior of non-dimensional parameters over time during a test. The facility was scaled based on the predicted performance of the compressor at the design point. The impact of this scaling on the off-design performance is discussed in Section 6.2.

Table 2.1 Important Non-Dimensional Parameters for Scaling Test Facility

Parameter	Formula	What It Measures
Corrected Flow	$Wc = \dfrac{\dot{m} \cdot \sqrt{\dfrac{R_g \cdot T_T}{R_{air} \cdot T_{T\_Ref}}}}{A \cdot \dfrac{P_T}{P_{T\_Ref}}}$	mass flow through compressor corrected to standard day conditions
Corrected Speed	$Nc = \dfrac{N \cdot \pi \cdot D}{\sqrt{R_g \cdot T_T}}$	tip speed relative to speed of sound
Ratio of Specific Heats	$\gamma = \dfrac{C_p}{C_v}$	defines 1-D compressible flow relationships
Mach Number	$M = v/c$	velocity of flow relative to speed of sound
Reynolds Number	$\mathrm{Re} = \dfrac{\rho \cdot v \cdot D}{\mu}$	momentum of the fluid relative to the viscosity

2.2.1 Matching Corrected Flow and Mach Number

For an ideal gas with constant γ corrected flow can be expressed as:

$$Wc = f(M,\gamma) \cdot \frac{P_{T\_Ref}}{\sqrt{R_g \cdot T_{T\_Ref}}}$$

$$f(M,\gamma) = \sqrt{\gamma} M \cdot \left(1 + \frac{\gamma - 1}{2} \cdot M^2\right)^{-\frac{\gamma+1}{2(\gamma-1)}}$$

Eqn (2.1) [7]

The corrected flow in the facility is set with a choked throttle between the test section and the dump tank. As long as the flow remains choked the Mach number is constant making the corrected flow constant. Therefore, one significant influence on the available test time is the size of the dump tank. The larger the tank the longer it will be before the pressure in the dump tank rises above the critical pressure where the orifice unchokes. The throttle is designed so that the area can be changed between runs. Before the first test CFD compressor models and an estimate of the throttle discharge coefficient are used in combination with steady and unsteady models (both of which assume the compressor operates at a specific operating point from the CFD) of the facility to set a nominal throttle position. Analysis after the run allows the investigators to view where the compressor operated and adjust the throttle accordingly. A quasi-steady lumped parameter model of the facility was developed to investigate how changing different variables affected the entire system. Figure 2.2 shows some of the results of the unsteady model for the compressor design point. It is easy to see from Equation 2.1 that if the corrected flow is constant then the inlet Mach number also remains constant.

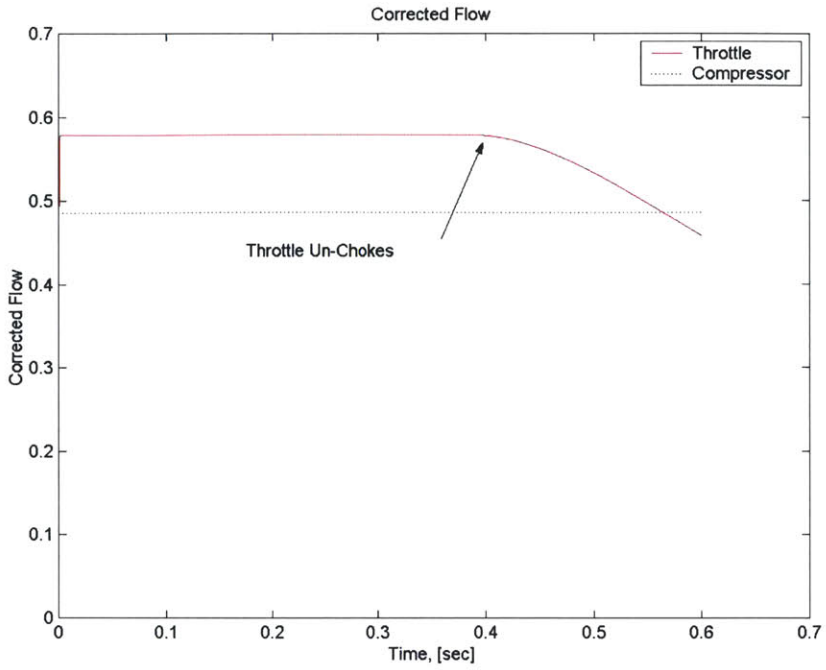

Figure 2.2: Estimated Corrected Flow During Blowdown

2.2.2 Matching Corrected Speed

Taking the derivate of Corrected Speed with respect to time shows that:

$$\frac{dN_C}{dt} = \frac{D}{\sqrt{R_g T_T}} \cdot \frac{dN}{dt} - \frac{ND}{2\left(R_g T_T\right)^{3/2}} \cdot \frac{dT_T}{dt} \qquad \text{Eqn (2.2)}$$

Thus to keep the corrected speed constant during the test it is evident that:

$$\frac{dN}{dt} = \frac{N}{2R_g T_T} \cdot \frac{dT_T}{dt} \qquad \text{Eqn (2.3)}$$

Assuming an isentropic expansion within the tank and choked flow across the pressure screen yields the total temperature of the flow as a function of time expressed by Equation 2.4. The derivation for this equation is in Appendix A.

$$T_T(t) = T_T(0)(1 + t/\tau_b)^{-2} \qquad \text{Eqn. (2.4)}$$

Where τ_b is the blowdown time constant and defined by:

$$\tau_b = \left[\left(\frac{\gamma - 1}{2}\right)\frac{W_{Sc} A_{Sc} \sqrt{R_g T_T(0)}}{V_S}\right]^{-1} \qquad \text{Eqn. (2.5)}$$

V_S = Supply Tank Volume
W_{Sc} = Corrected flow through pressure screen
A_{Sc} = Open area of pressure screen

The power consumed by each compressor stage can be expressed as:

$$P = \dot{m} \cdot C_P \cdot T_T \cdot (\tau_c - 1) = W_{Sc} A_{Sc} P_T \frac{\gamma \sqrt{R_g T_T}}{1+\gamma} (\tau_c - 1)$$

Eqn. (2.6)

Power consumption is related to deceleration of the rotor by:

$$P = -I \cdot N \frac{dN}{dt}$$

Eqn. (2.7)

Solving for the compressor speeds leads to complicated expressions involving the corrected flow, screen open area, blowdown time constant, and inertia. This analysis was previously done for a single rotor by J.L. Kerrebrock [8]. His work showed that the corrected flow cannot be held constant but careful selection of design parameters, primarily the inertias of the rotational systems, can keep the deviation of the corrected speed from the design corrected speed within acceptable limits. Numerical models were used to examine how modifying parameters changed the behavior of the corrected speed of the two rotors. Figure 2.3 shows the estimated corrected speed from the unsteady lumped parameter model for a test of the compressor at the design point.

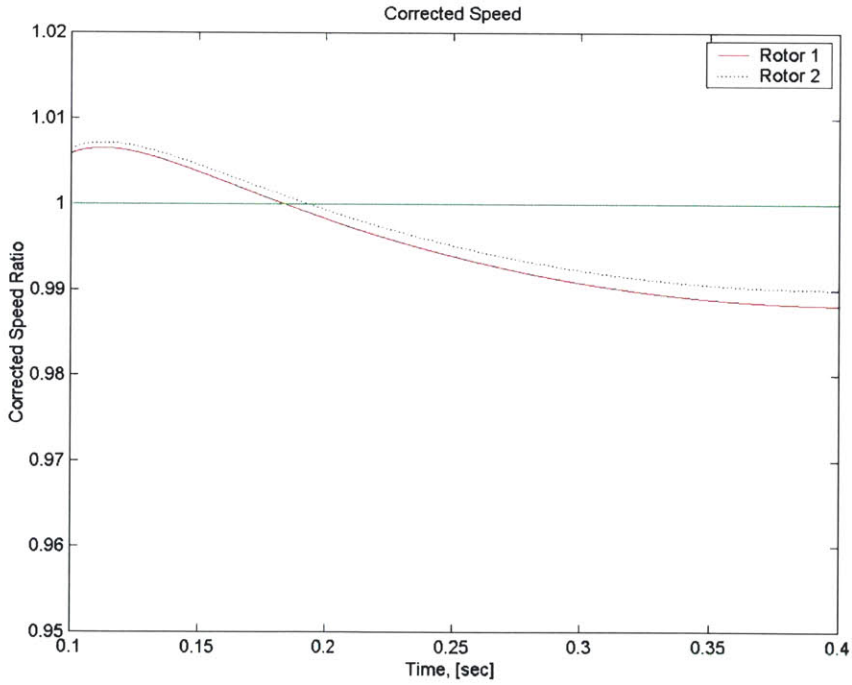

Figure 2.3: Estimated Variation in Corrected Speed During Blowdown

2.2.3 Matching Ratio of Specific Heats

The ratio of specific heats (γ) of the working gas determine the 1-D compressible flow relationships that govern the fluid. The simplest way to match the working gas to the design gas is to use air. Looking at the equation for corrected speed (in Table 2.1) shows

that increasing the molecular weight of the working gas lowers the physical rotor speed for a given corrected speed. Operating the facility at lower physical speeds lowers stresses in the rotors and flywheels. A mixture of carbon dioxide and argon can match the γ of air at a modest price and is 44% heavier than air. Using this mixture there is a concern is that temperature of the supply tank not drop below 220 K during blowdown because of concerns that the CO_2 might solidify. It is also important to note that the mixture ratio is set so that at standard day conditions the ratio of specific heats of the mixture matches that of air. This value changes 2% with the changing temperature across the compressor.

2.2.4 Matching Reynolds' Number

As mentioned earlier Reynolds' number cannot be held constant during the blowdown. It is entirely dependant on the density and velocity into the compressor. Above a certain value changes in Reynolds' number have small impacts on compressor performance. The way to increase the Reynolds' number is to increase the initial supply tank pressure. The initial supply tank pressure is linked to the inertia of the two rotating systems by Equation 2.8, thus along with the benefit of longer test times increasing the available inertia also increases the Reynolds' number.

2.3 Facility Packaging

As shown above, for a given compressor design, there are a limited number variables available to adjust the scaling and maximize available test time. These variables are initial supply tank pressure, supply and dump tank volume, rotational inertia, and throttle area. Throttle area and initial pressure are varied from test to test while volume and inertias are fixed. Selecting these parameters such that they could be packaged in a realizable manner proved to be challenging.

2.3.1 Supply Tank Sizing

Early in the program it was decided to make a minimum number of modifications to the existing GTL Blowdown Turbine Facility because of schedule and a desire for longer test times. The intent was to focus solely on building a new test section. Analysis showed that the blowdown time constant (τ_b) of the Blowdown Turbine Facility would be about four times greater than τ_b of the Blowdown Compressor Facility. Further analysis showed that this configuration would require inertias nearly three times larger than those used in the final design. These simply could not be packaged within the test section so a smaller supply tank was purchased.

2.3.2 Fast-Acting Valve Area

The Fast-Acting Valve separates the test section and dump tank (maintained at vacuum) from the supply tank (at initial pressure) during the spin-up of the rotors then opens

quickly providing a smooth expansion path from the supply tank to the inlet of the compressor. The minimum area of this expansion path is less than the minimum area of the compressor. This means that there would be very high velocity flow within the valve leading to large boundary layers and losses. In order to lower the fluid velocity in the valve (and increase the initial pressure in the supply tank) a screen was placed between the compressor inlet and the valve. This lowers the Mach number in the valve and increases the pressure in the supply tank, improving the operability of the fast-acting valve. The influence of supply tank pressure on the fast-acting valve is described in Section 3.2.

2.3.3 Fitting Flywheels within the Flow path

It was decided to connect the rotor, flywheel, and motor by one shaft because gearing introduces unwanted dynamics to the system. This dictated that the flywheels had to fit inside the inner diameter of the flow path. When one notes that inertia scales as radius to the fourth power it is easy to see that this maximum diameter is a severe constraint on the inertia and ultimately a limit on available test time. Inertia can also be modified, to first order, by changing the length and density. Increasing inertia through length is limited by the shaft and trying to keep the frequency of its first bending mode safely above the operating speed. Increasing the density is limited by available materials and the strength properties of those materials. Section 3.4.2 describes attempts to maximize inertia by using a high-density tungsten nickel alloy.

3 Detailed Facility Description

This chapter discusses the some of the details of the facility. Credit must be given to Dr. J.L. Kerrebrock, Dr. G.R. Guenette, and Prof. A.H. Epstein and others who pioneered blowdown test facilities. Without the experience of those investigators this facility could not have been fabricated on the time scale that it was. Elements of this facility that were not part of other blowdown facilities are the pressure screen and the inertia elements.

The final facility design consisted of supply and dump tanks; gas bottles, vacuum pumps, and a piping system; and a separate test section for each rotor. The tanks and test sections sit on a track system. When bolted together their centerlines are aligned within 0.003 inches and the entire facility can hold a vacuum of better than 100 millitorr, with the vacuum pump running. The Blowdown Counter-Rotating Aspirated Compressor Facility is shown in Figure 3.1

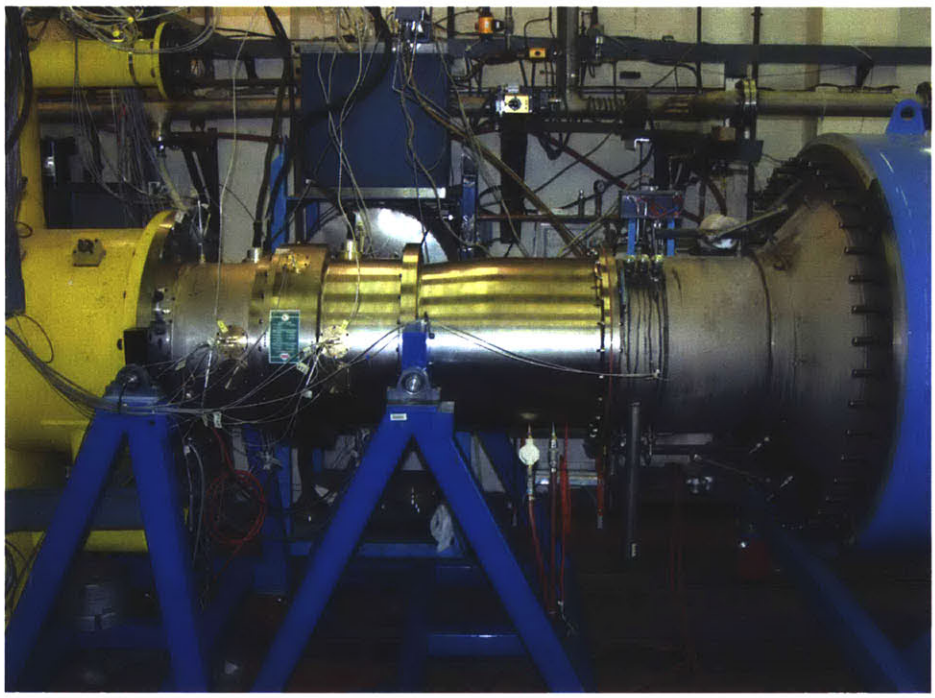

Figure 3.1: Blowdown Counter-Rotating Aspirated Compressor Facility, flow goes from right to left

3.1 Tanks and Accessory Systems

As discussed in Chapter 2 the volumes of the supply and dump tanks set the blowdown time constant and the time that the corrected flow through the compressor is constant, respectively. The dump tank is the same tank that was used for the Blowdown Turbine Facility. It has a volume of 570 ft^3 and can safely hold pressures up to 60 psia. The supply tank was specifically sized for this project. It has a volume of 157 ft^3 and can safely hold pressures up to 100 psia. The dump tank is bolted to the floor and serves as a datum for the assembly of the rest of the facility. The supply tank sits on wheels that mount to a 12 ft wide track and can travel up to 10 ft.

Vacuum is pulled through four inch pipes by an industrial pump that is capable of pumping 150 cubic feet per minute. Each tank was individually vacuum tested and were pulled down to about 60 millitorr.

The working gas in the facility is a 51.09%-48.91% mix (by mole) of Argon and Carbon Dioxide. There is a bottle farm for each gas. The piping system that connects the tanks, vacuum pump, and bottle farm is controlled by a series of solenoid actuated ball valves. The facility operator is capable pulling vacuum on one or both of the tanks, filling the supply tank to a specific pressure, and venting one or both of the tanks through two vents of different sizes. In the event of a power failure the valves are set in a manner so that both tanks and the bottle farm (if open) will vent to atmosphere, avoiding a dangerous over pressurization of the tanks.

3.2 Fast Acting Valve

The Fast Acting Valve was designed and built in 1981 by Guenette. The valve was designed to open in less than 50 ms, seal a pressure of 10 atm. in the tank against vacuum in the test section, provide a smooth expansion path for the gas exiting the tank, and operate in temperatures up to 530° F. The pressure and temperature requirements of the valve are less stringent for the CRAspC facility. The operating temperature is the ambient 70° F and the operating pressure is around 2 atm.

The valve consists of an outer annulus, a slider cone which seals against the outer annulus and a pilot cylinder which holds the actuators that move the slider. Figure 3.2 is a sketch of the valve. Inside the pilot cylinder is a pneumatic actuator that can hold the valve closed and initiates the acceleration of the slider. The slider is made of mild steel and weighs about 100 kg. In order to open the valve in 50 ms a force between 10,000 and 20,000 lb is required for accelerating the slider. A more detailed description of the valve can be found in "A Fully Scaled Short Duration Turbine Experiment" [9].

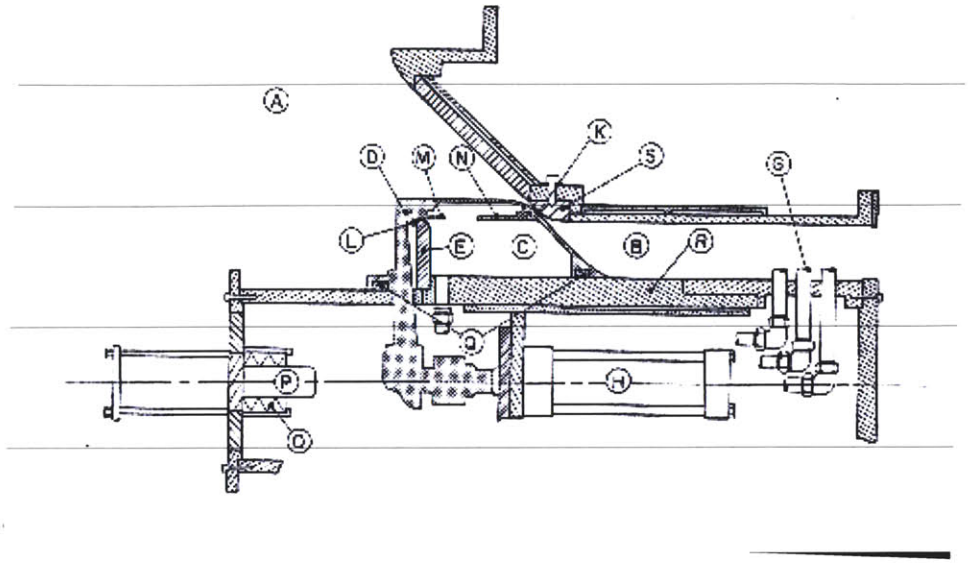

Figure 3.2: Schematic drawing of the Fast-Acting Valve [9]

There are three stages for the valve opening. These three stages are illustrated in Figure 3.3. The first stage is when the pneumatic actuator is fired, this opens the valve slightly. At this point the pressure in the chamber behind the slider is ~0 and the pressure on the dump tank side of the valve is the same as the pressure in the tank. This creates a large force that accelerates the slider. Next the chamber fills so that there is no pressure difference and the slider coasts. Finally the gap in the chamber closes so that as the slider moves backwards the gas in the chamber is compress and the slider decelerates. On the pilot cylinder there is a series of springs to absorb any energy still in the slider before it runs out of travel.

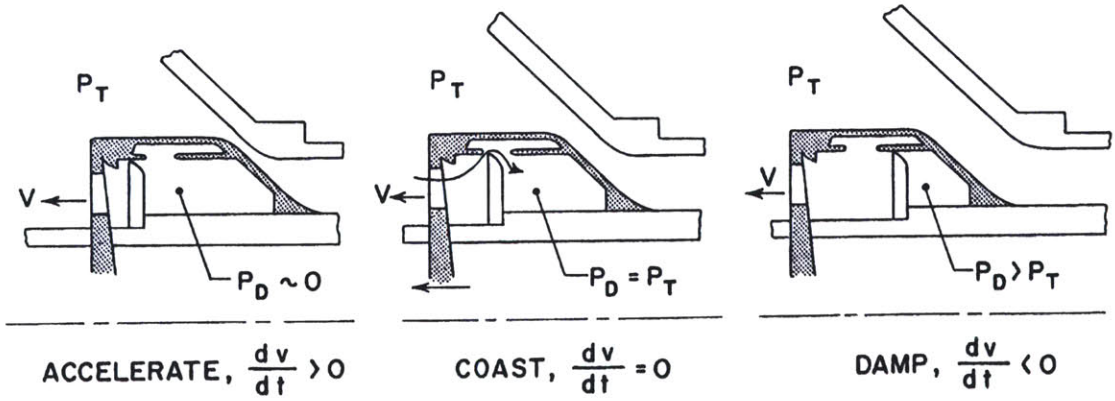

Figure 3.3: Sequence of events for the Fast-Acting Valve while opening [9]

Operating the fast acting valve with tank pressures of between 30 and 40 psi presented two challenges. The first was that there was less force available for use in creating a seal. To improve the seal two steps were taken. First, all elastomer o-rings in the valve were replaced and a seal plate that had been damaged was also replaced. Second, operational

procedures were modified and pressure inside the pilot cylinder was used to press the valve shut. Experiments showed that after the modifications, with 200 psi in the pilot cylinder and 1 atm in the supply tank, a vacuum of less than 100 millitorr could be maintained in the test section and dump tank.

The other challenge was that because of the lower pressure there was less force available for accelerating the slider and less gas in the chamber for damping. This problem was addressed by modifying the pressure in the pilot cylinder used to open the valve.

3.3 Test Sections

There is a separate assembly for housing each rotor and its flywheel and drive motor. Each section consists of flow paths, instrumentation ports, and the rotating assembly. Figure 3.4 shows details of both sections. Each assembly sits on a stand that moves along a track that is aligned with the track the supply tank runs on but is narrower in width. The tip casing is mounted into the aft section and acts as a guide when the forward section is bolted to the aft section. Elastomer o-rings are used at all interfaces to provide seals when pulling vacuum.

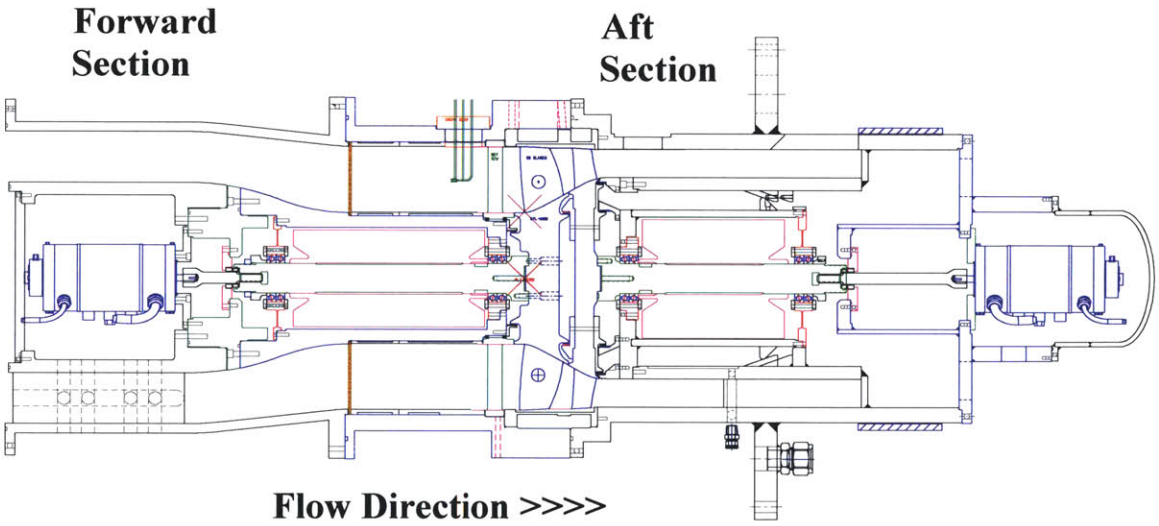

Figure 3.4: Sketch of Both Sections

3.3.1 The Forward Test Section

The forward section is shown in Figure 3.5. Important aspects of the design of the forward section are the pressure screen, the cantilevered nature of the housing for the

flywheel, and choosing tolerances of critical interfaces so that the appropriate parts were concentric about an axis.

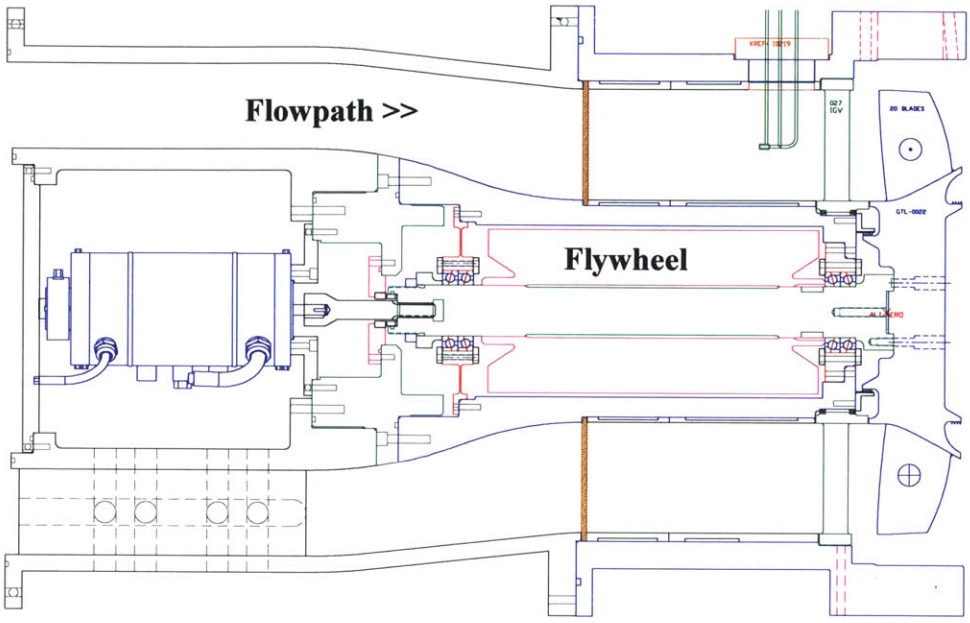

Figure 3.5: Forward Test Section

3.3.1.1 Vibration Analysis

The only connections between the inner and outer annuli of the forward test section are three thirteen inch long struts near the valve that are aligned with struts in the valve. Struts were not used at the rotor end of the test section because of a desire to keep the flow entering the compressor uniform. Early in the design process Dr. Michael Glynn, of the MIT Lincoln Laboratories, created a basic 3-D model of the test section and analyzed the vibration modes, natural frequencies, and static deflections of the test section. This analysis proved to be critical and lead to several design changes. Figure 3.6 shows the first vibration mode of the original forward test section design. This mode is one where the rotor bounces up and down. The frequency of this mode was 151 Hz (9060 rpm) which is lower than the 14,000 rpm design speed of the first rotor [10]. To solve this problem the struts were made longer and the slope where the inner diameter of the flow path is reduced from the valve ID to the first rotor ID was increased. Stiffness of a cantilevered beam decreases as length cubed. Changing the slope made the entire assembly shorter, therefore stiffer, increasing the frequency of the first mode so that it is greater than the design speed of the rotor.

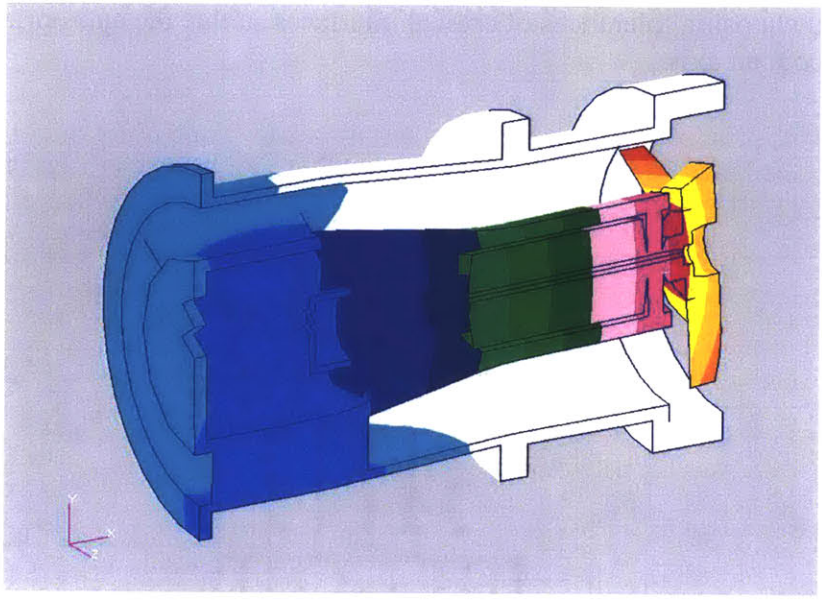

Figure 3.6: First Mode - 151 Hz (9060 RPM) [10]

3.3.1.2 Pressure Screen

The requirements of the pressure screen are that it must have the correct total pressure loss, pass the correct mass flow, and provide uniform flow to the compressor. Literature showed that sub-sonic jets exiting perforated plates required a length of about 40 hole diameters to mix out and that sonic jets exiting perforated plates required about 80 hole diameters to mix out [11]. The first attempts focused around using two subsonic screens with a combined pressure ratio between 2 and 3 (upstream total pressure to downstream total pressure). A handbook for pressure losses through various flow obstructions was consulted [12]. After investigation it was decided that the flow seen by the screen was not in the range of that described by the handbook, therefore a more reliable solution could be obtained with a choked screen. While the screen is choked the conditions entering the compressor are determined by the corrected speeds of the two rotors because they are supersonic and choked, not the supply tank pressure. The biggest challenge in designing the pressure screen was finding a commercially available stamped sheet of steel with small enough holes and but thick enough to withstand the pressure difference. The limiter on the thickness was the diameter of the holes. As the diameter of the holes decrease the thickness of the sheet that the dies can punch through decreases. It was found that for the same hole diameter the sheet thickness could be increased by using mild steel instead of hardened steel. The stress in the perforated plate goes as the inverse of the thickness cubed [13]. It was found that even though the mild steel has a yield stress that is almost half that of the hardened steel the stress in the plate decreased to a safe level because of the increased thickness.

Before the rotating assemblies were in the test sections the pressure screen was installed and run through several blowdowns with increasing dump tank pressures to verify the strength of the plate and determine the discharge coefficient. During these tests the only element controlling the flow was the choked screen. Stagnation pressures were measured

upstream and downstream. The thermocouples were too valuable to risk in these tests so it was assumed that the tank temperature and pressure were related isentropically. The mass flow through the tank was estimated from the pressure history in the tank. The discharge coefficient was calculated from the mass flow rate of the air exiting the tank. During preliminary calculations the discharge coefficient was assumed to be 0.62, from the tests it was calculated to be approximately 0.73.

3.3.2 The Aft Test Section

The aft test section is shown in Figure 3.7. Differences between the aft and forward sections include separate flow paths to the dump tank for the main flow and bleed flow and an absence of cantilevered structures. After the exit measurement plane flow disruptions like struts are acceptable, allowing for a much stiffer structure. The canister that holds the rotating assembly was designed so that it could fit in the assembly fixture used for the Blowdown Turbine Facility.

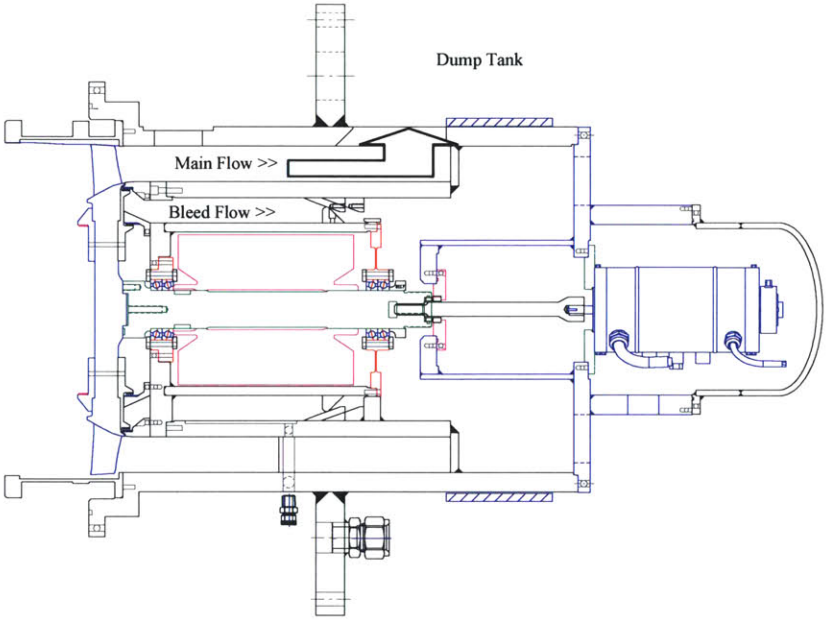

Figure 3.7: Aft Test Section

After exiting the root of the blades of the second rotor the aspiration bleed flow is kept separate from the main flow by two labyrinth seals. The bleed flow then passes between the main flow and the flywheel and passes through a variable area orifice that is used to meter the amount of aspirated flow. The bleed flow then passes by the motor housing into the dump tank without going through the main throttle.

The throttle that sets the corrected flow is an aluminum ring that rides on two hardened rods with linear bearings. A third rod is attached to the throttle and exits through the flange. This rod is used to open and close the throttle without disassembling the facility. Measuring the open area of the throttle comes from the displacement of this rod from a set point. A Cajon© fitting is used to seal the area around the rod and hold the throttle in place.

3.4 Rotating Assemblies

The rotating assemblies of the forward and aft test sections are very similar and will be discussed together. Important dimensions such as the bearings, tolerances, and drive motors are identical. Dimensions such as the rotational inertia and shaft lengths vary slightly between the two assemblies. Figure 3.8 is the forward rotating assembly and Figure 3.9 is the aft rotating assembly.

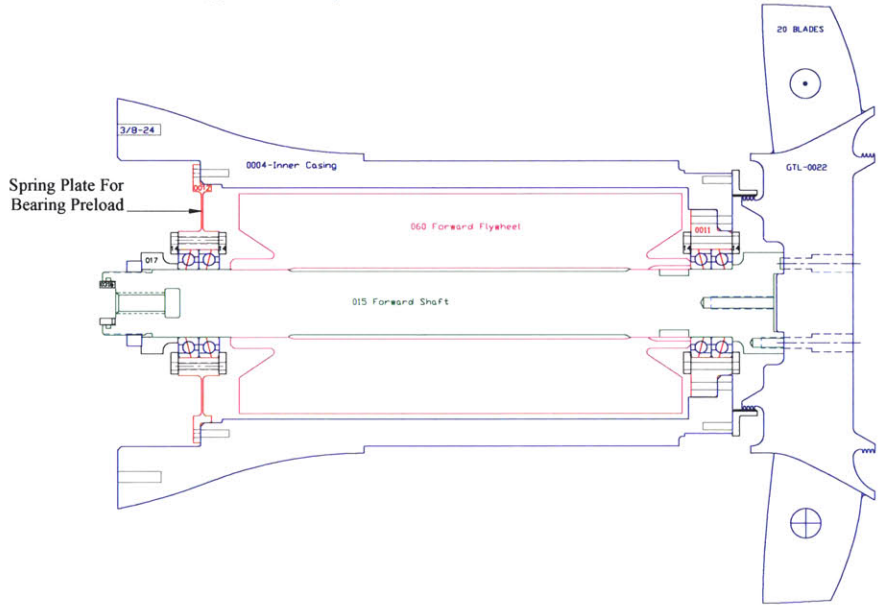

Figure 3.8: Forward Rotating Assembly

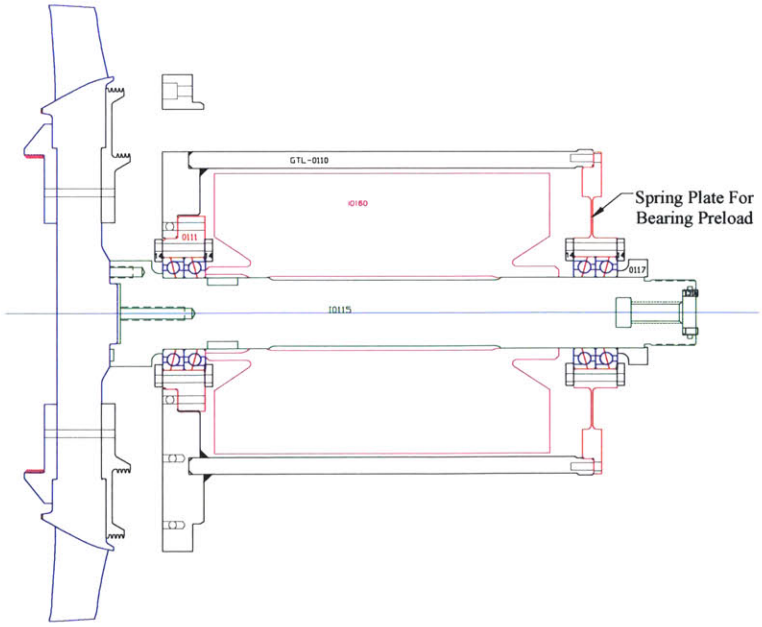

Figure 3.9: Aft Rotating Assembly

3.4.1 Bearings and Drive Shaft Assemblies

Choosing the proper bearings is critical to the operation of the test facility. The choice of what bearings to use was primarily based on experience from previous Blowdown Compressor Facilities. Fafnir super precision angular contact bearings were chosen. These bearings have angular contacts which makes them very stiff under axial loads. The rotors generate axial loads during operation so it is important that the bearings are stiff enough that the rotors do not move, possibly into each other, during the blowdown. The bearings are dual tandem mounted for maximum stiffness. Dual tandem mounting means that the thrust surfaces of both bearings in the pair face the same direction. This provides increased thrust loading capability in that direction. Two pairs of bearings are used for each shaft and the pairs are mounted in opposite directions.

The rated static radial loading of the bearings is 6,860 lbf. The rated permissible speed is 13,600 rpm. The design speed of the first rotor is 13,800 rpm; greater than the rated bearing speed. GTL experience had shown that during blowdown testing bearings can be operated beyond their rated range because of the low number of cycles they experience. A bearing with higher rated speed was available by decreasing the shaft diameter 5 mm. Vibration analysis showed that decreasing the shaft diameter reduced the frequency of the first shaft bending mode below the operating speed of the rotor. During shake-down testing the rotating assemblies were brought to their design speeds without incident. The expected life of the bearings was not calculated because the design speed was greater than the rated speed and expected number of cycles on the bearings was expected to be on the order of $8x10^5$, low compared to typical bearing applications. This corresponds to ~20 tests plus 30 minutes of facility shake-down tests.

One important aspect of the operation of the bearings is the amount of grease that is used. Minimizing heating in the bearings is important to prevent melting of the balls. Too much grease increases heat generation in the bearings. Not enough grease results in too much friction. GTL experience has shown that the proper amount of grease is about one dab (~0.1 g) of SKF LGLT 2/0.2 grease per ball.

At operating speed radial forces generated by the balls in the bearings, combined with the angular contact surface, generate an axial force that tends to separate the inner and outer races resulting in bearing failure. The bearings need to be preloaded to prevent this separation. The bearing manufacture recommends different levels of force for preload. The lightest was selected to limit friction and heating. The axial preload force is created by a spring that doubles as a bearing mount (labeled in Figures 3.8 and 3.9). Sixteen 0.75 inch holes were drilled in the 0.062 inch thick membrane to tailor the axial spring constant. Finite element analysis predicted, and tests confirmed, that the springs have a stiffness of 50 lbf per 0.001 inch. During assembly measurements were made of the spring-bearing assembly and of the distances to each mating surface. A spacer ring was then made to create the correct displacement of the spring when the shaft nut is tightened.

When everything is touching there is approximately 100 lbf of pre-load on the bearings. The aft spring is shown in Figure 3.10 with the bearings.

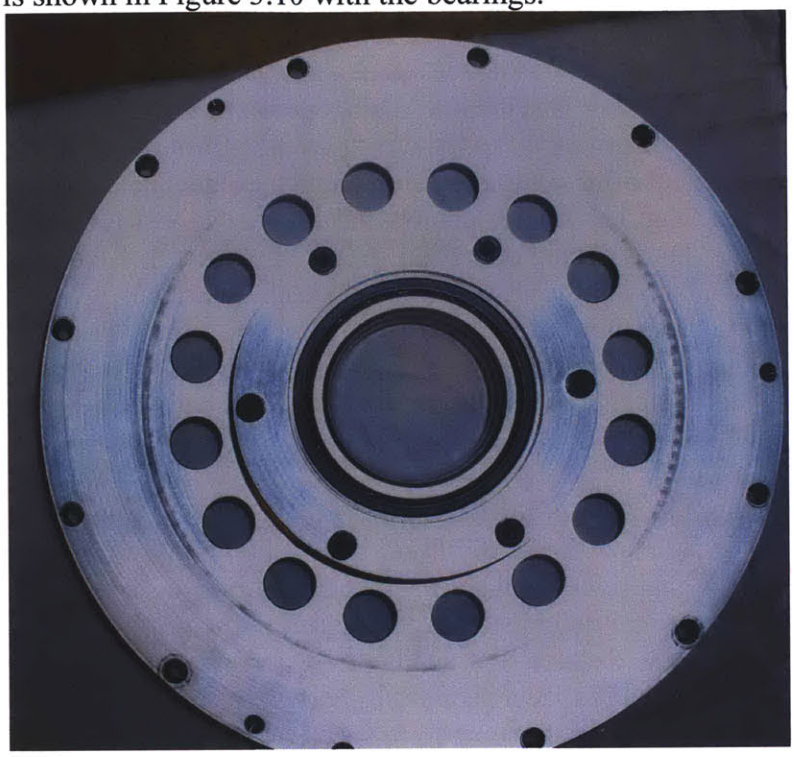

Figure 3.10: Aft bearing and spring-plate assembly

3.4.2 Flywheel Design

Designing the flywheels to maximize the inertia within the size constraints, and minimizing forces due to imbalance, required a considerable amount of effort. Various high density materials were investigated including tungsten alloys and depleted uranium. Flywheels made of tungsten-nickel alloy, which would have operated super-critically on springs, were designed and manufactured. The strength of the alloy billets was less than reported by the alloy manufacturer and they burst near design speeds during over-speed tests. The flywheels were then redesigned and made with 17-4 PH stainless steel. The steel flywheels have a lower inertia and were designed in such a manner that springs were not required.

3.4.2.1 The Tungsten Solution

3.4.2.1.1 Material Challenges

As mentioned above multiple high-density materials were investigated for maximizing the flywheels inertia. An alloy of 97% tungsten and 2% nickel was selected. The tungsten had a high density (~2.5 times more than stainless steel), a high advertised yield strength (85,000 psi), and the nickel made it machinable. Both flywheels burst at a stress condition of approximately 35,000 psi, approximately one third the predicted yield stress. The author believes that the lower stress at which it burst is due to two factors. The first

factor is that tungsten is a brittle material, therefore the statistics of the stress for failure have a larger variation than a ductile material. These statistics for the specific alloy were unavailable to the author. Second, the billets were relatively large. This could have led to problems in adequately controlling the sintering process. The billets were ultrasonically inspected. In the forward flywheel no voids were found and in the aft flywheel 8 voids ranging from 0.020 in. to 0.032 in. were indicated. The manufacturer of the billet indicated that voids this small should not deteriorate the strength of the billets [15]. Figure 3.11 is a piece of one of the flywheels after bursting.

Figure 3.11: One piece of a tungsten flywheel after bursting.

3.4.2.1.2 Design Challenges

Another challenge in designing the flywheels was establishing a way to maintain centrality during operation. At design speed the bore of the flywheels grew nearly 0.0005 inches more than the shaft. Without something to keep the flywheel centered a clearance that large would lead to an imbalance force of ~1,500 lbf. A cyclic force this large is unacceptable, especially considering that the bearings operate at their limit. Many options for centering the flywheel were investigated. Most involved trying to clamp onto the flywheel at a larger diameter, none of these were satisfactory. The chosen solution was to operate the flywheels 'super-critically'. The flywheels were to be attached to the shaft by plates, given the name Inertia Centering Plates (ICP), with spiral arms cut out of them that made the plates radial springs. Figure 3.12 shows one of the ICPs.

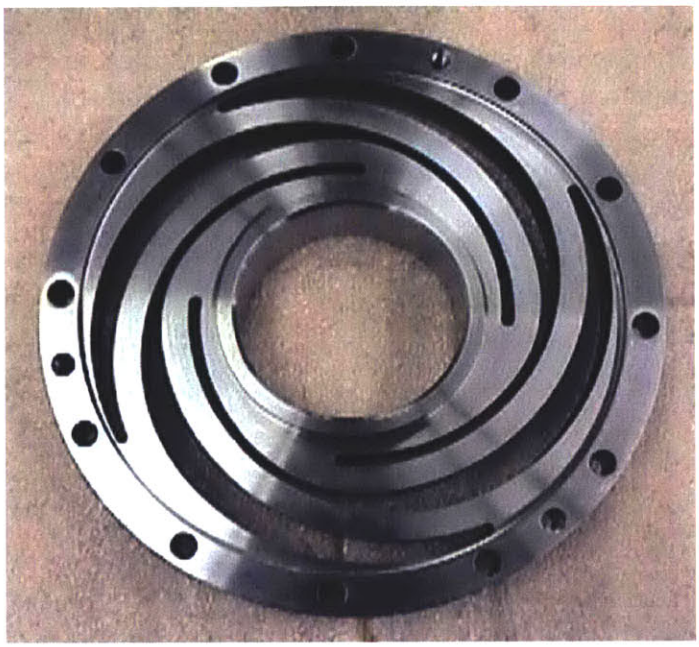

Figure 3.12: One of the Inertia Centering Plates

The goal was to operate the flywheels between the first and second vibration modes of the spring and flywheel system. Vibration theory shows that after going through the critical frequency the response of the system to a cyclic input decreases as the frequency of the forcing increases [14]. In this system the cyclic force is a result of an un-avoidable imbalance in the flywheel. The radius of the bore of the flywheel was designed to be 0.003 inches larger than the radius of the shaft. A gap is necessary to allow the flywheel to move and settle to a steady operating condition during the acceleration. The gap size was selected with the constraints that it be small to minimize the force on the bearings while passing through the critical frequency and larger than the static deflection of the flywheel on the springs. The mass of the flywheel, combined with the desire that the critical frequency be ~1/4 the design speed, set the necessary stiffness of the flywheel.

Dr. Michael Glynn was asked to perform the Finite Element Analysis of the ICPs. Figure 3.13 shows the estimated stress in the final design of the springs. After three design iterations it was found that the radial stiffness of the springs of the springs was approximately linear with the following dimensional grouping of design variables, referred to as the 'geometric constant': $K \propto \frac{E \cdot I}{\alpha \cdot R^3}$ Where E is the elastic modulus of the material, I is the bending moment of a cross section of the arms, R is the radius of the arms, and α is the angle that the arm extends across. After this relationship was established the next design met the requirements for radial stiffness. Figure 3.14 is a plot of predicted stiffness from FEA vs. the value of the geometric constant.

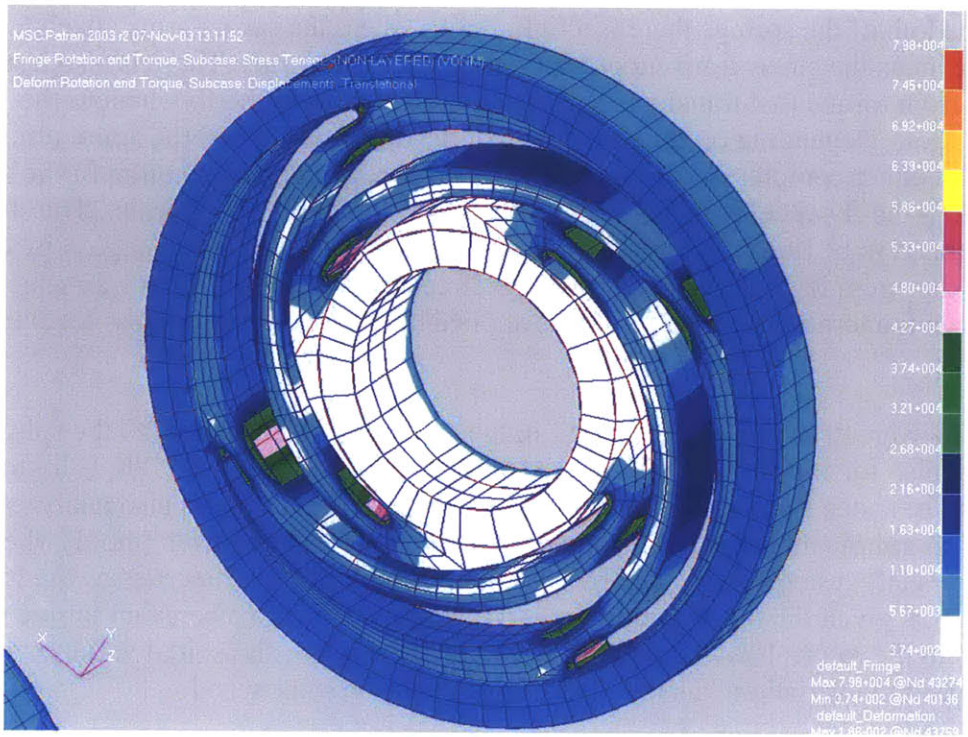

Figure 3.13: Von-Mises Equivalent Stress (psi) in the ICPs [10]

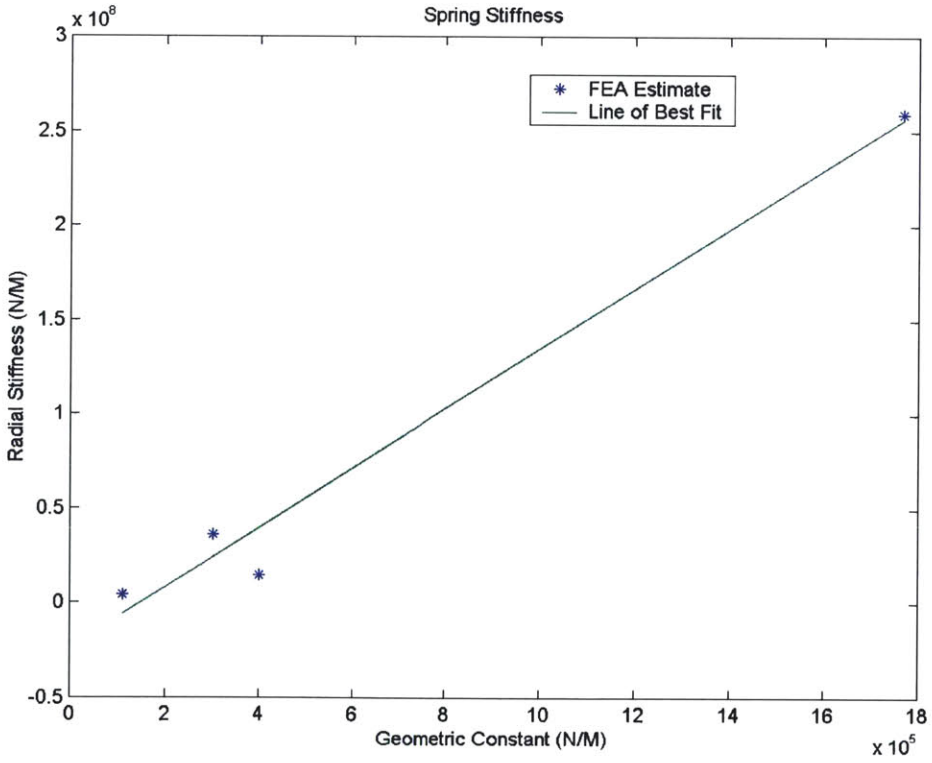

Figure 3.14: FEA Estimate of Spring Stiffness for Different Geometries

Near the hub of the springs there is a tight radius where the spring arms attach to the hub. In these areas the stress from supporting the flywheels is large. There is also a stress that results from torque that transfers rotational momentum from the flywheel to the compressor. Depending on the direction that the torque is applied the spiral arms are placed in either compression or tension. The compression/tension nature of the stress due to holding the flywheel is independent of the direction of the spiral arms. The stresses are assumed to be linear in nature so adding a compression stress to a region in tension lowers the stress level in the material. The direction of the spiral arms was selected so that when the torque from the rotor was applied it lowered the total stress level in the ICP.

The ICPs were designed to be a spring in the radial direction but, due to the spiral design, they are also torsion springs. During the test they essentially see a 1,000 ft-lbf torque in the form of a step function. The rotational stiffness of the ICPs was also analyzed by Dr Glynn. A simple model was developed with two rotational elements (the flywheel and the rotor/shaft system) connected by a torsion spring with the properties of the ICPs. The system was given the initial condition of the design speed and a constant torque was applied to the rotor. It was found that although there was a sinusoidal variation of the rotor speed the variation was less than 1% of the mean rotor speed.

Analysis predicted that as the flywheels passed through the critical speed approximately 850 lbf and 630 lbf would be imparted to the shaft and bearings by the forward and aft flywheels respectively. Balancing the flywheels to better than 1 oz-in would limit the imbalance forces at full speed to 315 lbf and 220 lbf (Forward, Aft). Unfortunately, the material failed during over-speed tests, and the operation of the system in the blowdown rig was never observed.

3.4.2.2 The Steel Solution

After the tungsten flywheels burst using tungsten was abandoned because of time and economic constraints. 17-4 PH stainless steel, heat treated to an H1150 condition, was chosen as a substitute material because of its well known properties and high strength. The lower density of 17-4 decreased the inertia and required that the facility be run with a lower initial pressure in the supply tank, reducing the expected Reynolds' number. Also the method of running the flywheels super-critically was not an option with the steel flywheels because the lower mass increased the critical frequencies to an unacceptable speed.

The bore of a steel cylinder with the dimensions of the flywheels, rotating at the design speeds, grows ~7×10^{-4} and 5×10^{-4} inches (Forward, Aft). While less than the growth of the tungsten flywheel this is still too much. During the re-design process it was noted that the growth of the bore goes as the outer radius squared. By having a section at each end that is only ~ 3/8 in. thick the growth of these lands is almost negligible. Furthermore, not all the material above these lands had to be removed, just enough to separate the lands from the material at the higher radii. This meant that the removed material, at the lower radii, has a small impact on the inertia. Without the ICPs the

flywheels can be made slightly longer further increasing the available inertia. Figure 3.15 is an outline of the forward flywheel.

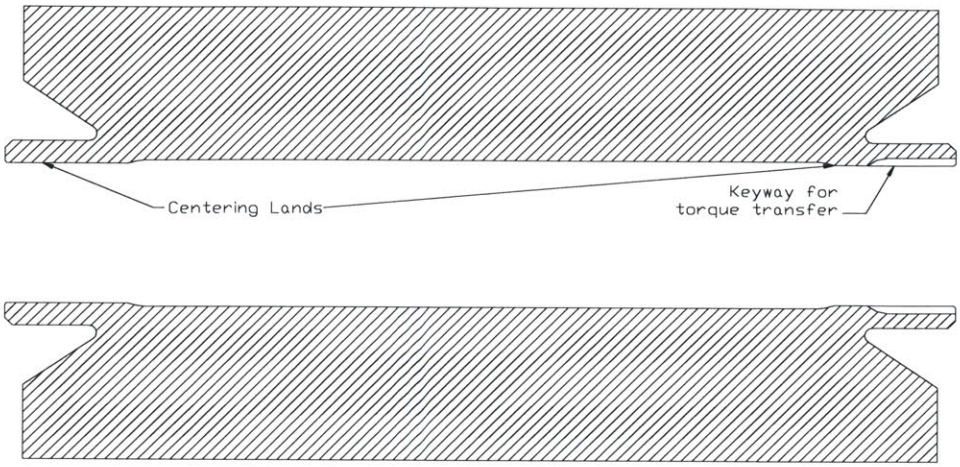

Figure 3.15: Forward Flywheel

Finite element analysis showed that the radial growth of the lands is in fact slightly negative. This is shown in Figure 3.16, the FEA of the forward flywheel. The pinching in of the centering lands is a result of material above them pulling upwards. During the initial shake down tests of the rotating systems no imbalance problems were experienced.

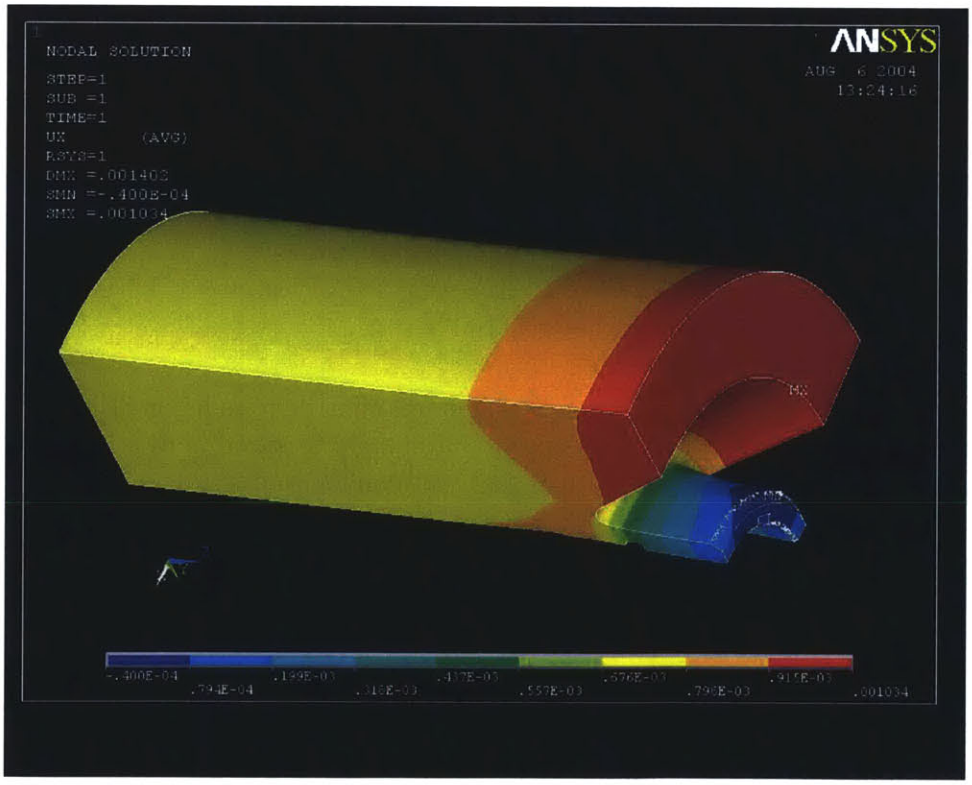

Figure 3.16: Radial Deflections of the Forward Flywheel (m)

The most significant challenge involving the stainless steel flywheels was encountered during assembly. The flywheel and shaft were designed so that the radial gap between them would be 0.0000 to 0.0003 inches. When manufactured there was a slight gap (within tolerance) but they would not go together, partly because they were made of the same material. Because both pieces have the same hardness trying to force the shaft into the flywheel would have resulted in galling. The first step to solving this problem was turning down the shaft, coating it with chrome (a harder material), then re-grinding it to the specified diameter. Then the bores were given another honing pass to increase the diameters by 0.0001 in. Finally the shafts were cooled before being inserted into the flywheels. The shafts can be removed from the flywheels without tooling.

3.4.3 Motors and Motor Control Architecture

The motors used in the Blowdown Compressor Facility are 15 hp motors made by Reuland Electric. These motors use 440 volt AC power. They are rated for 16 amps and 16,000 rpm. Power is supplied to the motors by a Yaskawa GPD-515 motor drive. A LabView© program was written to send commands from a computer to the GPD-515 such as set speed, acceleration rates, 'coast', and 'stop'. The computer that runs this LabView© program is physically located next to the computer that operates the Data Acquisition System (DAQ) so that the motors and DAQ can be run by the same person.

Temperatures in the motors are monitored manually, although the drives have the capability to accept input commands related to overheating this functionality was not used. The motors have six thermocouple outputs. They are located on the motor bearings at multiple locations on the windings. Temperatures in the motors were not allowed to exceed 250 F.

The encoders on the motors were designed for this facility. Each encoder has two outputs; a once per revolution signal and another where the number of pulses is equal to 16 times the number of blades. The number of pulses was chosen so that future high speed measurements could be correlated to blade passages.

3.4.3.1 Requirements for Motor Operation

The motors are cooled with cold process water and must operate in air because of internal lubricants. The rotors must be in vacuum to bring them to speed with a 15 hp motor therefore there needs to be a mechanical seal between the motor housing and the rest of the test section. This seal is created with a carbon face ring where the main shaft mates with the quill shaft. The carbon face seal can be run dry but a thin layer of Shell Turbo T68 oil was placed on the face during assembly. Water lines, power cables, encoder signals, and thermocouples are fed into the motor housing through four ¾ inch holes in one of the struts of the forward section. This meant the welds for these struts had to be vacuum tight. Figure 3.17 shows the forward motor housing with support hoses coming through the strut. These lines for the aft motor are brought in through 1 inch flex tubes connected with Swagelock© fittings.

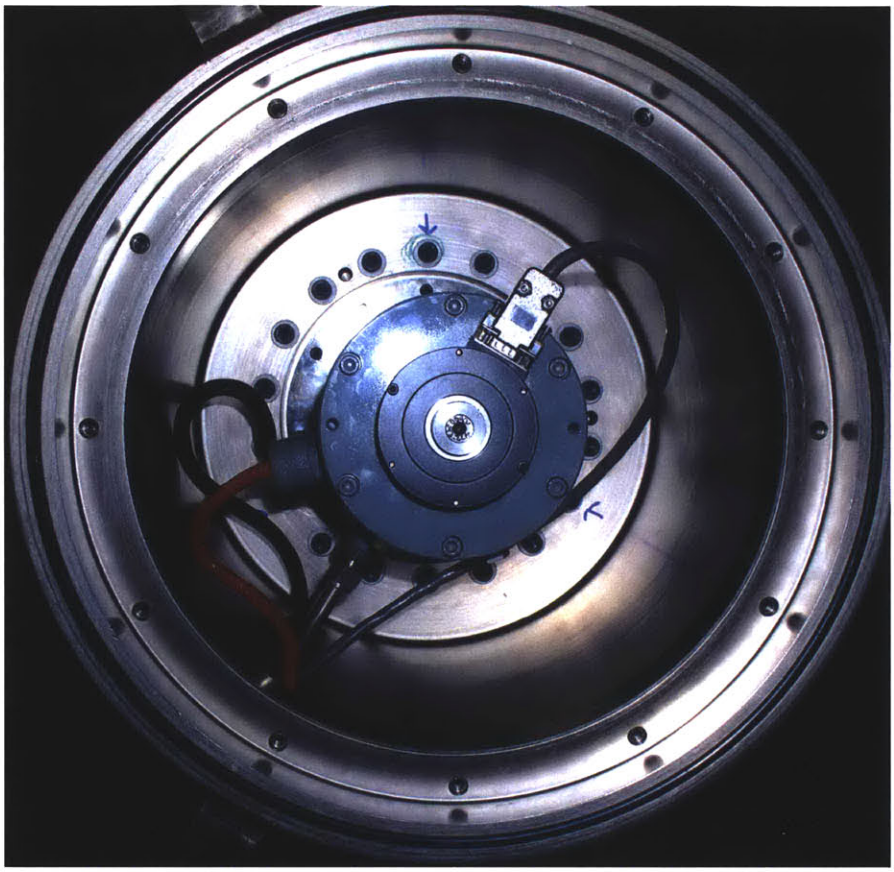

Figure 3.17: Forward motor housing, showing water and electrical lines through the struts.

3.4.3.2 Motor Control

There were two requirements for motor control in the Blowdown Compressor Facility. First, the motors needed to hold the design speed within 1%. Second, the motors had to be brought to speed and slowed down as quickly as possible to limit the amount of wear on the bearings. Also, the system cannot be allowed to slow down through bearing friction, this would take too long and the heat generated in the bearings could cause them to melt. The drives are able to decelerate the motors. 5,000 Ω resistors are utilized during deceleration to dissipate some of the power.

The motors are controlled by setting a set speed and acceleration schedules. Operators can choose a set speed, high and low speed acceleration rates, high and low speed deceleration rates, and a switching speed. Typically the two deceleration rates are set to the same value. The low speed acceleration is set to the calculated maximum acceleration (based on the available motor power and the inertia of the system), the high speed acceleration is set to a very low value (typically 0.3 Hz/sec), and the switching speed is set to approximately 5 Hz less than the set speed. Switching to a low acceleration rate before the set speed prevents the motor from over-shooting the set speed. At any point while the motor is running the operator can select 'coast' or 'stop'. If 'stop' is selected then the motor is decelerated at a rate that is dependant on the speed

and the set deceleration rate. When 'coast' is selected power to the motor is removed and it is allowed to slowly decelerate due to bearing friction. Typical operation sequence for a test is that the rotors are brought and held at the design speed, the DAQ is then armed, the motors set to coast, and the valve fired. The motors are then used to stop the rotors. Typically it takes about five minutes to bring the rotors up to the set speed.

4 Design and Manufacture of Bladed Components

The primary focus of this chapter is the manufacturing of the bladed components of the Counter-Rotating Aspirated Compressor (CRAspC). The author was involved with the mechanical designs of the blade and managing the production process. The aero-dynamic design is discussed in Section 4.1 because mechanical design and manufacturing decisions must be influenced by the aerodynamic design. The bladed components of the test facility are the Inlet Guide Vanes (IGV), first stage rotor (non-aspirated), and second stage rotor (aspirated). Producing these components required a synthesis of aerodynamic design, structural analysis, and advanced manufacturing processes.

4.1 Blade Design

Aerodynamic design of the blades in the CRAspC is the work of Dr. Ali Merchant. The methodology and code used to design and predict the performance of aspirated blades was developed by Dr. Drela and Dr. Merchant from first principles. Unlike most industry designs there was no database of previous design knowledge to use in designing these stages. The designs were also analyzed by Dr. John Adamczyk of NASA Glenn using APNASA, a 3-D viscous code.

4.1.1 Counter-Rotation Benefits and Challenges

The pressure rise across an axial compressor is a result of the change in angular momentum of the fluid. Typically between stages the swirl is removed from the flow by stators. By not removing the swirl and counter-rotating the next stage a much larger change in angular momentum can be achieved with lower physical speeds. A common method for conceptualizing the change in angular momentum for a stage is velocity triangles. The velocity triangles for the counter-rotating compressor are shown in Figure 4.1 [16].

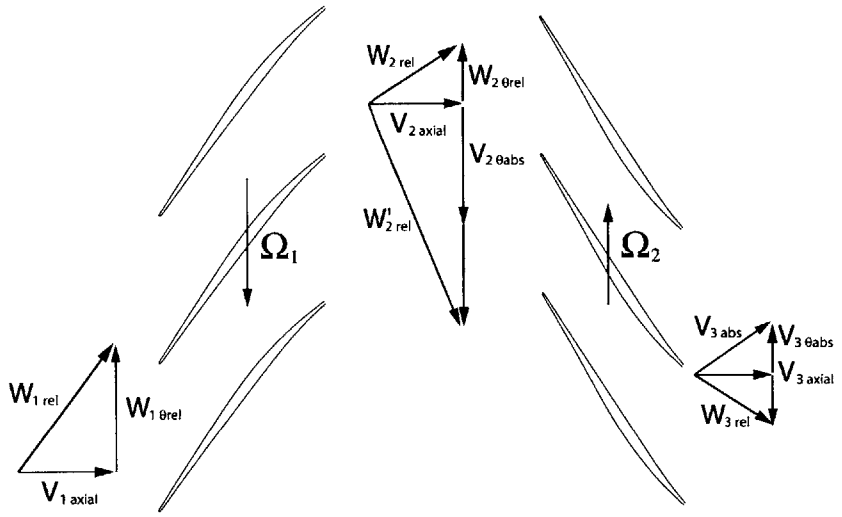

Figure 4.1: Velocity Triangles for a counter-rotating compressor [16]

The benefits of counter-rotation have been known since at least the 1950's with the Curtiss-Wright Counter-Rotating Compressor [1]. To date attempts at counter-rotation have been unsuccessful. The characteristics of the flow that have prevented success are high relative Mach numbers in the second rotor, separation (typically indicated by high diffusion factors), sensitivity to shock un-start, and finally matching the two rotors is more difficult when the stator between them is removed. Section 4.1.4 discusses how predictions show that aspiration might be a solution to these difficulties.

4.1.2 Inlet Guide Vanes

The Inlet Guide Vanes were employed to introduce a slight counter swirl into the hub of Rotor One. This increased the loading at the hub of Rotor One and decreased the loading of the hub of Rotor Two; increasing the overall performance of the machine. Above the hub the IGV does nothing to modify the flow. Figure 4.2 shows the hub, mid-span, and tip streamlines of the IGV.

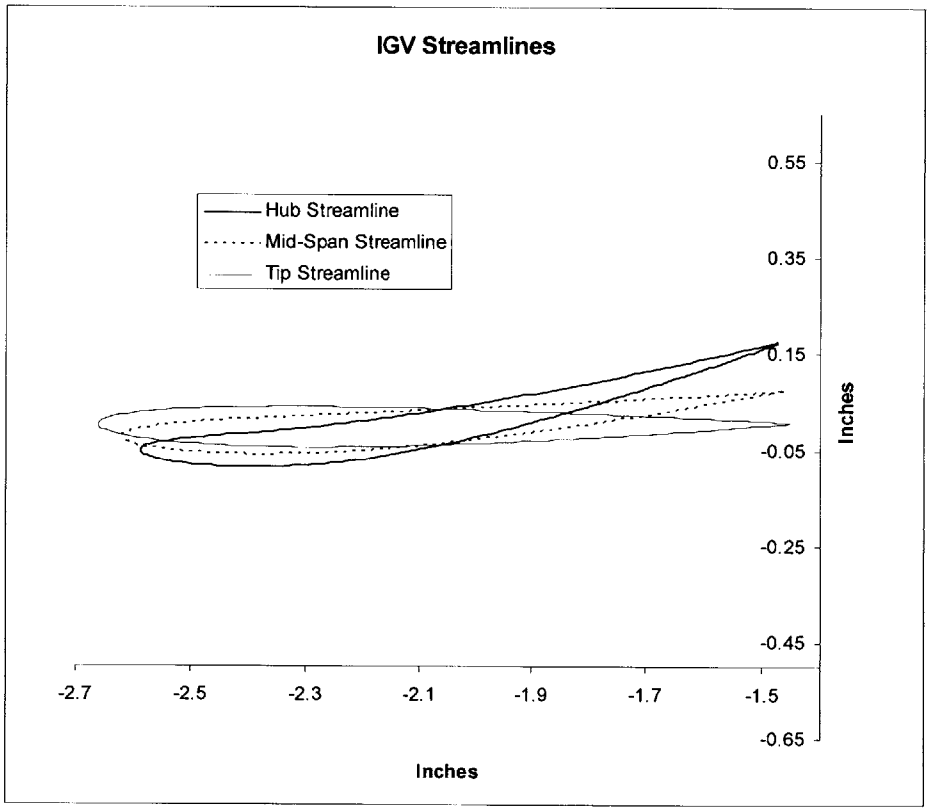

Figure 4.2: Streamlines that define the Inlet Guide Vanes

After it was decided to use an IGV there was a need to be able to measurements across an entire IGV pitch in the downstream measurement plane. This is due to IGV wakes passing through both rotors. In previous Blowdown Turbine experiments a translator was built that moved the downstream instruments circumferentially so that the circumferential variation due to the nozzle guide vane wakes could be measured. Designing and building

the translator requires a large amount of time and resources that were unavailable. It was believed that by placing the IGV on bearings, and tailoring its inertia for a certain acceleration rate, that the translator could be replaced. Fundamentally there is no difference between a rotating IGV with stationary probes and a stationary IGV and rotating probes. During early shake-down tests it was noticed that while the IGV did accelerate as predicted due to the incoming flow there were interactions with the first rotor that were not modeled that resulted in the speed of the IGV exceeding the rated speed of it's bearings after the test time. In order to maintain a safe operating situation and protect the rotors the capacitance probe that had been used to measure the IGV speed was replaced with an aluminum rod that fixed the IGV in place.

4.1.3 Rotor One

The first rotor is an un-aspirated fan that has supersonic tip relative Mach numbers. Rotor One has 20 blades, a hub to tip ratio of 0.5 and an average aspect ratio of about 1.6. The design tip speed (in air) is 1450 feet per second. The design pressure ratio is 1.92 with a polytropic efficiency of 0.923. Table 4.1 summarizes the aero-design parameters of Rotor One. An important measure of compressors is their diffusion factor (recall Eqn. 1.1). The diffusion factor is a zero-th order indicator of how efficient the compressor will be. Typically, compressors with diffusion factors greater than 0.6 experience separation and unacceptably low efficiencies [2]. The diffusion factor for the first rotor is .48 and the average relative Mach number across the span of the first rotor is 1.26 [16]. Figure 4.3 is the hub, mid-span, and tip streamlines of the first rotor. Figures 4.4 – 4.6 show lines of constant Mach number within the rotor passage for three different streamlines.

Table 4.1: Rotor One Aero-Design Summary [16]

Rotor One Stage Aero-Design	
N Blades	20
Hub to Tip Ratio	0.5
Tip Speed	1450 fps
Polytropic Eff.	0.923
Aspect Ratio	~1.6
D Factor	0.48
Pressure Ratio	1.92
$\Delta H/U^2$	0.34

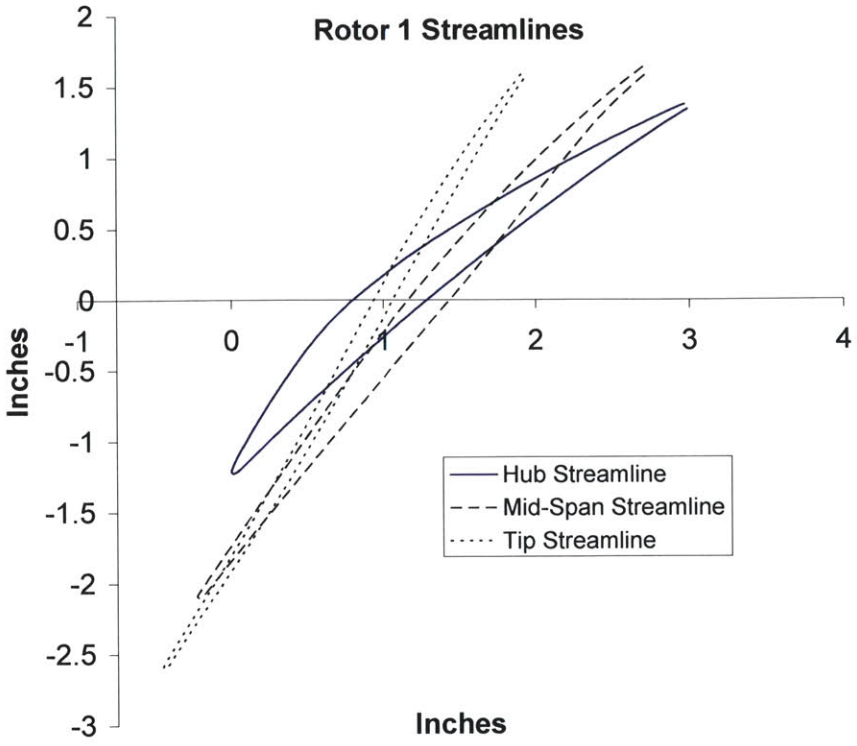

Figure 4.3: Rotor One Streamlines

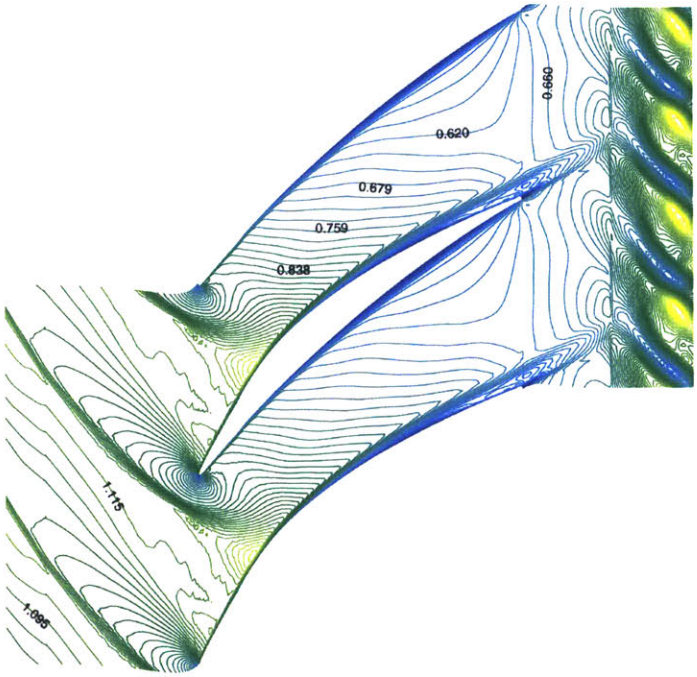

Figure 4.4: Relative Mach Number Contours of Rotor One at Hub, D=0.53 [17]

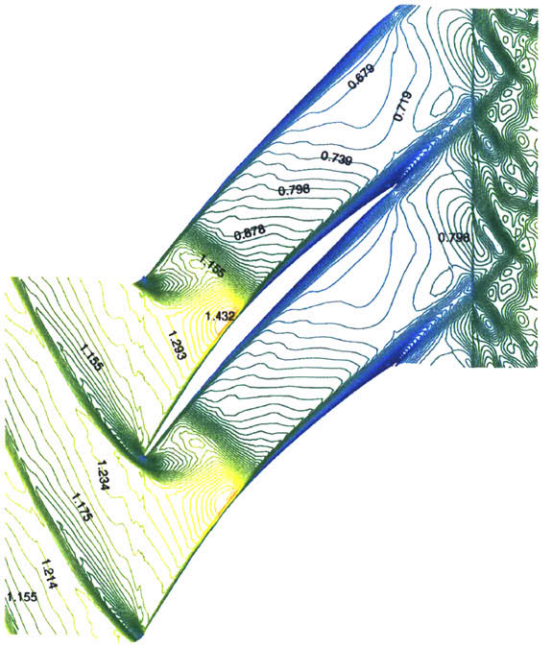

Figure 4.5: Rotor One Relative Mach Number contours, Mid-Span [17]

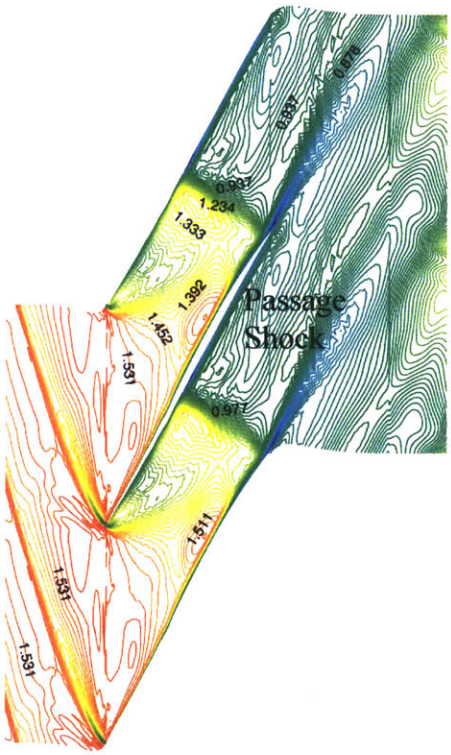

Figure 4.6: Rotor One Relative Mach Number Contours, Tip [17]

4.1.4 Rotor Two

The second rotor is aspirated and the flow is supersonic relative to the blade across its entire span. Rotor Two has 29 blades with an aspect ratio of 1.75 and operates at a tip speed of 1150 fps. The pressure ratio is 1.6 with a polytropic efficiency of 0.902. The diffusion factor for this stage is 0.52, higher than rotor one and typical compressors [16]. Approximately 1% of the stage inlet mass flow is used in aspiration. CFD results indicate that aspiration technology is a solution to many of the hurdles in counter-rotation. First, aspiration removes low-momentum boundary layer fluid which delays or even prevents separation effectively increasing the range of diffusion factor available to a designer. This concept is illustrated in Figure 4.7. Second, as with supersonic inlets, the aspiration slot sets the shock position within the rotor passage. This is illustrated in Figures 4.9 – 4.11. Figure 4.8 shows three streamlines for the second rotor.

Table 4.2: Rotor Two Aero-Design Summary [16]

Rotor Two Stage Aero-Design	
N Blades	29
Hub to Tip Ratio	0.7
Tip Speed	1150 fps
Polytropic Eff.	0.902
Aspect Ratio	~1.75
D Factor	0.52
Pressure Ratio	1.6
$\Delta H/U^2$	.50

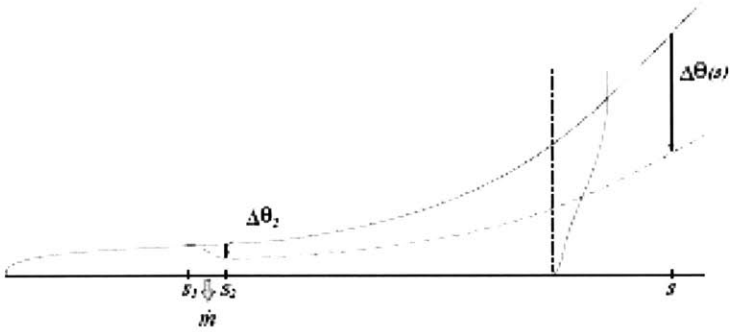

Figure 4.7: Effect of Aspiration on boundary layer growth

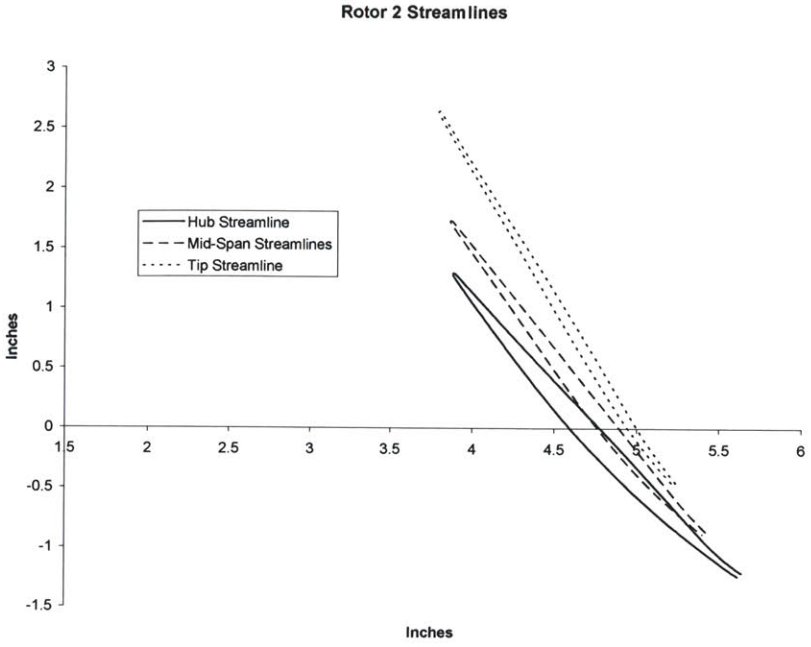

Figure 4.8: Streamlines for Rotor Two

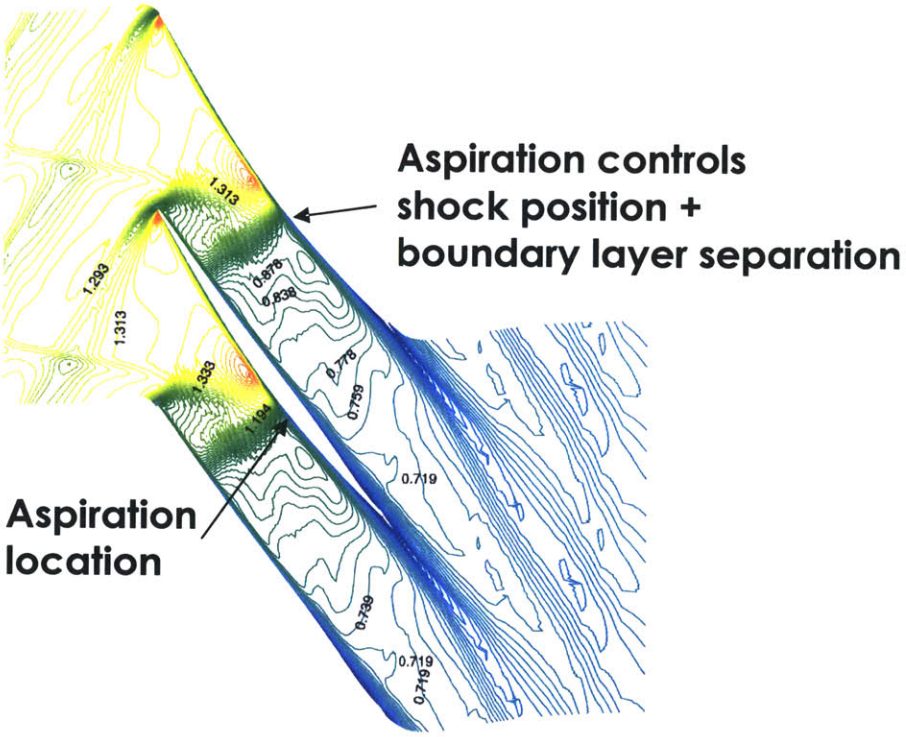

Figure 4.9: Relative Mach Number contours for Rotor Two at hub [17]

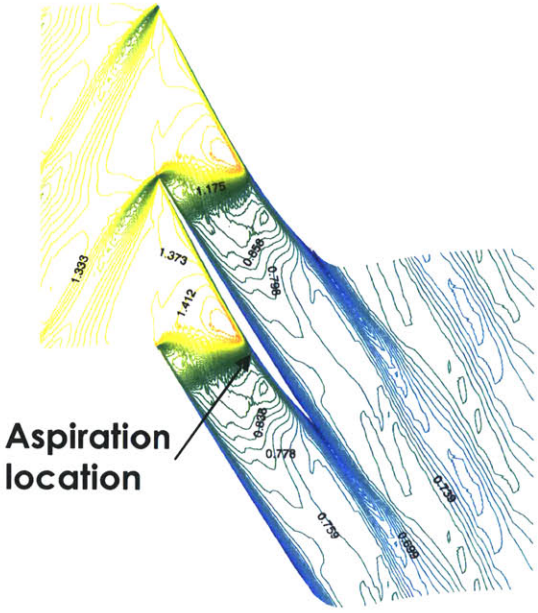

Figure 4.10: Mid-Span Relative Mach number contours, Rotor Two [17]

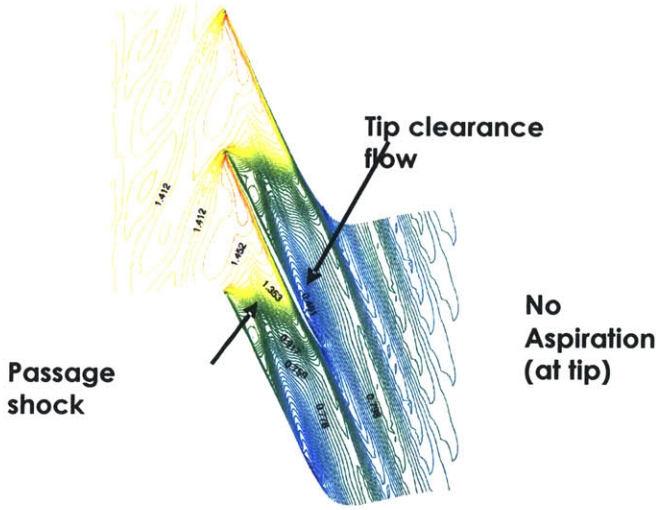

Figure 4.11: Rotor Two Relative Mach number contours at tip [17]

4.1.5 "Hot-to-Cold" Geometry Transformations

It is important to note that the aerodynamic geometry generated by the aero-design codes is not the final data that is used for manufacturing the compressors. When placed under centrifugal and aerodynamic loads the blade geometry changes. The geometry used for manufacture was generated by putting the aero geometry into a finite element code and applying centrifugal and aerodynamic loads in a direction opposite of what the blades experience. Care had to be taken to apply these loads in a non-linear manner because the

as the blade deforms the center of mass changes, changing the effect of the centrifugal loads. In these two rotors the tips grow nearly 0.015 inches and un-twist.

4.2 Five-Axis Machining of Blisks

The IGV and first rotor are both blisks. Blisks, also known as integrally bladed rotors (IBRs), are components where the blades and disk are one piece, typically machined from a forging. Blisks are gaining popularity in use in axial compressors. Blisks reduce part counts, complexity, and eliminate problems of wear at the blade-disk interfaces. For this project using blisks where possible was attractive because it reduced manufacturing cost per rotor by reducing the number of machine set-ups. There are a few variables that determine the cost of the blisk. These are the fillet radius, surface finish, and profile tolerance. Ultimately all of these variables influence machine time.

Figure 4.12 shows the IGV while still on the machine. Normally integrally machining the shroud and blades together makes the process more difficult. This is due to the fact that the part must be flipped at least once (increasing setups), that when roughing material a tool that is not designed for plunging will be expected to plunge, and typically non-optimized roughing patterns are used. However, in this specific case adding the integral shroud for inertia simplified the machining process. The blades have a very high aspect ratio. These long short blades would not provide enough resistance to the cutting forces. The shroud provides another clamped boundary condition and makes the blades much stiffer. Without this holding tolerances on these blades would have been difficult due deflections. Section (4.2.1) gives a more detailed description of how blade mechanics affect the machining process.

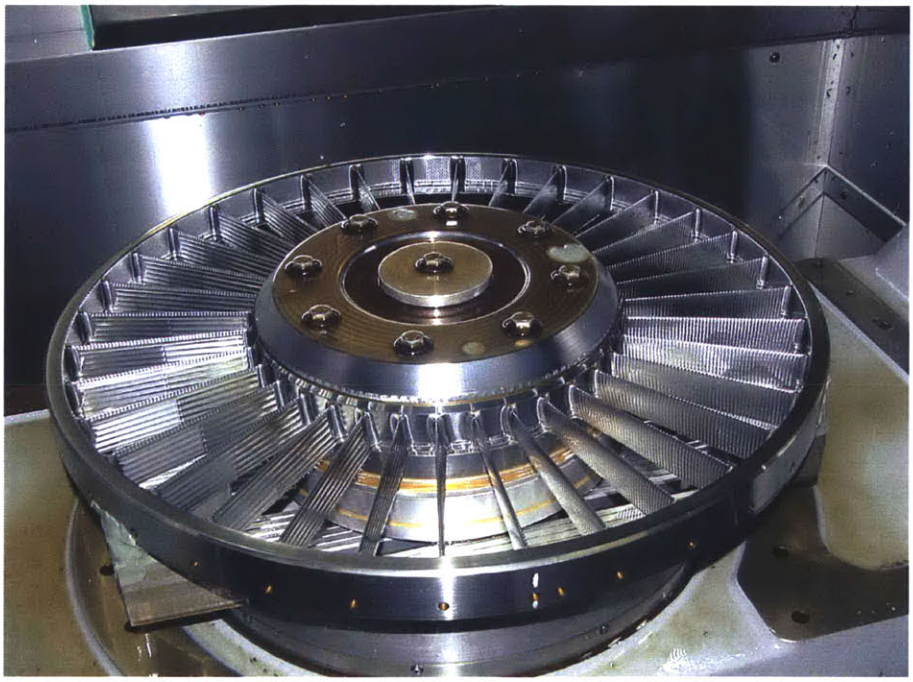

Figure 4.12: IGV while still on the machine

4.2.1 Selection of Profile Tolerance

Profile tolerances are a method of controlling deviations of a three dimensional surface. The best way to think about profile tolerancing is to imagine offsetting the design surface on both sides by the amount of the tolerance. A surface that fits within this envelope meets the tolerance. Figure 4.13 is a two-dimensional sketch of this concept. The profile tolerance for the blades was selected based on the length scale that could be resolved by the CFD design codes and what could reasonably be maintained by the machines that would be used. Table 4.3 lists the length scales of each blade section and the profile tolerance.

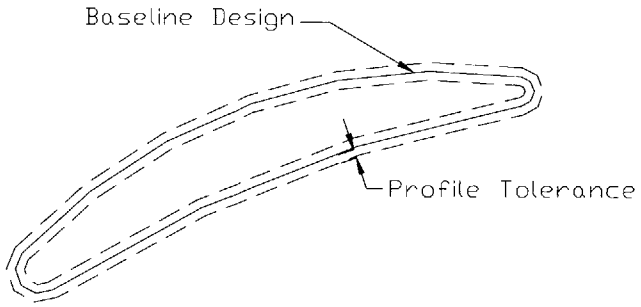

Figure 4.13: Sketch that illustrates the concept of a profile tolerance

Table 4.3 Blade Row Length Scales

Blade Row	Diameter	Chord	Span	Profile Tolerance
IGV	21"	1.14"	5.18"	0.010 in.
Rotor One	21"	4.5"	4.62"	0.006 in.
Rotor Two	21"	3.0"	2.72"	0.004 in.

For the manufacturer holding the blade tolerance is a matter of balancing multiple deflections. First the tool is essentially a beam, when cutting forces are applied to the tip of the tool it bends. The longer the tool is, and normally tool length is a function of blade height, the greater the deflection is. Second, the blade also acts as a beam and bends under the cutting forces. Generally the machine tool path is created so that if everything in the system was perfectly rigid a blade thinner than the design would be produced. The decision for the magnitude of this undercut is based on the blade material, the ratio of tool length to diameter, machine specific considerations and experience.

One of the major developments of the design code that was used for these blades is that it shapes the leading edge in a manner that minimizes shock strength. The controlling feature is not the surface position but the derivatives of the surface profile. A problem

with maintaining profile tolerance is that it does not hold the surface derivatives to the design. If this design concept is to be used in real engines it will be important to investigate how tightly the surface derivatives need to be held to achieve the desired performance. Depending on the result of that investigation new methods of manufacturing, tolerancing, and measurement may need to be developed.

4.2.2 Surface Finish Tolerance

Surface finish is defined as the average deviation of the surface from a mean-line surface. The standard for surface finish, and almost all correlations between surface finish and performance, is based on a 'sand grain finish'. This is a surface that would be created by a typical casting and the value is on the order of the largest grain of the casting die material. Surfaces of machined blades are fundamentally different. These surfaces are often machined with ball endmills, because of they allow better machine dynamics and can hold tighter profile tolerances. Machining with a ball-end mill leaves cusps on the surface, see Figure 4.14. The surface finish of a machined surface is often defined as the measured roughness across these cusps. Cusp height is a function of tool radius and the distance between machine path lines; surface roughness is approximately ¼ of the cusp height.

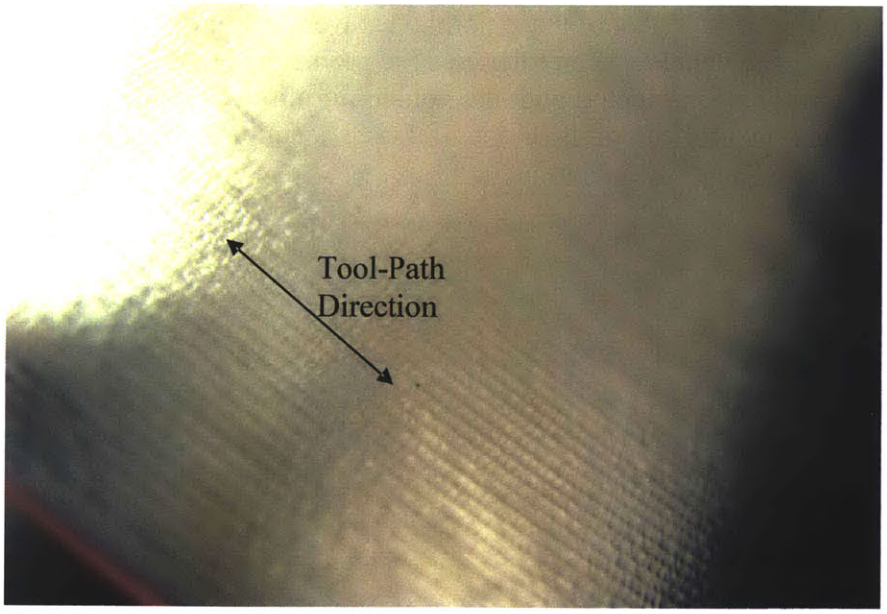

Figure 4.14: Tool markings and surface finish for Rotor One

A surface roughness of 125 μ-inches was specified for the IGV and Rotor One and 63 μ-inches for Rotor Two. This is much rougher than most engine airfoils. The rougher surface finish was chosen because it allowed for significant reductions in machine time and cost. Turbocam, the shop who machined all the blades for this project, has demonstrated that they typically achieve a surface finish of 32 μinches (close to a typical airfoil roughness) parallel to the machine lines. Turbocam was required to machine the blades so that the machine paths were parametrically spaced. This way the machine lines

approximately match flow streamlines, reducing the roughness in the direction of flow. The flow velocity perpendicular to machine lines should be small therefore the cusps should not start thicker boundary layers. An additional benefit of specifying parametric machine paths is that the heights of the blades decrease from the leading edge to the trailing edge. This results in a smoother finish, perpendicular to the cusps, at the trailing edge.

4.2.3 Non-Conformities of Manufactured Parts

The profile tolerance for the first stage was inspected through a process known as "on machine probing". A Renishaw probe was used to interrogate the surface. The blades are inspected while still on the machine so that if the blades are thick measures can be taken to correct them without additional set-ups. Points on streamlines defined the blades for production. A sampling of these definition points were used for inspection.

The drawback of on-machine-probing is that it extends the time on the machine, this makes the process expensive. Five of the first rotor's 20 blades were probed. On each blade three streamlines were probed with 7 points on each side and 4 points around the leading edge. The blades were within tolerance with the exception of the tip streamlines behind the leading edge. Most of these points that were out of tolerance were thick but because the rest of the blade was in tolerance the problem could not be fixed by taking a skim cut. The rotor was accepted with the non-conformities. Figure 4.15 shows the design intent and the probed points of one of these streamlines, Table 4.4 lists the points and their deviation from the design.

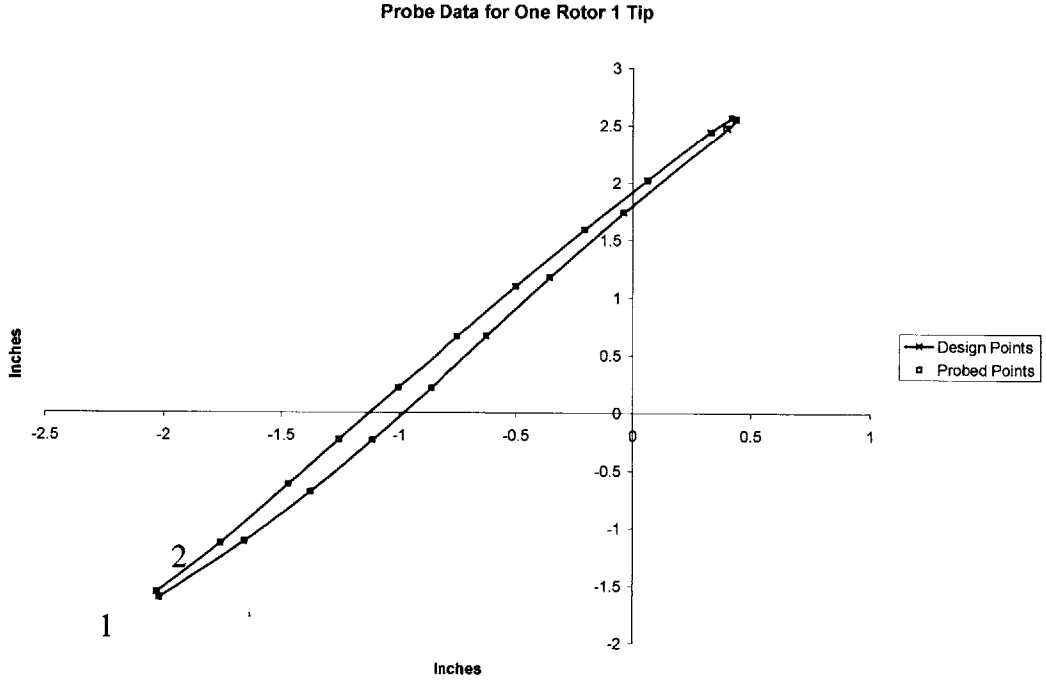

Figure 4.15: Probe data for one stream line of Rotor One

Table 4.4: Probe Data From One Streamline of Rotor One

Point Number	Deviation (in)
6	0.001
7	0.0022
8	0.0023
9	0.0038
10 (LE)	0.0064
11 (LE)	-0.0031
12 (LE)	0.0013
13 (LE)	0.0081
14 (LE)	0.0035
15	0.0023
16	0.0016
17	0.0004
18	-0.0004

4.3 Manufacturing Process for Aspirated Blades

The passage for the aspirated flow in these blades was through the root of the blade. Previous aspirated blades removed the aspiration flow through the shroud. Producing the aspirated blades for the second rotor required an orchestration of several diverse manufacturing and design disciplines including, five-axis machining, electron-beam welding, electric discharge milling, material selection and heat treatment, and finite element analysis. During the process there were multiple set-backs. This section discusses the sources and solutions to these problems, the final process for how the blades were manufactured, and how the blades would be manufactured in the future based on what the author learned from this process.

4.3.1 Challenges Associated with Aspiration

The two causes of most of the issues that were dealt with during the production process were the lean of the blades and the requirement that the aspiration flow be removed without taking it through the tips. In previous aspirated compressors the blades were shrouded and the aspiration flow was removed radially outward. Figure 4.16 is a sketch showing the pathway for the bleed flow through the blade.

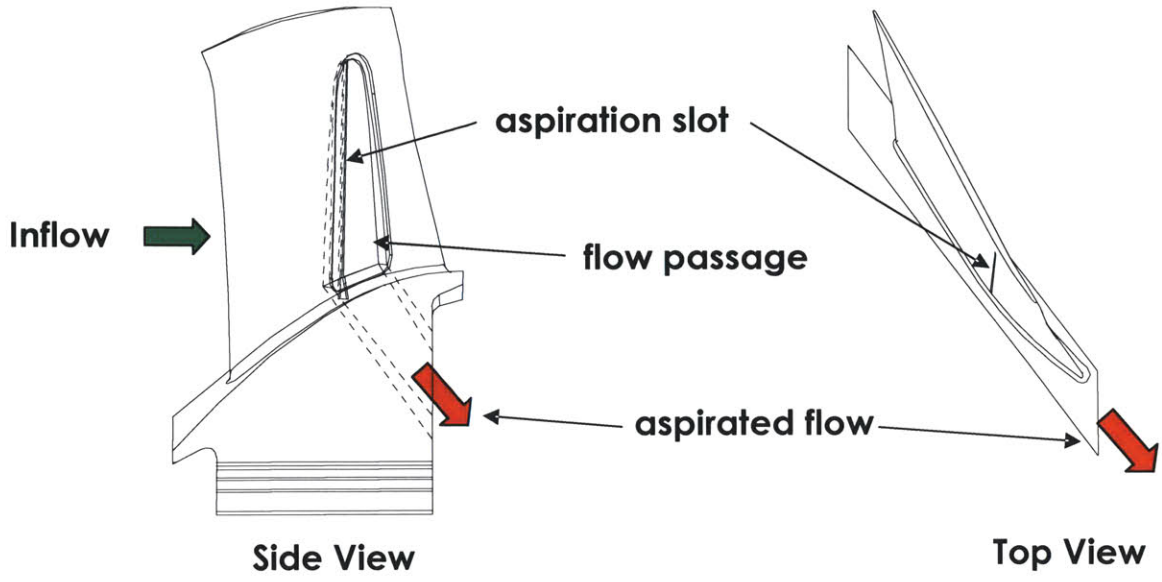

Figure 4.16: Sketch of scheme for removing aspiration flow radially inward [16]

4.3.1.1 Blade Lean and Root Stress

There is about 5° of lean in the second rotor. This lean increases the bending stress in the root, where the blade is attached to the foot. The bending stress is a result of centrifugal forces acting on the center of mass of the blade, which is not radially above the root, and the pressure difference between the pressure and suction sides of the blades. In early designs and trials the aspirated blades were to be made of aluminum. This decision was made because it was believed that using aluminum simplified the design. As a result of aluminums lower density the rotational stresses would be lower, making the design of several critical areas simpler. These areas included the dovetails where the blades fit into the disc, the root of the blade, and the passage through the blade for the bleed flow. Also aluminum would have lowered the cost of the blades through its lower material cost and better machining qualities. During the initial design of the blades it was believed that the only problem with aluminum would be its weld-ability in the electron beam process (more about e-beam welding in section 4.3.2.1). Aluminum alloy 5083 was selected for its welding properties and the experience of the vendor with it.

The problem with aluminum was that it's relatively low yield stress was unable to handle the bending stress in the thin areas of the root near the bleed passage. Throughout the design process it was known that stresses due to rotation were significant compared to the yield stress of the material at the full design speed, it was believed that the stress due to the blade loading would be negligible. During the final stress analysis, performed by Dr. F. Neumayer, it was discovered that the aero loads on the blades increased the maximum stress beyond the ultimate stress of the material. Initially it was believed that, because the highest stresses were near the bleed passage, modifying the passage and increasing minimum wall thickness on the pressure side of the blade could reduce these stresses to

acceptable levels. Figure 4.17 shows FEA results for the aluminum blade. After several iterations it was realized that because the prime contributor to the stress was a bending stress the second area moment needed to be increased, not the area. Modifying the passage only nominally changed the stress. To lower the stress levels below the yield stress would require thickening the blade, requiring a redesign of the aero. This was not an option because of schedule and budget constraints. Turbocam, the machine shop producing these blades, had already been given the geometry and invested engineering time developing the CNC programs. Changing the external blade shape would have required paying them to re-perform this work.

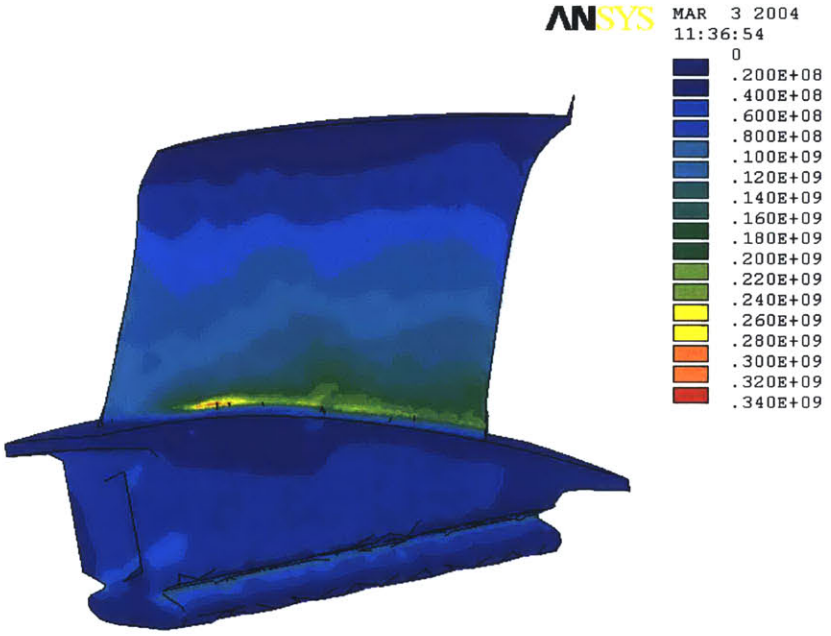

Figure 4.17: Stress in Rotor Two, Pressure Side, Alum.- Yield Stress ~120 MPa (Max 340 MPa) [18]

Instead of modifying the geometry it was decided to change the blade from aluminum to a steel alloy. The finite element analysis was done again with basic steel properties, shown in Figure 4.18. 17-4 PH with an H1150 heat treatment was selected because it's yield stress is high enough to handle the maximum predicted stress. Changing to steel doubled the weight of each blade; this in turn doubled the stress in the dovetails in the disc requiring the addition of a H1150 heat treatment of the disc to ensure that the dovetails would not fail at design speed. The e-beam welding essentially anneals the material and the weld joint is near the area of highest stress in the blade, this required that the blades be heat treated mid-way through the manufacturing process. This is discussed in greater detail in Section 4.3.2.

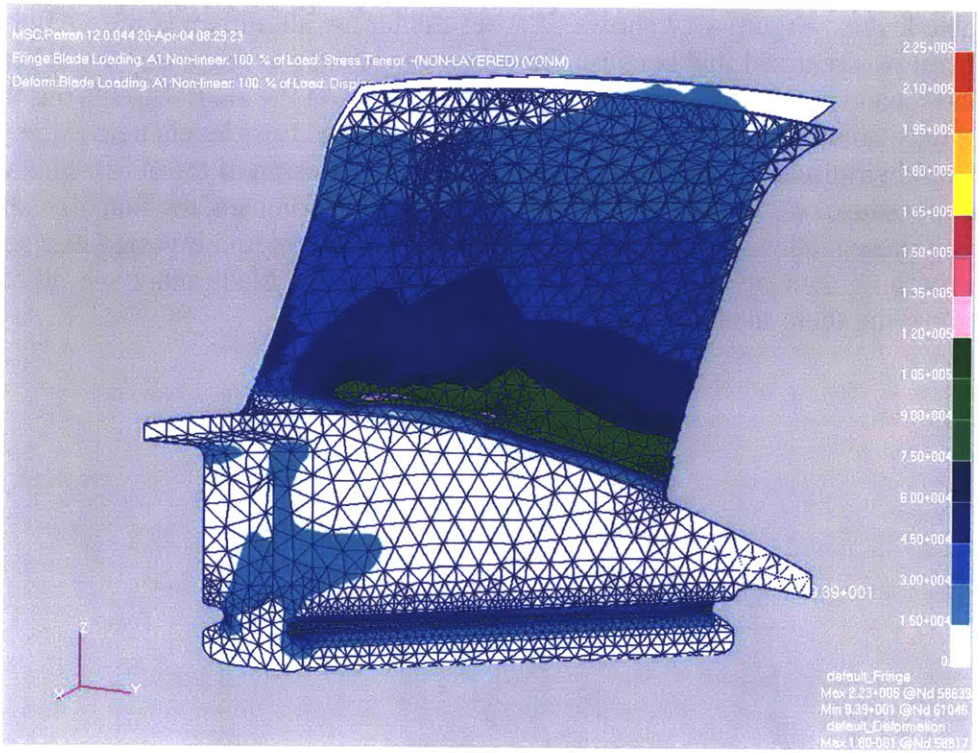

Figure 4.18: Stress in Rotor Two, Pressure Side, 17-4 PH - Yield Stress = 162 ksi (Max 150 ksi) [19]

A material option that was not given much consideration was titanium. Titanium was unattractive because it is a difficult material to machine and the development time of the manufacturing process probably would have been longer. The yield strength to density ratio of aluminum is ~$4X10^4$ m^2/s^2, for 17-4PH steel the value of this ratio is ~$1.4X10^5$ m^2/s^2, and for titanium the strength to density ratio is ~$2.7X10^5$ m^2/s^2. The components of stress due to rotation scale linearly with density thus it is evident that using titanium would have nearly halved the stress in the blades.

4.3.1.2 The Bleed Passage and Plunge EDM

The biggest difficulty in manufacturing the aspirated blades was the passage from the cavity within the blade to the back of the foot of the blade. This passage is approximately 0.080 in wide and 1.0 in long at the blade root and approximately 2 in. deep. The length to diameter ratio of a tool that could fit into this passage to break through to the cavity in the blade would have to be on the order of 30. There is simply not enough strength in tool with these dimensions to machine this passage. The chosen solution was electrical discharge milling (EDM). Electrical discharge milling removes metal by creating an electrical arc between the tool and the work-piece that erodes away the work-piece material. The tool and work-piece are immersed in a dielectric fluid. The fluid between the tool and work-piece must be continually flushed and free of particles otherwise a short circuit is created between the tool and work-piece.

The original design of the bleed passage was a passage that was convergent from the exit to where it meets the pocket inside the blade and was defined by four planes. The

reasoning was that a simple tool could be made that matched this panel, burning material with the tip and sides at the same time. This decision was made with a lack of experience with the EDM process. While the vendor tested the process it was discovered that the method for burning this geometry was to burn up through the center and then use different tools to burn the sides. This process required ~24 hours on the machine. To reduce the cycle time the passage geometry was redefined so that it is a simple projection from the blade root to the back of the foot. A second simple burn was added to widen the passage near where it exits from the foot to match the original geometry.

After changing the passage geometry there were still problems with the process. During the plunge fluid must continually flow past the tool; otherwise the burned particles create a short circuit. During the plunge there is no natural process for creating this flow. One traditional solution to this problem is to make the tool in two halves with a passage in the middle. The dielectric fluid is then pumped into the tool, comes out the center where it is burning, and exits along the exterior of the tool. This method was attempted without success. The tool was too long and thin and the pressure required to drive the flow split the tool at the tip. Attempts were made to weld the two halves of the tool together but this could not be done without bending the tool. The solution was to use EMD drilling to drill from the foot into the cavity and then burn the bleed slots. Then a fixture, connected to a pump, was placed on the side of the blade that was able to pull fluid through the holes, into the cavity, and out the bleed slots. Once this was done a solid tool was used to burn through. The first few blades were used as trials to optimize the burn time through the number and diameter of the holes.

It took between forty-five seconds and a minute to burn one hole, and about eight hours to burn the passage way. In retrospect the simplest, and quickest, way to bring the bleed flow from the internal cavity to the exit in the foot would have been to EDM drill multiple holes. This assumes that enough holes could be drilled to pass the required bleed flow and that the pressure losses across each hole would be acceptable.

4.3.2 Order of Operations

The manufacturing process for the aspirated blades was an integration of three distinct manufacturing methods and material heat treatment management. The process is described in detail below.

4.3.2.1 Rough Machining

Annealed steel is easier to machine than heat treat hardened steel and the e-beam welding process annealed the weld joint. Therefore, the steel alloy was received in an annealed state. The foot and dovetail were machined to finish dimension to create datums for future operations. The pressure side of the blade was rough machined with about 0.020 in. of stock remaining. The pocket for the bleed flow was machined to finish dimensions, as was the interior of the cover-plate for the pocket. The cover plate was also left with

about 0.020 in. of stock on the exterior. The suction side of the blade was not rough machined. In an early trial both sides of the blade were rough machined to within 0.050 of the final dimensions before the cover-plate was welded. It was discovered that there was a deflection of the blade during the weld process. There was so much deflection that the tips of the blade were no longer within the envelope of the finish blade and portions of the blade were missing. This is shown in Figure 4.19. Not rough machining the suction side of the blade left a large mass of metal that prevented deflection and created a way to dissipate more of the heat generated during the welding.

Figure 4.19: Aluminum test blade with section of leading edge due to distortion during welding

4.3.2.2 Electron-Beam Welding of the Cover-Plate

After rough machining the two pieces, blade and cover-plate, were sent to the weld vendor to be joined together. The method used for joining them together was electron-beam welding (EBW). In EBW heat generation for fusing the two pieces of material comes from a stream of electrons generated by a hot cathode and accelerated by a voltage somewhere in the range of 30,000 to 200,000 volts. Typically these beams generate heat on the order of 30 kW/mm^2. The beams are focused and directed to the work-piece by a magnetic field within a vacuum. Welding in a vacuum environment prevents oxidation in the material at the weld. The EBW process has the advantage of being able to weld through joints up to 200 mm thick. The EBW process results in a joint that is homogenous in properties with the rest of the work-piece. Since the weld join will be in or near the blade root, where stresses are highest, the homogeneous nature of an EB weld makes it very appealing for this application. [20]

The only hurdle was the location of the bottom weld. During trials it was discovered that it was difficult to control the position of the weld beam in the corner by the fillet. Both the blade and the root were at the same potential and the beam oscillated between the two. The inability to control the electron beam resulted in the porous weld shown in Figure 4.20. This required that the bottom of the cavity be moved slightly higher in the blade requiring a slightly longer EDM passage from the exit of the foot to the bottom of the cavity.

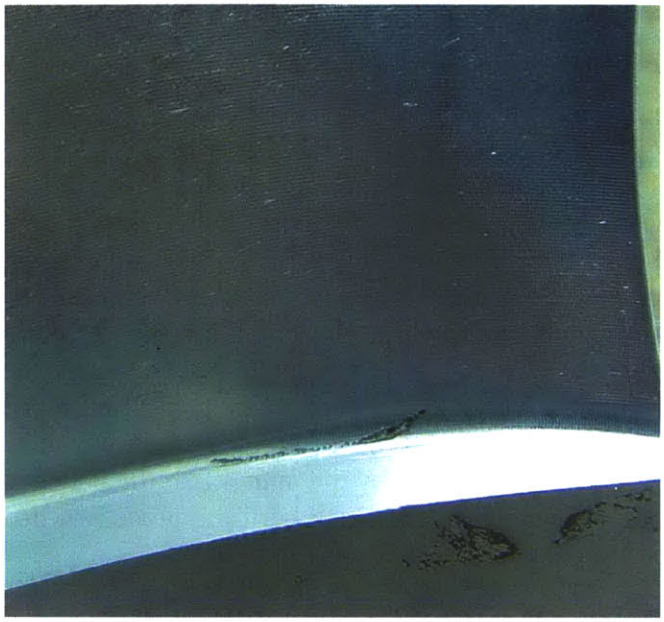

Figure 4.20: Inadequate weld joints in fillet because of control issues with the electron beam

4.3.2.3 Heat Treat

The material was received in an annealed condition and remained annealed after the welding. After the welding the blades were sent out for heat treatment and heat treated to an H1150 condition. This treatment was selected for its high yield stress and because the material remained machinable after the process.

4.3.2.4 Finish Machining

Following welding and heat treatment the blades were returned to the machine shop where they were machined to finish dimensions. Large amounts of stock, ~1/4 in. were left on the suction side of the blade to ensure that the internal pocket did not move relative to the datum planes used for alignment due to heat stresses during welding. This stock was removed first, then blades were finished with tool paths that were continuous around the blade and parametrically spaced. Similar to the first rotor the surface finish in the direction of the tool paths is better than in the span-wise direction. The surface finish in the span-wise direction was specified to be 63 μin. This is better than the specified surface finish for the first rotor because the second rotor is supersonic across the entire span and more highly loaded.

4.3.2.5 EDM Process

The final step in the manufacturing process of the aspirated blades was to EDM the aspiration slots and the passage from the back of the foot to the base of the interior pocket. As previously mentioned when plunge EDMing there must be a flow of the dielectric fluid around the tool to remove the burnt material and prevent short circuits between the tool and work-piece. This was the primary driver in deciding the order and method of the burns.

Before being placed on the CNC EDM machine several small (0.060 in. diameter) holes were ED drilled from the back of the blade foot into the internal pocket. Changing the number of pre-drilled holes changed the amount of time required to plunge the passage. The number of holes was chosen to minimize the total process time, more was not necessarily better. Next the aspiration slots were burned into the suction side of the blade on a CNC EDM machine. After this step a fixture was clamped onto the surface of the blade so low pressure could be applied to the aspiration slots and pull fluid through the drilled holes, into the blade cavity and out through the aspiration slots. This flow path was crucial to keep fluid moving past the tool as it plunged and burned the exit passage. In total the EDM processes required three different fixtures and about 10 hours per blade. As mentioned previously it is believed by the author that the better way to connect the blade cavity to the foot exit is by using the ED drilling process to drill as many holes as needed to get the proper flow area.

4.3.2.6 Assembly and Balancing

The second rotor was assembled at the GTL. Each blade was placed in a supersonic bath and then cleaned with pipe cleaners. This was to ensure that there was no debris within the aspiration passage that might be jarred loose during operation and possibly end up in the bearings. This process yielded nothing except for a little residual soot from the EDM process. After cleaning each blade was inspected and weighed. They were then placed in the disc in an order that accounted for variation in masses and resulted in a minimum imbalance. The calculated imbalance due to blade non-uniformity was 20.4 gram-inches. The rotor was then balanced on a dummy shaft in two planes so that the final imbalance was less than 1.4 gram-in. The assembled aspirated rotor is shown in Figure 4.21.

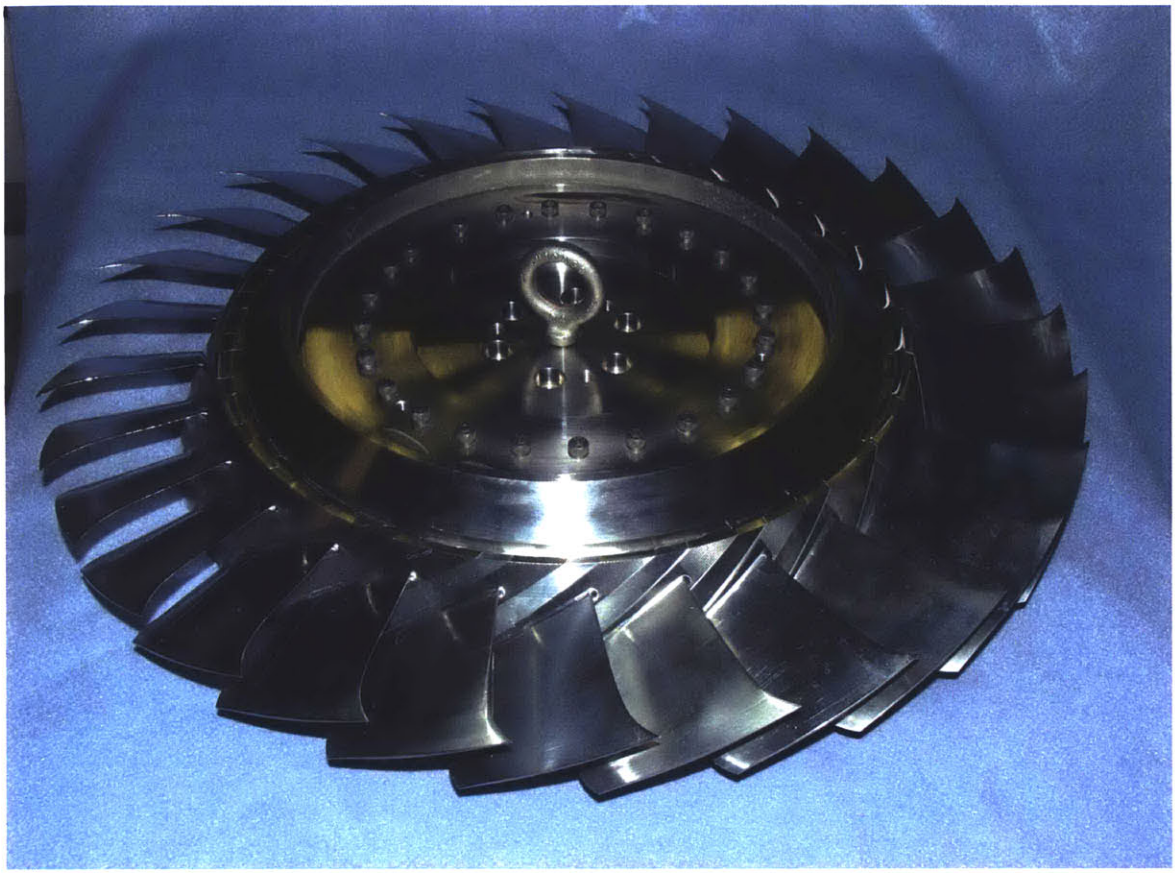

Figure 4.21: Aspirated Rotor after assembly and balance

5 Instrumentation and Data Acquisition

The primary measurement goal was to determine the adiabatic core efficiency of the compressor with less than 0.5% uncertainty. This chapter discusses the instruments and data acquisition systems used in the facility.

The efficiency of a compressor is defined as the inverse of the work required by the compressor to achieve a certain pressure ratio divided by the work required to achieve that pressure ratio in an isentropic process. If adiabatic operation and constant thermodynamic fluid properties are assumed and the working fluid is an ideal gas then the adiabatic efficiency of the compressor is:

$$\eta_C = \frac{\pi^{\frac{\gamma-1}{\gamma}} - 1}{\tau - 1} \qquad \text{Eqn. (5.1)}$$

where τ is the ratio of total temperatures and π is the ratio of total pressures. Thus to measure the efficiency the inlet and exit total temperatures and total pressures must be known. The accuracy that they must be measured with is discussed in Section 6.4.1 and detailed in [5].

5.1 Measurement Locations

Upstream of the compressor there are six instrument windows, three pairs separated by 120°. One of each pair is a window of 'singles'. These windows each contain one mid-span total temperature measurement, one mid-span low frequency total pressure measurement, one low frequency wall static pressure measurement, and at least one of the windows contains a pitot probe manufactured by United Sensor Corp., also positioned at the mid-span. In addition to these single measurements there are two span wise rakes, one that measures total temperature and another that is a low frequency total pressure measurement. The bodies of these rakes were machined so that they had an aerodynamic profile that minimizes the disturbance into the compressor.

Similar to the upstream measurement plane the downstream measurement also has six measurement windows that have the same circumferential positions as the upstream windows. Downstream of the compressor the span-wise height is 43% of the upstream annulus height. The required diameter of the heads of the downstream thermocouples results in requiring two downstream rakes to achieve similar measurement density downstream and upstream. Therefore, downstream there is only one window of singles. Figure 5.1 shows the location of all the instruments on the rig.

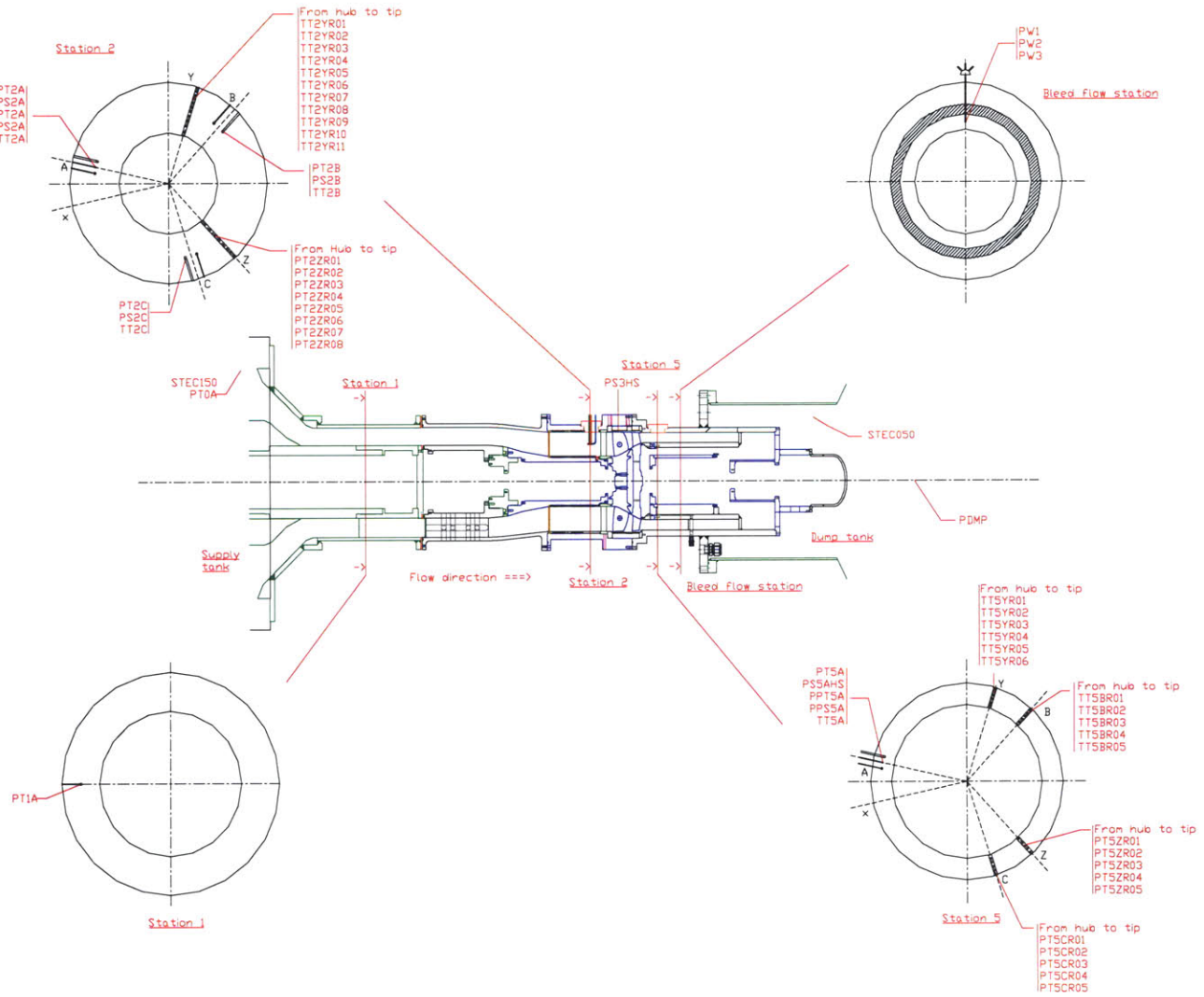

Figure 5.1: Instrument Locations in the Blowdown CRAspC Facility

In addition to these low frequency upstream and downstream measurements there are two high frequency static pressure measurements. One in on the casing between the two rotors and the other is a wall static measurement in one of the downstream instrument windows. High frequency response (~100 KHz) is achieved by fixturing the diaphragm of a .062 in. diameter Kulite pressure transducer flush with the wall.

In the bleed flow passage there is three way wedge probe to measure the total pressure and swirl in the passage. Also in this passage is a variable area orifice that was meant to choke the bleed mass flow. It was believed that with the total pressure measurement, knowledge of the swirl, and a chocked orifice an estimate of the bleed flow could be made. The first test revealed that the bleed passage was too large for the amount of bleed flow. The orifice was not choked, in fact the measured total pressure in the bleed passage was less than the pressure in the dump tank for most of the test time.

After initial tests a distortion of both the inlet total pressure and static pressure was noticed. After several runs additional inlet pitot probes were added to improve the circumferential measurement density. It is believed that the inlet distortion is due to non-uniformities in the hole pattern of the pressure screen. The analysis of this problem is discussed in Section 6.3.

5.2 Temperature Probes

The temperature transducers used in this facility were designed and built in the GTL. The probes are made of 0.0005 in. diameter type K thermocouple wire. The thermocouple beads are mounted within heads with vent holes that slow the flow enough to protect the fragile bead, provide adequate time response and reduce errors. The temperature probes were shown to be accurate to at least 0.3 K throughout the operational range and demonstrated a response time of better than 30 ms. Details about the design, manufacture, calibration and operation of the thermocouples used in this rig can be found in JF Onnee's master's thesis [5].

5.3 Pressure Probes

Probes that measure total pressure, wall static pressure, and pitot probes that measure static and total pressure at one location are placed throughout the facility, as seen in Figure 5.1.

5.3.1 Rated Transducer Properties

All of the pressure transducers used on the rig, both for the high frequency response and the low frequency response probes, are XCQ-062 transducers manufactured Kulite. These probes have a rated response frequency of better than 200 KHz. These transducers measure the pressure difference between the pressure being measured and a variable reference pressure behind the transducer membrane. A vacuum pump is used to set the reference pressure of all the transducers at ~0 psia. Transducers with pressure difference ranges of 15 PSI and 50 PSI were used in the facility. The rated linearity and

repeatability of the relationship between pressure difference and voltage of the transducers is 0.1 % of the transducer range [21]. Details of how the transducers where qualified can be found in Appendix C.

The zeros of Kulite transducers have been shown to drift with temperature [25]. The transducers used in the facility were temperature compensated between 70°F and -350°F (294°K to 61°K). Work by prior investigators has shown that the drift of Kulite transducers can be as much as 2.5% but for the low frequency probes, with the transducers mounted externally to the facility, the temperature at the face of the probe does not vary much from room temperature [25]. Initially during a test the tubes that carry pressure from the probe head to the transducer are evacuated. After the valve opens they are filled with gas that is nearly room temperature. After the initial fill there is no flow within the tubes thus to change the temperature of the transducer heat must be transferred either along the gas column or through the steel of the tubes. The time scale for this is L^2/α, with the minimum L being ~3 inches. For the gas column $\alpha = \kappa/(\rho \cdot C_p)$ $\alpha \sim 1.4 \times 10^{-5}$ m^2/s and for the steel $\alpha \sim 3.5 \times 10^{-6}$ m^2/s. Thus, the time scales for heat transfer are ~ 6 minutes for the gas column and ~ 27 minutes for the steel passage. Because it is assumed there is no temperature variation of the transducer the effect of temperature changes on the transducers was not measured.

5.3.2 Total Pressure Rake Design

The pressure rakes upstream and down stream are extremely similar. Both use the same impact head, steel tubing, and blade profile. The difference is in the number of heads per rake and the ability of the downstream rakes to be rotated ±15° to adjust them to the different levels of swirl at different corrected speeds. Figure 5.3 is a side view of one of the aft rakes with the impact tubes and heads exposed. For the upstream rake the number of impact heads was determined by the thickness of the profile and the number of steel tubes that could be fit into the cross section. Figure 5.2 is a cross section of the upstream rake that shows how the outer diameter of the tubes, combined with the dimension of the cross-section, limits the number of upstream pressure probes. For a sense of scale in these two figures the outer diameter of the tubing is 0.094 in.

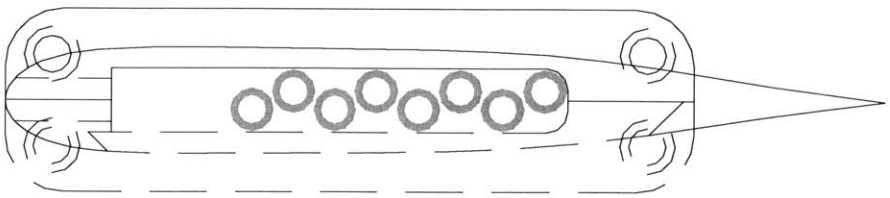

Figure 5.2: Cross-Section view of pressure tubes within the Upstream Rake

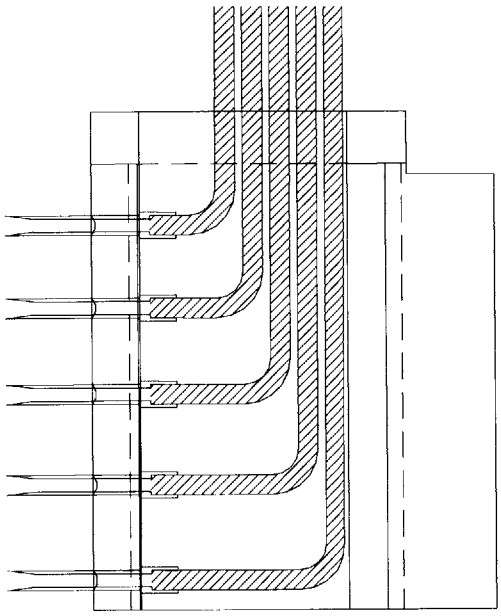

Figure 5.3: Sketch showing impact heads and tubes of a Downstream Rake

The inlet of the impact heads was designed to precisely measure the total pressure of the flow even if the flow was not aligned with the axis of the probe. According to the CFD results the swirl exiting Rotor Two could vary 5°-10° across the span. The 15° bevel on the inlet of the impact heads provide a range 27.5° of misalignment between the flow and the probe where the uncertainty in total pressure measurement is less than 1% of the velocity head [23]. The analytical form of this error is Equation 5.2.

$$\frac{U_{Pt}}{P_t} = \frac{1/2 \cdot \rho \cdot v^2}{P_t} \cdot 1\% = \frac{\gamma \cdot M^2}{2 \cdot \left(1 + \frac{\gamma - 1}{2} M^2\right)^{\frac{\gamma}{\gamma - 1}}} \cdot 1\% \qquad \text{Eqn. (5.2)}$$

5.3.3 Pitot Pressure Probes

Pitot probes are used to measure the static pressure and total pressure at a point. These probes are manufactured by United Sensor Corp and shown in Figure 5.4. According to the calibration curves provided by United Sensor Corp a conservative estimate of errors due to alignment and Mach number reveal that the error in total and static pressures are 1% of the velocity head [24]. The form for the relative uncertainty in static pressure based on Mach number is shown in Equation 5.3; Equation 5.2 is the uncertainty for the total pressure measurement of the pitot probes. Table C.1 in Appendix C shows the uncertainty in pressure measurement due to probe geometry for several runs.

$$\frac{U_{Ps}}{P_s} = \frac{1/2 \cdot \rho \cdot v^2}{P_s} \cdot 1\% = \frac{\gamma \cdot M^2}{2} \cdot 1\% \qquad \text{Eqn. (5.3)}$$

Figure 5.4: United Sensor Pitot Probe [24]

5.3.4 Wall Static Pressure Taps

Figure 5.5 is a sketch of the method for measuring the wall static pressure. This method assumes that the static pressure through the boundary layer is constant and that the diameter of the hole is small enough that the flow does not turn into it. Analyzing data from the runs shows a difference between the wall static pressure measurement and the mid-stream static pressure measurement from the pitot probes. Figure 5.6 is the unfiltered readings from every upstream static pressure measurement between 250 ms and 350 ms for Run 014. Figure 5.7 shows the difference between the wall static pressure measurement and the pitot static pressure measurement at each window normalized by the pitot static pressure measurement at each window. For each window the static pressure measurement at the wall is higher than the mid-stream static pressure measurement. In theory, if the flow is uniform, the static pressure measurement should be the same across the span. One theory for the wall static pressure measurement being higher than the mid-stream measurement is that a component of the velocity head could be entering the static pressure hole, increasing the measured static pressure. Alternatively, there is a circumferential variation of static pressure that seems to be related to variations in the percent open area of the pressure screen, the screen might also be creating span-wise variations of the static pressure.

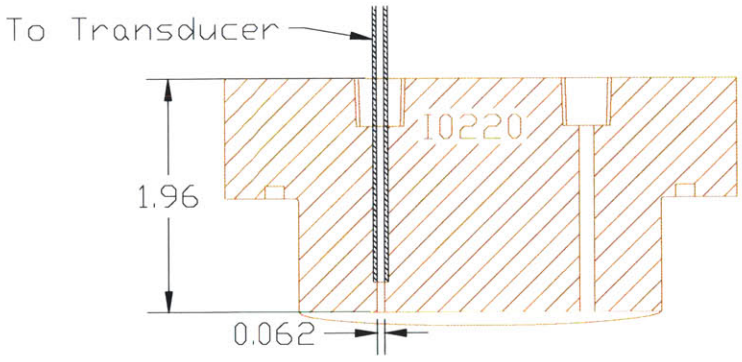

Figure 5.5: Wall static pressure taps, dimensions in inches.

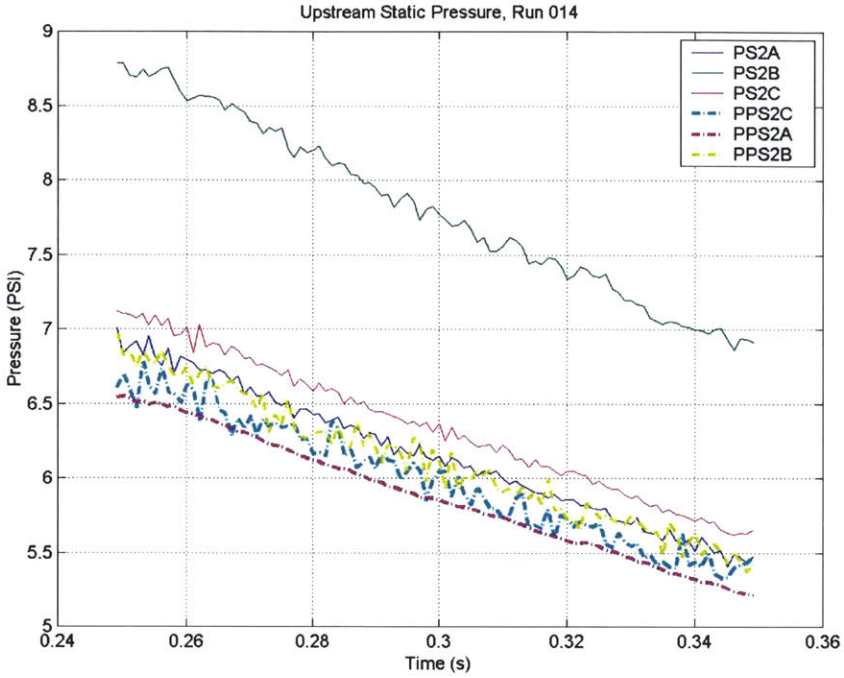

Figure 5.6: Upstream static pressure measurement for Run 014

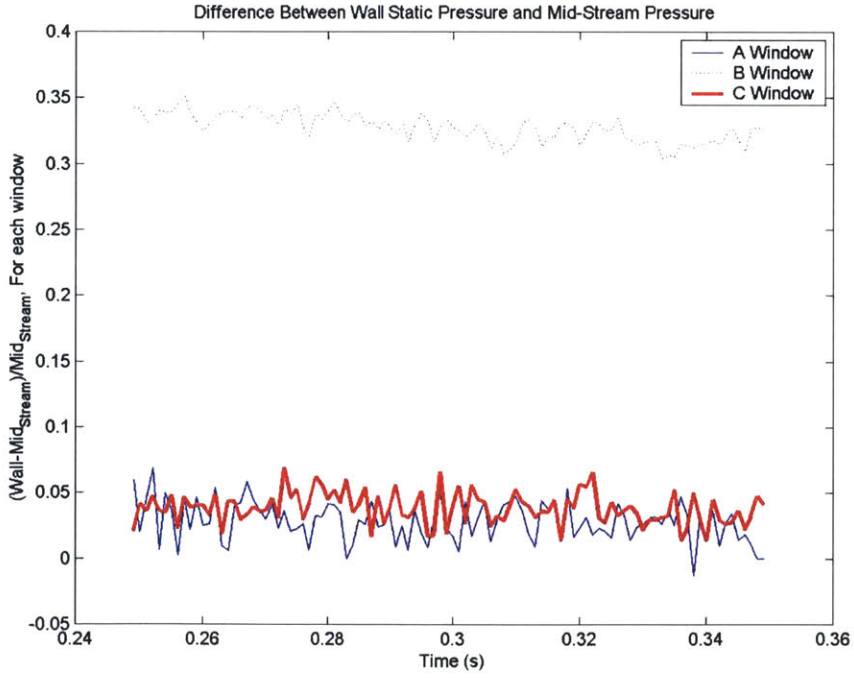

Figure 5.7: Difference in upstream static pressures normalized by the pitot static pressure, Run 014

5.4 Data Acquisition System

In early 1970's recording the data of blowdown compressor tests required high speed tapes, multiple A/D systems and computers, and careful analysis to ensure that all the data was on the same time scale. Retrieving and backing up the data required hours. Currently, technological advances allow the use of one computer for all the A/D cards in the facility. Retrieving and backing up the data for one run now requires ~90 seconds.

There are three different A/D systems used in the facility. There are two 'low-speed' cards (1 KHz), one 'high-speed' card (100 KHz), and one 80 MHz counter card.

5.4.1 Low-Speed A/D Cards

Two 16-bit National Instrument model PCI-6031E A/D cards are used to record the low frequency 'steady-state' pressure and temperature measurements. Each card has 64 channels and can sample the data at 1 KHz [22]. One card is dedicated to pressure measurements and the other card is dedicated to temperature measurements.

5.4.2 High Speed A/D Card

There is one high speed A/D card to capture the data from the two wall mounted high frequency static pressure probes. This card is an 8 channel 16-bit National Instruments PCI-6143. It has a maximum sampling rate of 250 KHz [22]. The sampling rate is set to 100 KHz during tests and two seconds of data is recorded. Also attached to this card is a once-per-rev signal from each rotor. This signal is used as a backup for rotor speed measurement and to provide a time base for rotor revolution based averaging.

5.4.3 80 MHz Counter Card

Finally, there is an 8-channel 32-bit 80 MHz counter card that is used to measure rotor speed. This card is model PCI-6602, made by National Instruments [22]. The input to the card is the full encoder signal (16 pulses per blade) and the output is the number of 80 MHz pulses between encoder pulses. In essence this provides a time between pulses thus the speed of the rotor is the angle between two pulses divided by the time between those pulses.

6 Facility Operation and Initial Results

To date fourteen tests have been run in the blowdown facility. These tests have provided insight into both the performance of the compressor and general principals for how to operate the facility. Section 6.2 discusses the experience learned about how the facility reacted to changes in initial conditions and the interactions observed between the two rotors. Also discussed in this chapter are the results from the initial tests and the uncertainty in the reported performance variables. Appendix D outlines the order of operations for a blowdown test.

6.1 Data Reduction Methods

During the test a limited number of parameters are measured, from these measurements the flow properties of interest are inferred. How the data is treated, along with the methods used for computing the flow properties influence the confidence in the final reported values. This section will discuss how the data is treated. Section 6.3 discusses the how the uncertainty in the measurements is propagated into the reported values. Appendix E examines all the data channels for a single run (Run 013) and then discusses the analysis process and how the test time is established.

6.1.1 Filtering

With the exception of the two high frequency static pressure measurements behind each rotor the purpose of the instrumentation on the rig is to measure the steady-state performance of the compressor. To remove high frequency instrument noise (some of it 60 Hz electrical hum) and non-steady flow structures measured by the instruments all of the low frequency data channels are digitally filtered before the data is reduced. The filter is a running 17 point average. At a 1000 Hz sampling rate 17 points are required to cover one 60 Hz cycle. This running average is done forward and backwards so that the phase lag of the filtered data is zero. Filtering in the forward direction, then the backward direction effectively creates at 34 point running average and everything above 30 Hz is attenuated. To test this filter a random set of data was generated and put through the filter. The original data, and the filtered data, were analyzed with a Discrete Fourier Transform. The response of the filtered data, compared to the response of the random data, is shown in Figure 6.1. Frequencies below 10 Hz are not modified by the filter. Above 10 Hz the filter attenuates the data at a rate of 20 dB per decade. Before entering the A/D cards some of the low frequency pressure transducer amplifiers have electronic 3-pole low pass filters with a break frequency of 500 Hz. The other amplifiers do nothing to modify the frequency spectrum of the signal before entering the A/D.

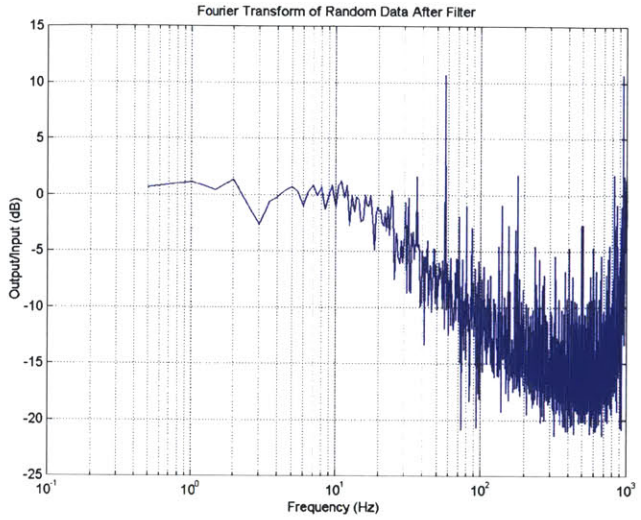

Figure 6.1: Response of random data to the digital filter used in data analysis

6.1.2 Corrected Flow

Between the pressure screen and the first rotor there are three circumferential measurement stations, all in the same axial plane. At each of these locations the total pressure, total temperature, and static pressure is measured. The static pressure is measured with both pitot probes in the center of the flow, and with wall static pressure taps. The wall static taps are not used in calculations because of the uncertainties discussed in Section 5.3.4.

For each measurement window the mass flow is estimated. First, the static temperature is inferred from the total temperature, total pressure, and static pressure. The total temperature and pressure are defined as the temperature and pressure of a fluid particle in the flow that is brought to zero velocity by an isentropic process. This isentropic constraint, along with table of gas properties [26], is used to estimate the static temperature. A Matlab© function was written that interrogates a properties table at the total temperature and total pressure. Once the entropy of the flow is known the function essentially moves along a line of constant entropy until the static temperature is found, such that $entropy(T_S, P_S) = entropy(T_T, P_T)$.

Once the static temperature is known the properties such as density, speed of sound, viscosity, enthalpy, and the ratio of specific heats come directly from the property tables. The last parameter that needs to be calculated to define the corrected flow is the velocity. The velocity is calculated as follows:

$$h = enthalpy(T_S, P_S)$$

$$h_0 = enthalpy(T_T, P_T) = h + \frac{v^2}{2} \qquad \text{Eqn (6.1)}$$

$$v = \sqrt{2 \cdot (h_0 - h)}$$

The mass flow ($\dot{m} = \rho \cdot A_c \cdot v$) is calculated for each window assuming that the total pressure, total temperature, and static pressure are constant radially and circumferentially within the 120° window. The average upstream conditions, mass flow, Mach number, density, etc. are then calculated as an average of these parameters from each window, weighted by the mass flow for each window. It is important to note that there is a four percent variation in the total pressure of the 'A' window compared to the 'B' and 'C' windows. This inlet distortion is discussed in detail in Section 6.3. Figures 6.2-6.4 show the pressures, mass flows, and corrected flows, respectively for each window during the test time in Run 013.

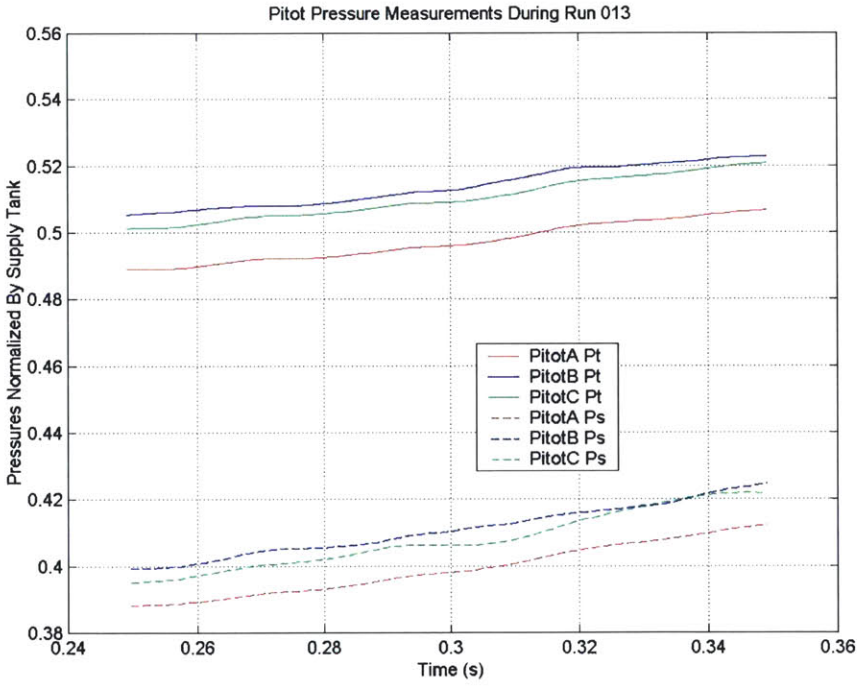

Figure 6.2: Total and Static Pressures for each window in Run 013

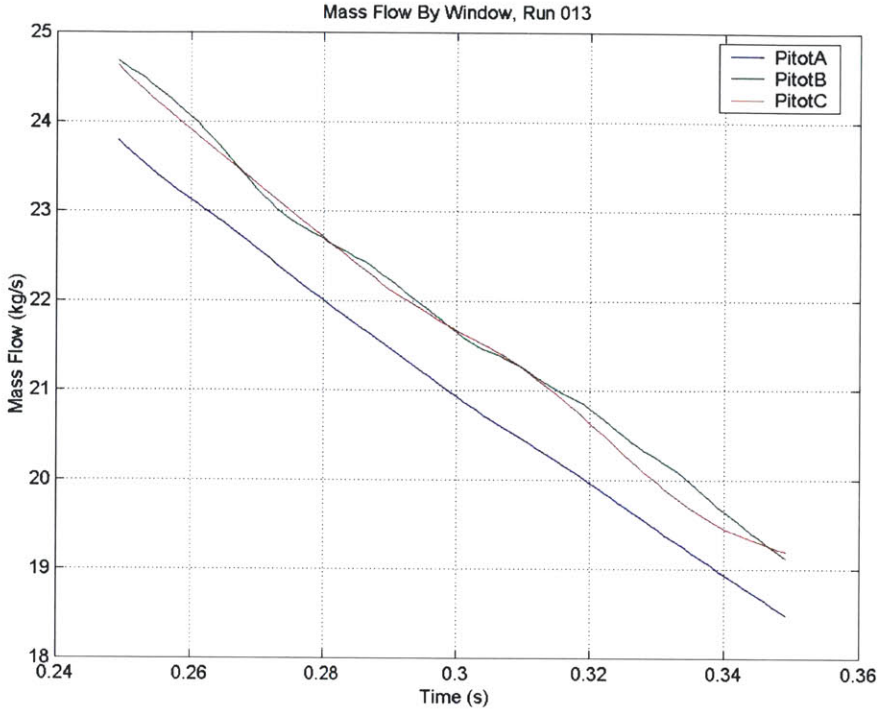

Figure 6.3: Mass flow for each window during Run 013

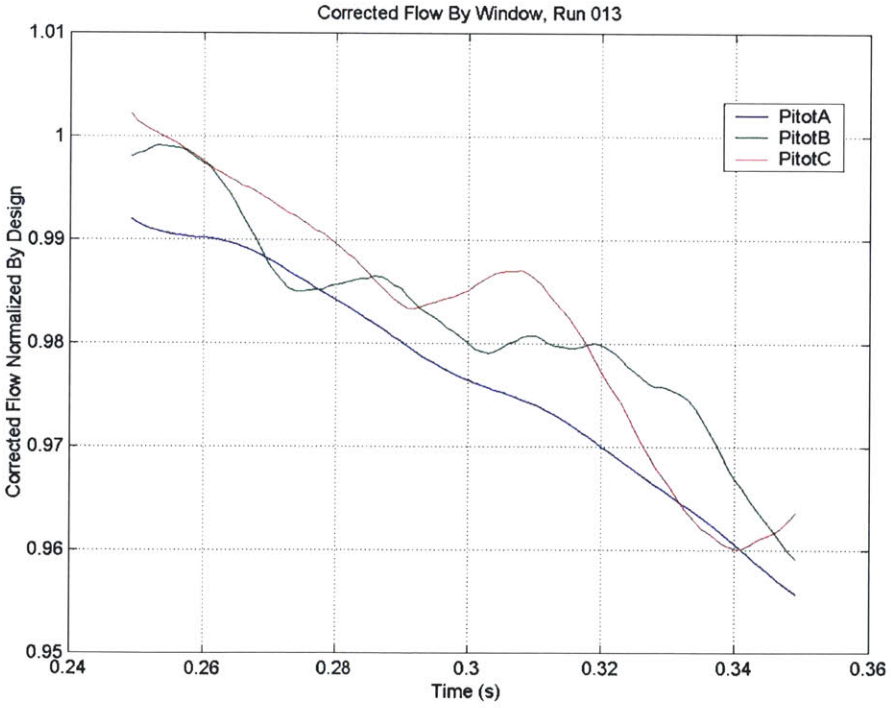

Figure 6.4: Corrected Flow by Window for Run 013

6.1.3 Efficiency

The adiabatic core efficiency numbers reported in Section 6.5 are 'area averaged' values. In the upstream measurement plane the measured values of the total pressure and total temperature rakes are assumed to be constant circumferentially. In the radial direction the measured values are assumed to be constant between measurement positions. Total pressure and temperature are averaged upstream with each measurement given a weight proportional to the area that it is measuring. Downstream the total pressure and total temperature measurements are area averaged with the same assumptions. Figure 6.5 shows the downstream total pressure measurements for Run 007 and the assumed profile used for area averaging. The author would have preferred to mass average the upstream and downstream measurements but there was no practical way to measure the downstream static pressure profile thus there is not any information about downstream mass flow. With the area averaged upstream and downstream total pressure and total temperature measurements the NIST tables are used to determine the total enthalpy and entropy into the compressor and then the total enthalpy out of the compressor and the total exit enthalpy of a compressor that operated isentropically. The core efficiency is the calculated from:

$$\eta = \frac{h_{0\_exit\_Isen} - h_{0\_in}}{h_{0\_exit} - h_{0\_in}} \qquad \text{Eqn. 6.2}$$

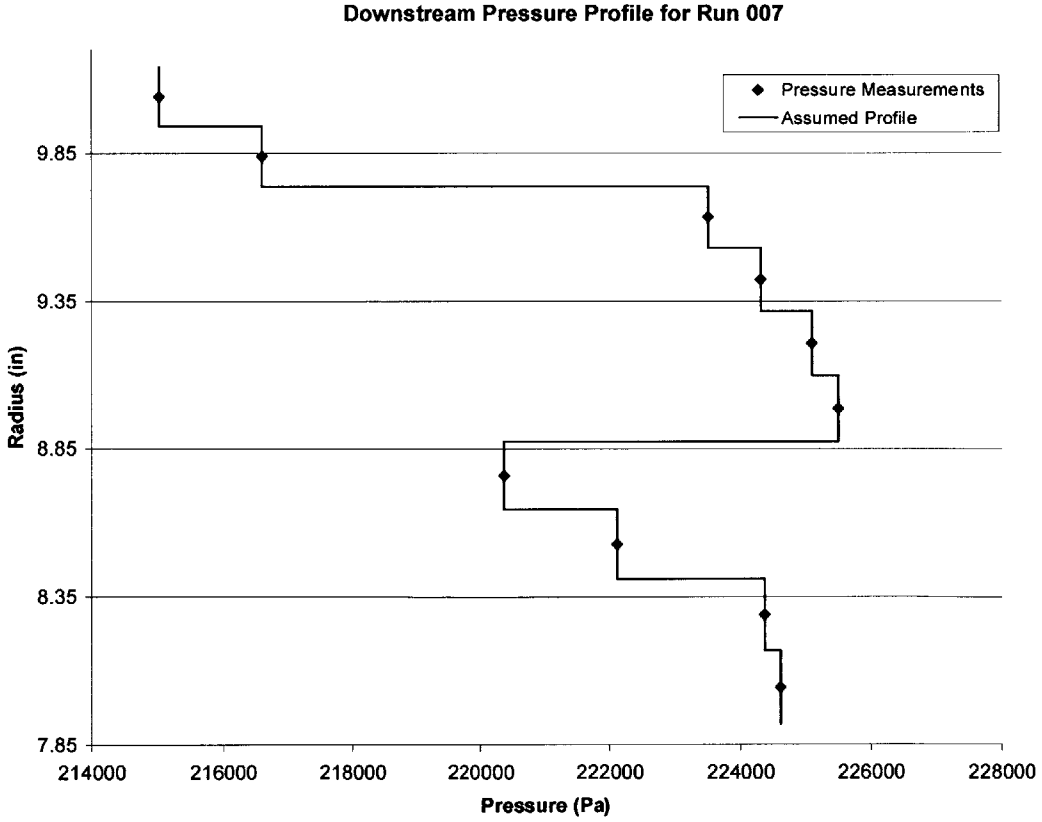

Figure 6.5: Assumed profile for area averaging

6.2 *Facility Operation*

Trying to measure a specific operating condition with this facility is difficult. It must be noted that in the blowdown facility there is no control of the compressor while it is running. Initial conditions must be set so that between 250 and 350 ms the compressor is operating where desired. There are only four variables that can be set. These are the initial supply tank pressure, the initial speed, and the open area of the throttle between the exit of the two rotors and the dump tank. When the facility was designed it was scaled to the design point of the compressor. This section discusses the effect of the scaling when operating the compressor in off design conditions.

6.2.1 Operational Constraints Due to Inertia Ratios

As described in Section 2.2.2, in order to maintain the corrected speed constant during a test the deceleration of the rotor must match the square root of the change in inlet temperature. The rotor deceleration is very dependant on the inertia of the rotational system. The inertia of the two rotating systems is fixed. Therefore, to keep both rotors at a constant corrected speed the ratio of work for the two rotors must match the ratio of inertia of the two rotating systems. The result is that a finite number of points on the map can be tested.

This principle was seen during early tests as the throttle was changed to get to the design throttle position. As the throttle is opened the back pressure on the second rotor decreases and the total pressure ratio across the second rotor, along with the energy it puts into the fluid, decreases. This means that if the initial pressure in the tank is correct for a given operating point, and the initial speeds of the two rotors are correct, but the throttle is too open, then after the initial transient the corrected speeds will match the desired condition, and rotor one will have a relatively constant corrected speed but rotor two will increase in corrected speed during the test time. This is shown in Figure 6.6. Figure 6.6 is the corrected speeds, normalized by the design corrected speeds, during Run 005. (In Figures 6.6-6.8 there are bumps in the corrected speed, these are related to changes in total temperature.) Run 005 was an attempt at a 90%-90% run, the initial speed of rotor two was low and the throttle was too open. For Run 006 the initial speed of rotor two was increased and the throttle was closed. The corrected speeds for this run are shown in Figure 6.7. Examining Figure 6.7 shows that the corrected speed of rotor two is still increasing, although at a slower rate than in Run 005, and the corrected speed of rotor two still did not match the corrected speed of rotor one at 250 ms. The reason the corrected speed still increased was because the caution was used in closing the throttle. It was closed incrementally to avoid stalling the second rotor at the beginning of the test. The initial speed of rotor two was adjusted linearly from Run 005 to Run 006 to match the normalized rotor one corrected speed. The corrected speed of rotor two was low at 250 ms in Run 006 because closing the throttle increased the work done by the second rotor during the transient therefore lowering the corrected speed at 250 ms during Run

006. From Run 006 to Run 007 the throttle was further closed and the initial speed was again increased. The corrected speeds for Run 007 are shown in Figure 6.8. In Run 007 the normalized corrected speeds of both rotors were matched to 90% of their design speeds, and during the test time (250 ms to 350 ms) the normalized corrected speeds did not deviate from 90% by more than 0.5%.

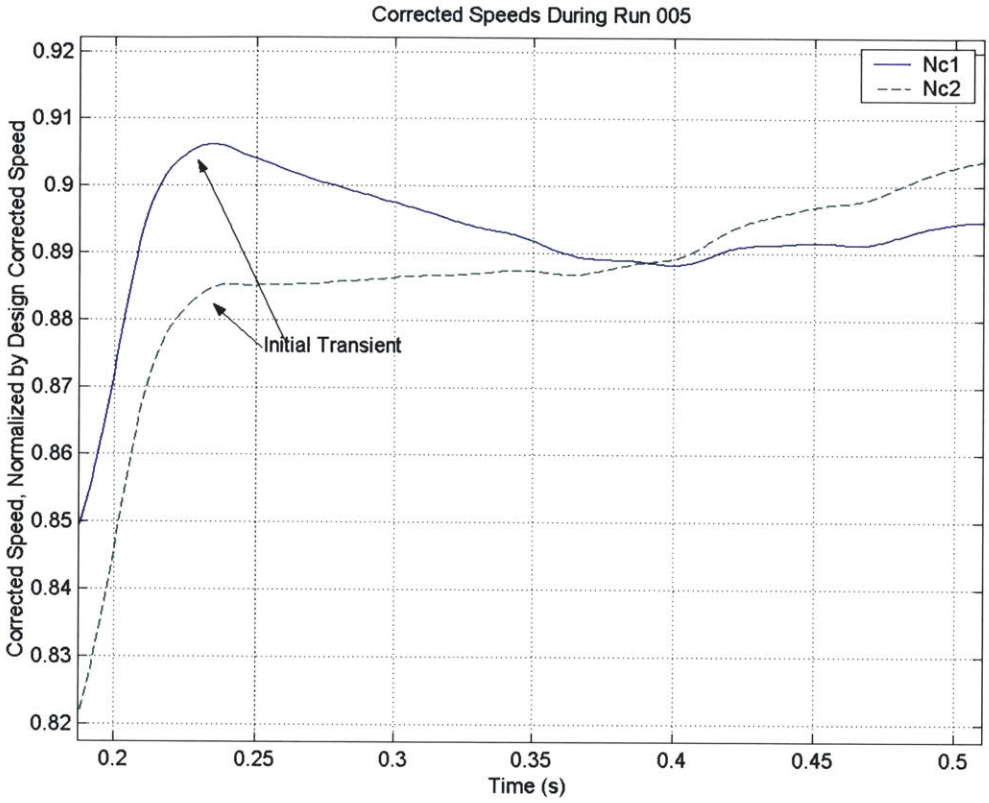

Figure 6.6: Corrected Speeds for Run 005

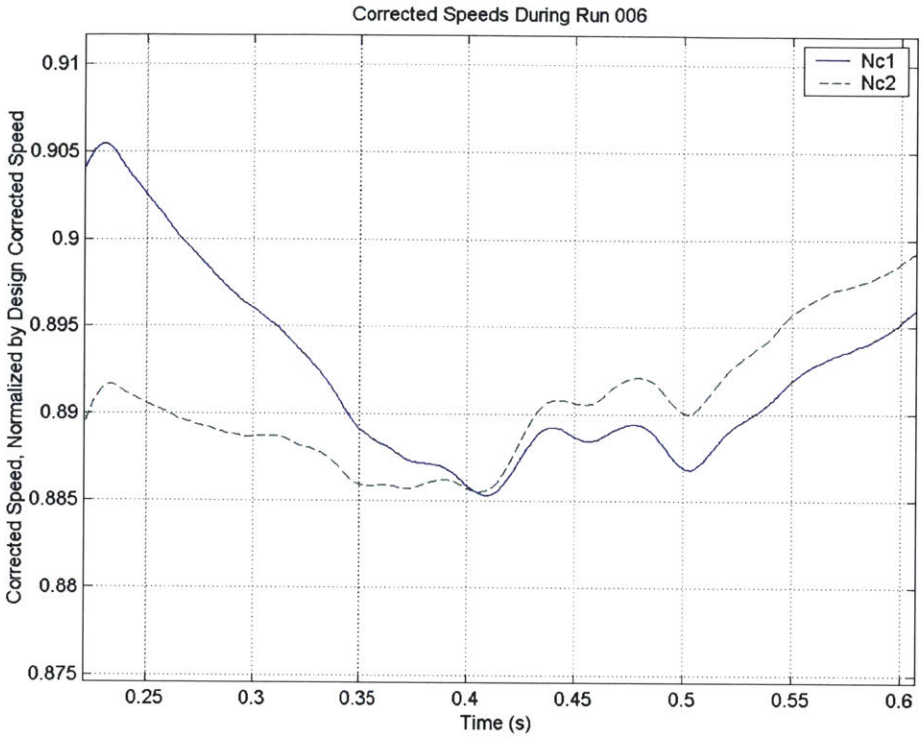

Figure 6.7: Corrected Speeds for Run 006

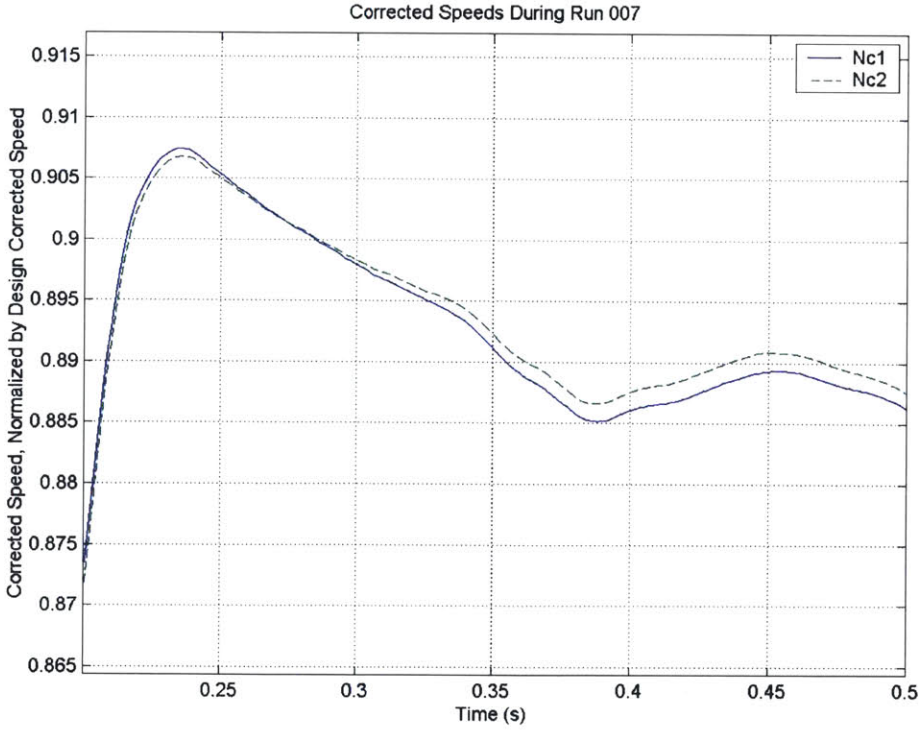

Figure 6.8: Corrected Speeds for Run 007

6.2.2 Throttle Behavior

Before any tests were run the throttle behavior was modeled as a choked orifice in a one dimensional flow. The mass flow through the throttle was modeled with the following relationship, which assumes an ideal gas:

$$\dot{m} = \frac{f(\gamma, M) \cdot A \cdot P_0}{\sqrt{R_g \cdot T_0}}$$

$$f(\gamma, M) = \frac{\sqrt{\gamma} M}{(1 + \frac{\gamma - 1}{2} M^2)^{\frac{\gamma+1}{2\gamma-2}}} \qquad \text{(Eqn. 6.3)}$$

Equating the mass flow into the compressor to the mass flow through the throttle (accurate to ~1% due to the bleed flow) gives that the ratio of throttle area to inlet area as:

$$\frac{A_T}{A_{in}} = \frac{f(\gamma_{in}, M_{in}) \cdot \sqrt{TR}}{f(\gamma_T, 1) \cdot PR} \qquad \text{(Eqn. 6.4)}$$

As gasses pass through an orifice it constricts and the effective area of the orifice is less than the physical area. The ratio of the effective area to the physical area is known as the discharge coefficient. A conservative discharge coefficient was applied to the throttle area to avoid setting the throttle area too small and stalling the compressor. There are several problems with this model. First, the flow is not an ideal gas, especially upstream were the gas becomes very cold. More importantly there are several flow features that are not contained in the one dimensional model. As shown in Figure 3.7 the flow exiting the compressor has to make a 90° turn into the dump tank, which leads to pressure head losses, and there is swirl in flow coming out of rotor two.

Despite the inadequacies of the model the discharge coefficient is consistent enough to be useful for setting the throttle. Table 6.1 shows the discharge coefficient for several runs and the operating condition of the compressor. For small changes in operating conditions (~5% in speeds or pressure ratio) the model is consistent to within ~2%-3%. Larger changes in operating conditions result in 5%-7% variation in the discharge coefficient. When deciding the throttle setting from one run to the next the inlet flow was assumed to remain constant and Equation 6.5 was manipulated to the form of Eqn 6.5, where values for Run(i+1) are desired values.

$$\frac{A_{T\_Run(i+1)}}{A_{T\_Run(i)}} = \frac{PR_{Run(i+1)} \cdot \sqrt{TR_{Run(i)}}}{\sqrt{TR_{Run(i+1)}} \cdot PR_{Run(i)}} \qquad \text{Eqn (6.5)}$$

Table 6.1: Variations of the discharge coefficient model

Run	Throttle Setting (in2)	Wc	Nc Rotor 1	Nc Rotor 2	PR	Discharge Coeff.
005	98.15	81.9%	89.9%	88.7%	1.98	98.3%
006	88.88	81.5%	89.7%	88.9%	2.10	102.6%
007	82.44	80.2%	90.0%	90.0%	2.30	100.7%
008	82.44	83.3%	93.2%	92.8%	2.47	98.6%
009	82.44	92.3%	99.5%	104.8%	2.97	91.0%
010	82.44	92.5%	100.5%	100.6%	2.91	93.0%
011	78.44	87.9%	100.4%	100.5%	2.90	94.9%
013	86.58	98.2%	101.5%	101.5%	2.91	96.2%
014	90.68	100.6%	101.7%	102.1%	2.84	96.4%
*Corrected flow and corrected speed values are normalized by the design value						

6.2.3 Rotor Interactions

It is very important to note the two rotors are highly coupled. If one attempts to consider operating points as two rotors operating independently, each with their own map, then important rotor interactions could be ignored. Thinking about the maps of each compressor only works if the interactions between the two rotors are also considered. There is no stator between the two rotors, so the swirl into the second rotor is dependant on the speed of rotor one. At the design corrected speed the first rotor is supersonic across nearly the entire span, therefore, to first order the corrected speed of rotor one sets the corrected flow entering it. Similarly the second rotor is fully supersonic across its entire span. Therefore, Rotor Two also sets its corrected flow, thus it acts as a throttle on the first rotor. For a given rotor one corrected speed there is a corrected speed for the second rotor where the flows match. Increasing the speed of rotor two from this set speed will lower the static to total pressure ratio of Rotor One, dropping its operating point. Similarly, if the corrected speed of the second rotor is decreased, then the static to total pressure ratio of rotor one will increase, pushing it further towards stall. This is shown in Figure 6.9. Run 009 and Run 010 had essentially the same Rotor One corrected speed (100%) and throttle setting. In Run 009 the corrected speed of Rotor Two was 5% above design, decreasing the speed of Rotor Two increased the backpressure of Rotor One.

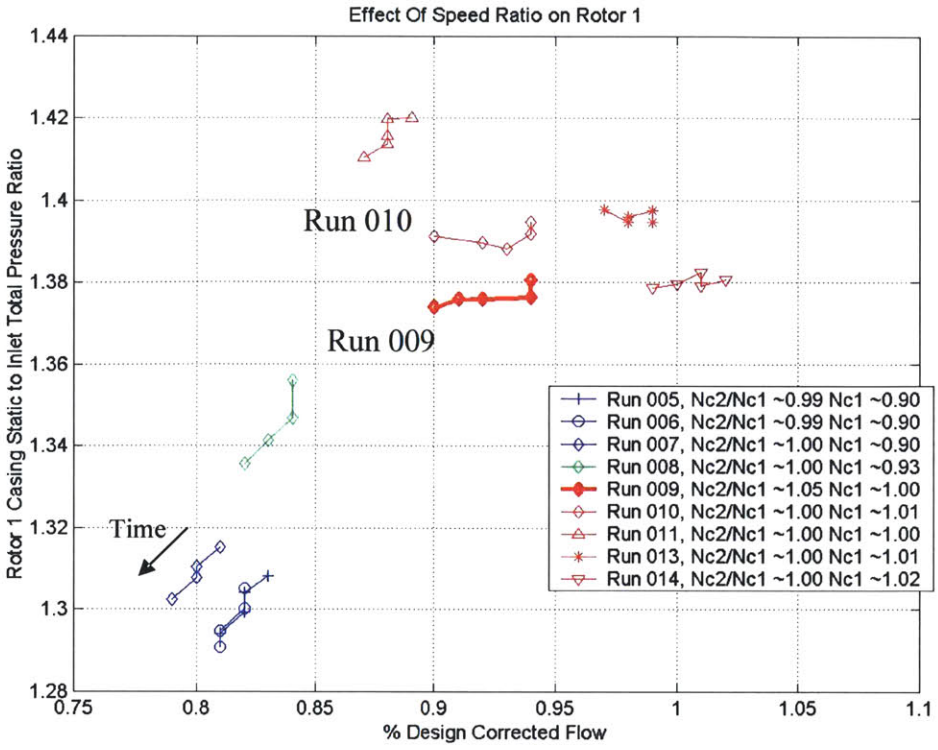

Figure 6.9: Throttling effect of Rotor Two on Rotor One

6.3 Inlet Distortion

An important aspect of testing the steady-state performance of the compressor at the design point is that the flow entering the compressor needs to be uniform in total pressure and total temperature. Unfortunately, neither of these is uniform. This section discusses the thermal boundary layers and the inlet pressure distortion.

6.3.1 Thermal Boundary Layers

In the radial direction there are hot boundary layers due to the fact that the gas is cold (~260 K) relative to the metal of the rig (~300 K). The mass of the rig, combined with the blowdown time scale, results in a nearly constant metal temperature but the gas temperature drops. This means that the thermal boundary layers grow during the test time. Typically the magnitude of the thermal distortion increases from ~1% of the center gas temperature at 250 ms to ~3% of the center gas temperature at 350 ms. Figure 6.10 is the inlet total temperature during Run 010 normalized by the total temperature at the center of the flow at each time.

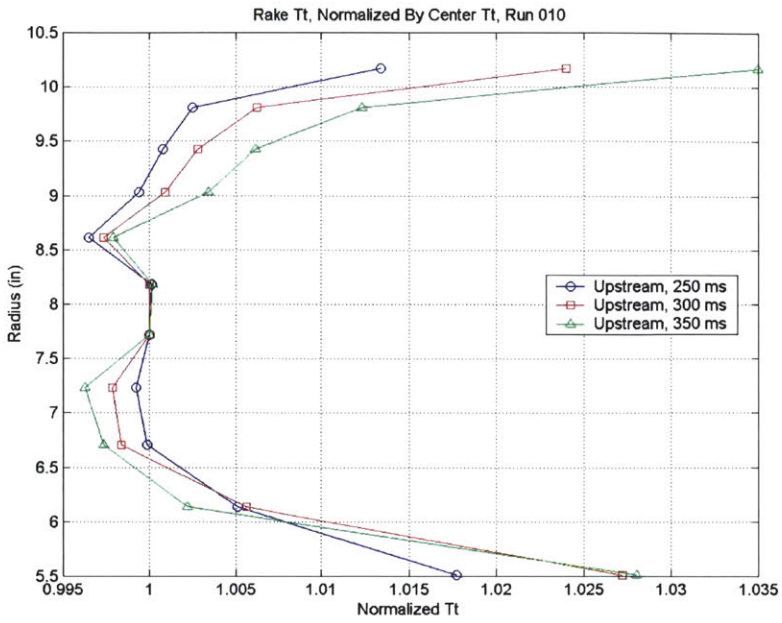

Figure 6.10: Thermal boundary layers during Run 010

6.3.2 Total Pressure Distortion

There are four circumferential points where the upstream total pressure is measured and there was as much as 4% variation among these measurements. After Run 011 pitot probes were added to increase the static pressure measurement density. Analysis showed that there is also a variation in the static pressure and velocity head entering the compressor. Figures 6.11 through 6.13 show the measured variation in these parameters for different runs. It is important to note that outside of the boundary layers there is no radial variation of total pressure measured by the rake.

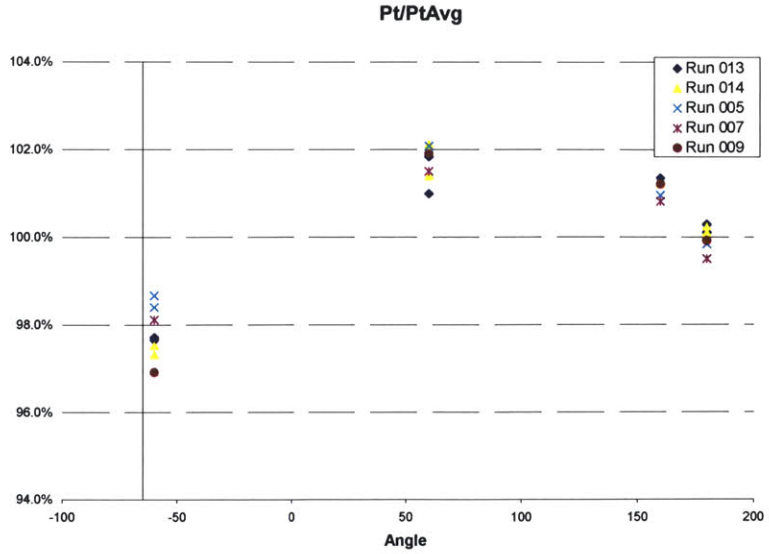

Figure 6.11: Circumferential total pressure variation, normalized by average total pressure

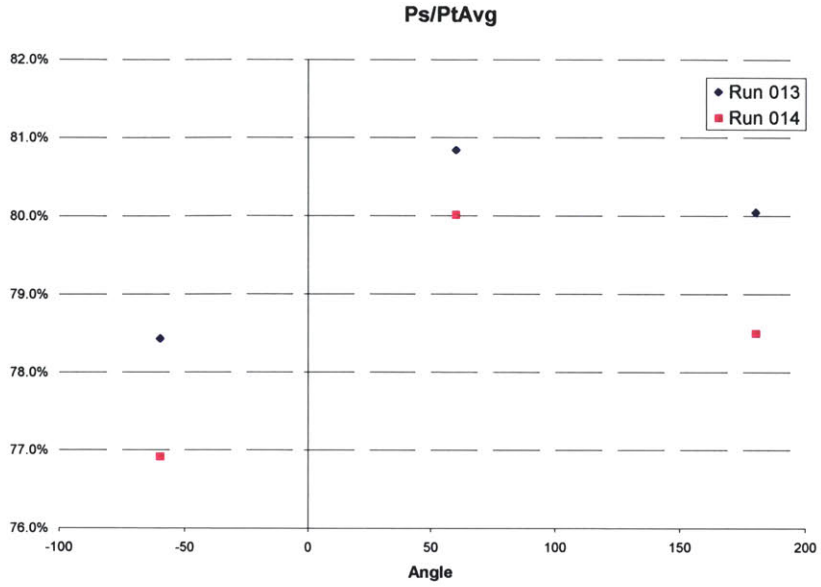

Figure 6.12 Circumferential static pressure variation, normalized by average total pressure

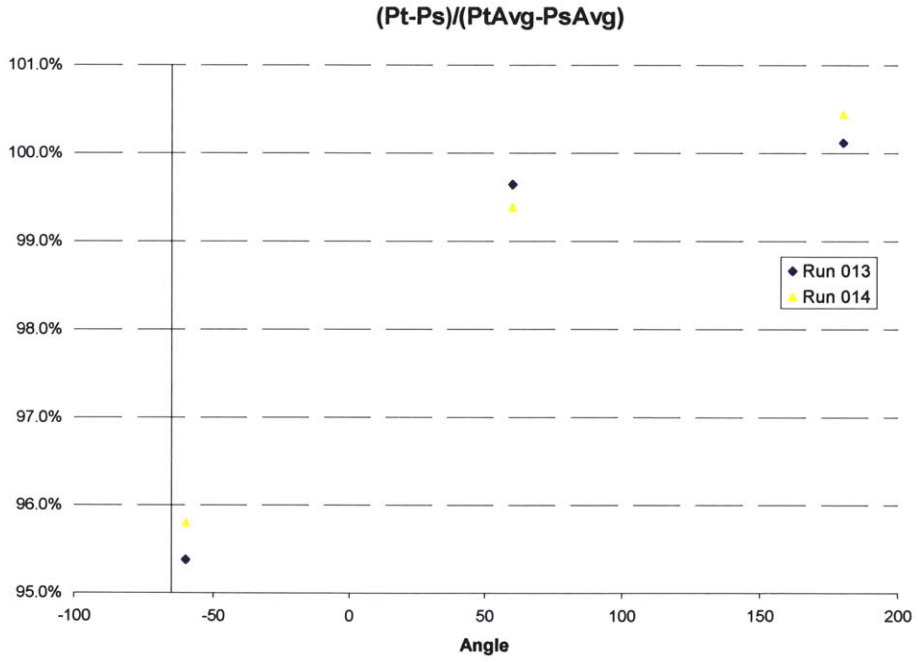

Figure 6.13: Circumferential variation in velocity head, normalized by the average

The measured variation is significant. N.A. Cumpsty defines a parameter for quantifying distortion (DC(60)) which is the change in total pressure divided by the average inlet velocity head. He says that typical engine contracts guarantee maintained operability for values of DC(60) ~ 0.5 [3]. For this facility DC(60) ~0.15. Establishing the source and extent of this distortion was a priority.

With only four circumferential measurements it was very difficult to make a statement about the extent of the distortion. It could have been 120° wide or possibly as small as a single jet. There are 60 hole diameters between the pressure screen and the measurement plane. This long length scale combined with the radial uniformity of the rake convinced the author that the jets were mixed out in the measurement plane. Figure 6.11 shows the consistency of the distortion for several runs. For these runs the rotor speeds, inlet Mach number, supply tank pressure, and throttle position all vary. The only consistent element from run to run was the pressure screen. Searching the literature for a model of losses through perforated plate the author found a paper by W.G. Cornell that presented a model for total pressure loss through a perforated plate with nearly sonic jets. This model says that the total pressure drop across the screen is linear with the percent open area of the screen. Cornell defines a loss factor by:

$$\lambda = \frac{P_{TUp} - P_{TDn}}{1/2 \cdot \rho_{Up} \cdot v_{Up}^2} \qquad \text{Eqn (6.6) [27]}$$

Table 6.1 shows the loss factor for several runs from the data. Figure 6.14 is Cornell's predicted loss factor based on Mach number entering the screen and percent closed area of the screen. These numbers seem to show that average loss across the screen roughly agrees with the model.

Table 6.2: Pressure Loss Coefficient for the screen

Run	Up Stream Mach #	Lambda
003	0.248	9.04
004	0.253	8.70
007	0.247	8.60
013	0.245	11.89
014	0.246	11.99

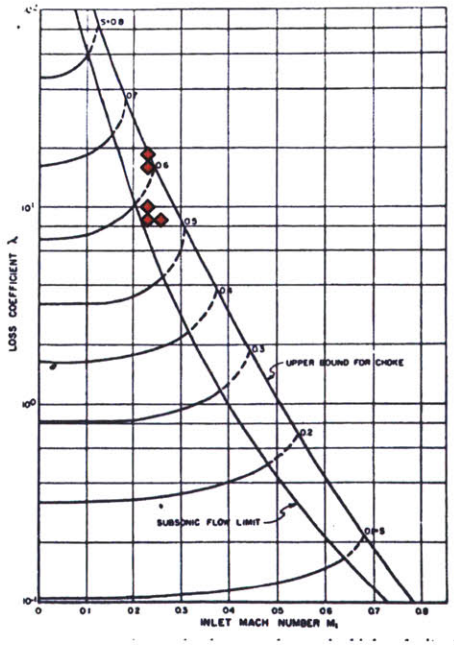

Figure 6.14: Prediction of loss coefficient [27]

The similarity between the model and the data suggests that the distortion is due to a variation in the open area of the screen. One simple approach, though not most accurate, to measure the open area was to count the number of holes. Eighteen 15° sectors with equal area were marked out on the screen and the number of holes in each sector were counted. In Figure 6.15 the measured circumferential variation in open area, along with error bars from the counting, is plotted on top of the previous plot of total pressure variation. There appears to be a strong correlation between total pressure variation and open area variation.

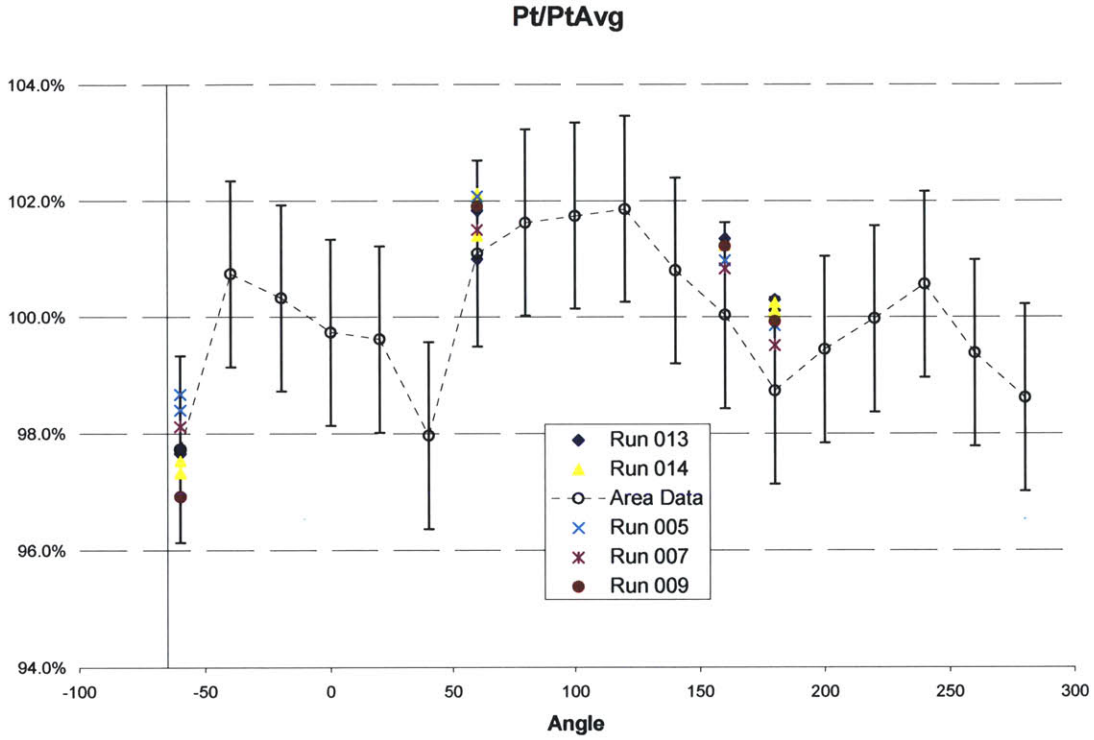

Figure 6.15: Correlation between area variation and total pressure

This data suggests that the total pressure variation is not a 4% distortion that extends 120° degrees but rather two 2% distortions. One is above the mean and extends for ~60° and another below the mean that extends for ~40°. Results shown in Section 6.5 seem to indicate that the compressor operates as designed in spite of the distortion.

6.4 Uncertainty Analysis

As important as the measured values of corrected flow, pressure ratio, and efficiency is the confidence that those numbers are the performance numbers of the machine. In this rig there are two sources of uncertainty. One source is the instrument measurement uncertainty and the other source is related to the flow properties and the discrete nature of the measurements. These sources are treated separately in the following sections.

6.4.1 Measurement Uncertainty

Uncertainty in the measurements of pressures and temperatures result in uncertainty in the final values for corrected flow and efficiency. Much of the work for determining uncertainty has already been performed by previous investigators. It should be noted that when calculating performance parameters the NIST gas tables for the mixture are relied upon. In order to make the uncertainty analysis a tractable problem it is necessary to assume that the working fluid is an ideal gas and that certain properties are constant. This yields analytical expressions for corrected flow and efficiency that can be manipulated to establish uncertainties. These analytical expressions and their derivations are found in Appendix B. Appendix C discusses the qualification procedure for the pressure transducers and contains Tables that list all the pressure transducers and the uncertainties associated with them. The uncertainties associated with the total pressure measurements are discussed in [5]. The results of his work are also tabulated in Appendix C.

Table 6.2 is the uncertainties in the corrected flow measurements due to measurement uncertainties. The Uncertainty Magnification Factors (UMF) show the relative weight of the uncertainty of each measurement [28]. These factors, and some of the measurement uncertainties, change from run to run because of variable flow conditions. It is interesting to note that because mass flow is corrected by inlet total temperature that term drops out of the analytical expression and the uncertainty in total temperature does not affect the corrected mass flow. Table 6.3 shows the uncertainty in the measured adiabatic efficiency. Efforts were made by Onnee to reduce the uncertainties in the total temperature measurement because the importance of total temperature uncertainty is 2.5X to 3X that of the total pressure uncertainty. For both sets of measurements the uncertainty could be reduced by creating a separate set of thermodynamic tables for the specific gas mixture ratio of each run.

Table 6.3: Uncertainties in Corrected Flow

		Rel. Measurement Uncertainties			UMF			
Run	Wc (% of Des)	Pt	Ps	λ	Pt	Ps	λ	Relative Uncertainty
005	81.7%	0.28%	0.29%	0.15%	2.940	-2.940	0.071	**1.17%**
006	81.4%	0.28%	0.28%	0.16%	2.973	-2.973	0.070	**1.18%**
007	80.0%	0.27%	0.28%	0.23%	3.138	-3.138	0.067	**1.23%**
008	83.0%	0.28%	0.29%	0.29%	2.788	-2.788	0.074	**1.13%**
009	91.9%	0.33%	0.32%	0.03%	1.935	-1.935	0.097	**0.88%**
010	92.3%	0.33%	0.32%	0.15%	1.894	-1.894	0.099	**0.86%**
011	87.9%	0.30%	0.30%	0.01%	2.285	-2.285	0.086	**0.97%**
013	98.0%	0.37%	0.34%	0.05%	1.467	-1.467	0.117	**0.74%**
014	100.5%	0.39%	0.35%	0.10%	1.302	-1.302	0.127	**0.69%**

Table 6.4: Uncertainties in adiabatic efficiency measurements

		Relative Uncertainty					UMF			
Run	Meas. Ad. Eff	Up Pt	Dn Pt	Up Tt	Dn Tt	γ	Pt	Tt	γ	Uncertainty
005	0.792	0.31%	0.42%	0.05%	0.10%	0.15%	1.347	-3.142	2.225	**0.85%**
006	0.811	0.31%	0.39%	0.05%	0.09%	0.16%	1.267	-2.952	2.280	**0.80%**
007	0.842	0.31%	0.36%	0.05%	0.09%	0.23%	1.182	-2.780	2.393	**0.84%**
008	0.840	0.32%	0.36%	0.05%	0.09%	0.29%	1.080	-2.446	2.375	**0.90%**
009	0.868	0.36%	0.37%	0.05%	0.09%	0.03%	0.959	-2.159	2.558	**0.54%**
010	0.873	0.36%	0.37%	0.05%	0.09%	0.15%	0.973	-2.205	2.552	**0.66%**
011	0.836	0.34%	0.37%	0.05%	0.09%	0.01%	0.935	-2.032	2.442	**0.51%**
013	0.888	0.40%	0.38%	0.05%	0.09%	0.05%	0.995	-2.297	2.598	**0.61%**
014	0.885	0.42%	0.38%	0.05%	0.09%	0.10%	1.033	-2.433	2.622	**0.69%**

6.4.2 Non-Instrument Related Uncertainties

There are other uncertainties that are not related to instruments but rather result from a lack of instrument density or fundamental aspects of the facility. The uncertainties that are considered are those related to discrete span-wise sampling of the flow, the discrete circumferential sampling of the inlet flow and the uncertainty that arises from the non-adiabatic performance of the compressor. Also discussed is accounting of the bleed flow in the reported adiabatic efficiency.

6.4.2.1 Uncertainty Related to Span-wise Sampling

The downstream temperature and pressure profiles are measured at discrete points and between measurement points the profile is assumed constant. To quantify the uncertainty that this process introduces to the measurement the author examined the difference between the area averaged efficiency from the CFD results when measured at the measurement points and when the entire CFD grid was used. Figure 6.16 shows this process for the CFD run where both rotors were at 90% of their corrected speeds. Table 6.4 lists the difference between the predicted area averaged core adiabatic efficiency and an area averaged adiabatic efficiency using just the values where there are instruments. The difference between the two values decreases towards the design point because as the pressure ratio profile is essentially flat (with exception of the end walls) thus the variation between points decreases. CFD data for this analysis was supplied by Dr. Merchant. It is important to remind the reader that values labeled as "measured" in this section are not measured data points but rather the CFD prediction at points where there are instruments.

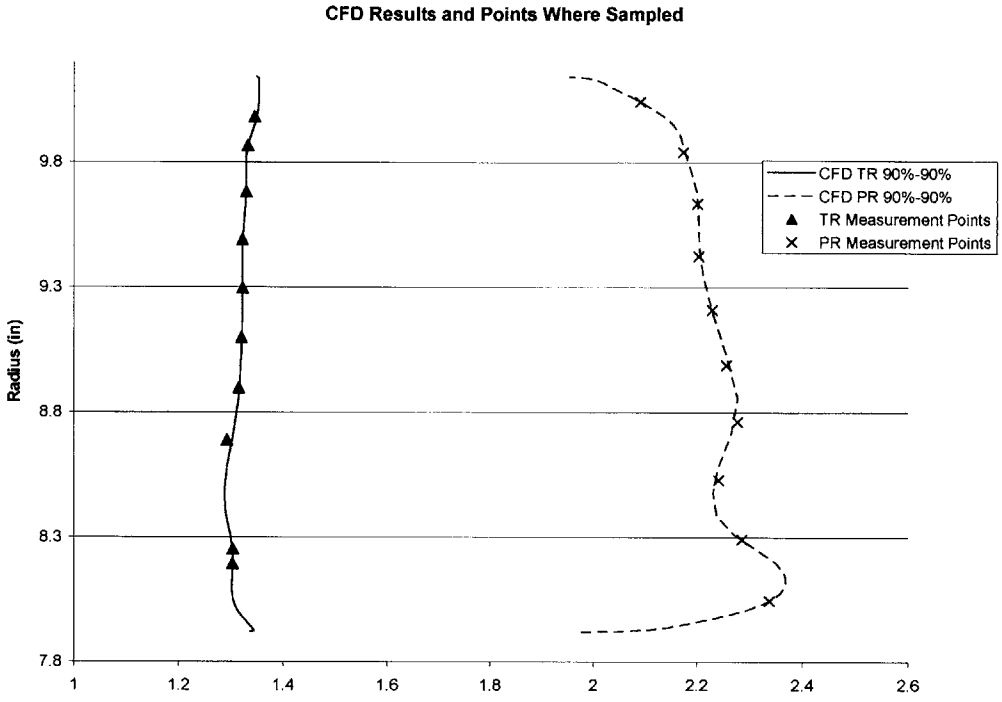

Figure 6.16: CFD result used to estimate uncertainty from radial sampling

Table 6.5: Uncertainty from discrete radial measurements

CFD Run	Predicted Eff	"Meas" Eff	Difference
90%-90%	80.70%	81.93%	1.24%
95%-95%	84.67%	85.41%	0.74%
100%-100%	87.33%	87.89%	0.56%

6.4.2.2 Uncertainty Resulting From Circumferential Sampling of Inlet Distortion

The total temperature and total pressure rakes sample the flow at one circumferential location. Because of this there is a difference between the measured upstream conditions and the true upstream conditions. When the efficiency analysis was done the total pressure rake values were not modified to reflect the average upstream total pressure because at the time the extent and shape of the inlet distortion was not fully known. This results in yet another uncertainty in the efficiency measurements. To quantify this uncertainty JF Onnee used the open area data to establish a baseline total pressure profile then used a parallel compressor analysis to compare the measured adiabatic efficiency to the adiabatic efficiency predicted by the parallel compressor model [5]. The result is that the inlet distortion results in an uncertainty in adiabatic efficiency on the order of 0.95%.

6.4.2.3 Uncertainty due to Non-Adiabatic Operation

Typically compressors operate adiabatically. In steady-state test rigs the temperatures of the compressor metal nearly match the temperatures of the working fluid and the heat transfer to the working fluid is negligible. In the blowdown test environment the temperature of the working fluid entering the compressor is as cold as 250° K. The ambient temperature of the facility is ~290° K. The mass of the compressors is large enough that they can be considered isothermal during the test time [5]. As the working fluid enters the compressor it is first heated by the metal, and then, due to compression heating, the temperature of the fluid rises above the metal temperature and heat is transferred from the fluid to the facility metal. J.F. Onnee estimated how the net heat transfer into the fluid would change the indicated efficiency relative to an adiabatic efficiency for the same compressor. This work is summarized in his master's thesis; the result is that the difference between the indicated efficiency and the adiabatic efficiency is ~0.01% [5].

6.4.2.4 Bleed Flow Accounting

As aspirated compressors have developed there has been discussion as to how to account for the mass flow when reporting efficiency [6]. J.L. Kerrebrock recommends that the efficiency of the machine should be expressed as the efficiency of core flow modified by the bleed flow as shown in Eqn. 6.6. (δ_i is the mass fraction of bleed flow i relative to the inlet mass flow, π_i and τ_i are the pressure ratio and temperature ratio of bleed flow i)

$$\eta_{overall} = \eta_{core}\left[1+\sum_i \delta_i\left(\pi_i^{\frac{\gamma-1}{\gamma}} - \tau_i\right)\right] \qquad \text{Eqn. (6.7)}$$

In this facility attempts were made to measure the bleed flow but they were unsuccessful. Equation 6.6 says that uncertainty in the bleed flow measurement does not affect the measurement of the core efficiency.

6.5 Initial Test Results

Fourteen tests have been run to date. The first seven tests were spent establishing how to operate the facility and moving up the 90%-90% speed line until the throttle position that matched the design throttle condition was found. Once the design throttle condition was found the rotor speeds were increased to the design speeds. For the first attempted test at design speed the second rotor over-sped to a corrected speed of 105% this test produced the highest pressure ratio. The data from these tests will be looked at and compared to CFD results. The CFD results are the analysis of John Adamczyk, using the APNASA code. Also, data from the high frequency wall static pressure measurements, located between and behind the rotors is analyzed.

6.5.1 90%-90% Corrected Speeds

Figure 6.17 shows the quasi-steady performance of the compressors during Run 007. The reported efficiency is the adiabatic core efficiency. This is an area averaged value from the rakes. Between 250 ms and 350 ms both the corrected speed for both rotors is 90% of the design value ±0.5%. During the test time the total pressure ratio varies from 2.34 2.26, a change of 3.4%. The adiabatic core efficiency varies from 87% to 82% during the test time. The corrected flow drops from 81% of the design value to 78% of the design value. It is expected that as the pressure ratio changes the corrected flow into the compressor would also change but typically a decrease in pressure ratio would lead to an increase in the corrected flow. During the test time the Reynolds' number entering the compressor varies 5%. The value used for normalizing Reynolds' number is the Reynolds' number used for designing and analyzing the rotors, ~8 x 10^5 based on chord.

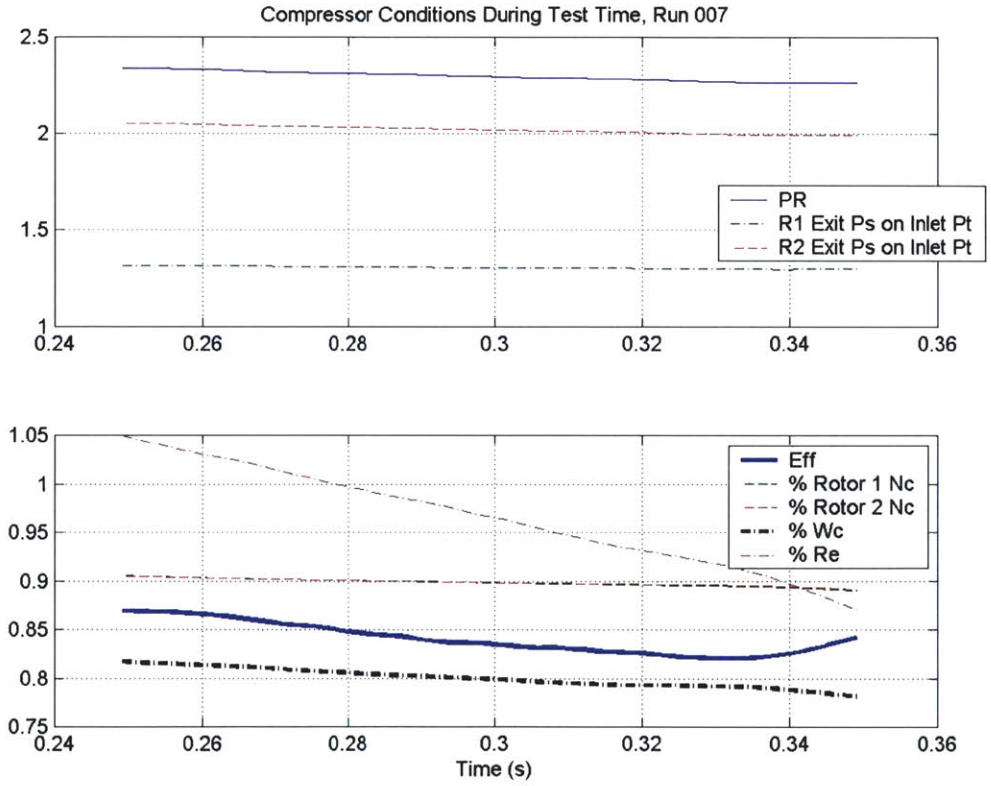

Figure 6.17: Performance Of CRAspC during Run 007

Figures 6.18-6.20 show comparisons of the measured span-wise pressure ratio, temperature ratio, and efficiency profiles of the compressor to the CFD predictions with the corrected speeds at 90%-90%. Below mid-span the measured total pressure ratio roughly agrees with the CFD. Above mid-span the total pressure ratio is as much as 4% higher than the predicted profile. The measured total temperature and efficiency profiles seem to agree well with the predicted profiles with the exception of the point nearest the tip casing.

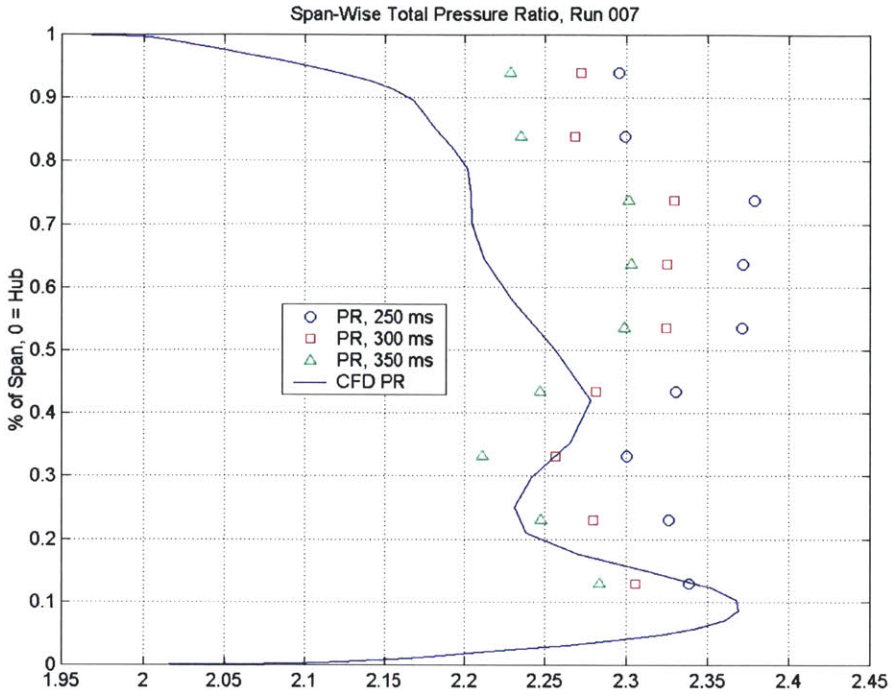

Figure 6.18: Span-wise Total Pressure Ratio Profile compared to CFD, 90%-90% Corrected Speeds

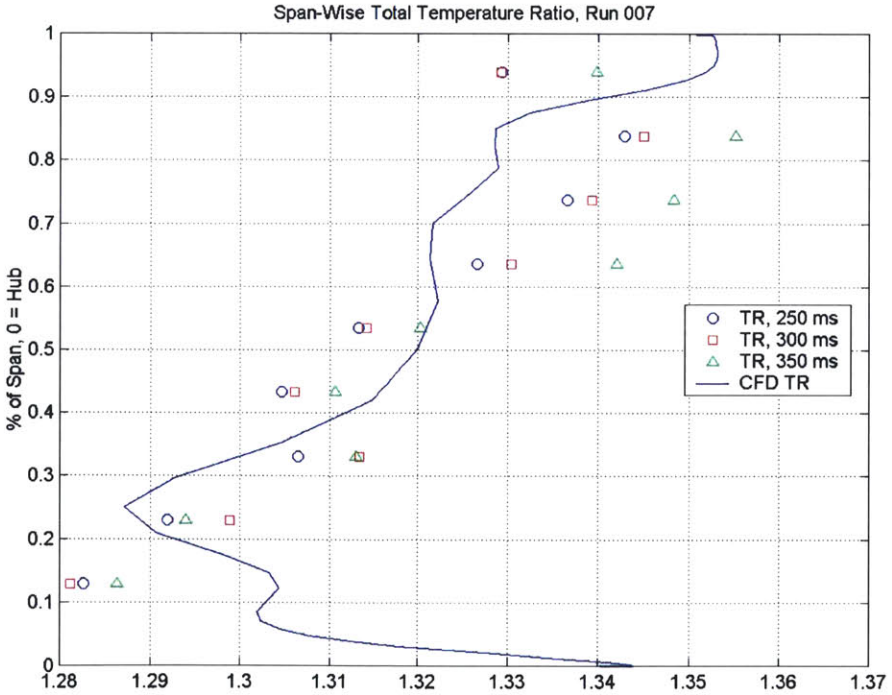

Figure 6.19: Span-wise Total Temperature Ratio Profile compared to CFD, 90%-90% Corrected Speeds

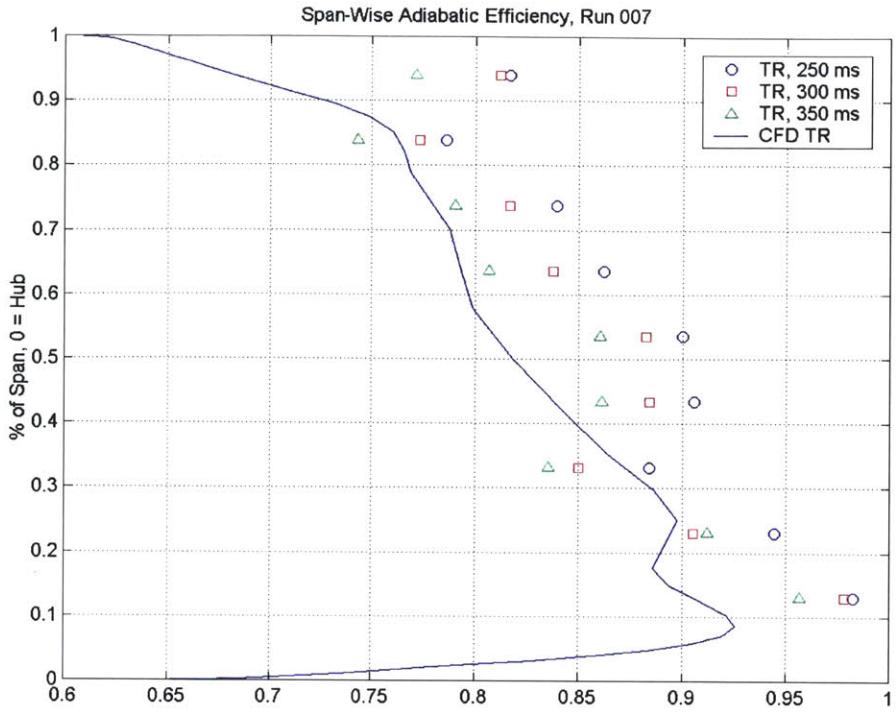

Figure 6.20: Span-wise Efficiency Profile compared to CFD, 90%-90% Corrected Speeds

6.5.2 100%-100% Corrected Speeds

Figure 6.21 shows the quasi-steady performance of the compressor at the design point. The corrected speeds start at 101% of their design values and at the end of the run they are at 100% of their design value. During the run the ratio of corrected speeds is constant. The corrected inlet flow drops 4% from 94% of the design corrected flow to 90% of the design corrected flow. During the test time the total pressure ratio across the compressor drops 1.7% from 2.95 to 2.90. The ratio of compressor exit static pressure to inlet total pressure is nearly constant during the run, dropping 1.9% from 2.58 to 2.53. The adiabatic efficiency of the core flow is 0.885 at the start of the test and drops as low as 0.865 near the end of the test time.

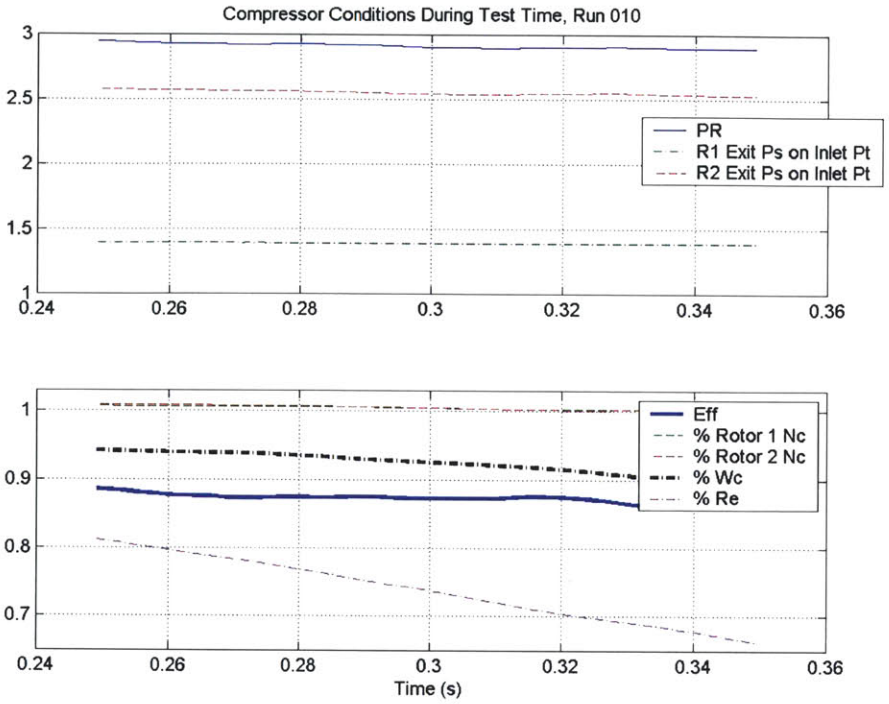

Figure 6.21: Compressor Performance at Design Point

Figures 6.22-6.24 show comparisons of the measured span-wise pressure ratio, temperature ratio, and efficiency profiles to the CFD predictions. It needs to be stated that the measured ratio of exit static pressure to inlet total pressure is lower for the test than for the CFD. The measured pressure ratio profile is lower than the predicted profile. Also of note is that in the CFD predicted pressure profile below 70% of the span the predicted pressure ratio increases slightly but the measured pressure ratio decreases slightly. The measured temperature ratio profile matches the predicted profile, with the exception of the hub and tip were it is lower. Similarly, the measured adiabatic efficiency profile generally matches the CFD efficiency profile except at the hub and tip. Similar to Run 007 the low tip total temperature ratio can be explained by the high inlet temperature; from the thermal boundary layer. The adiabatic efficiency near the hub approaches unity, in a region where one would expect end wall effects to lower the efficiency. The author believes that this is due to a combination of two factors. The reasons are fundamentally related to the fact that in when the profiles are generated there is an assumption that there is no radial mixing of the fluid in the compressor. Similar measurements for transonic, and supersonic compressors have shown that a combination of radial transport and vortex shedding move higher entropy fluid away from the hub to the center of the flow [29]. At this point these hypotheses are simply conjecture; there has been no modeling that demonstrates they are plausible explanations for the phenomena seen in this compressor.

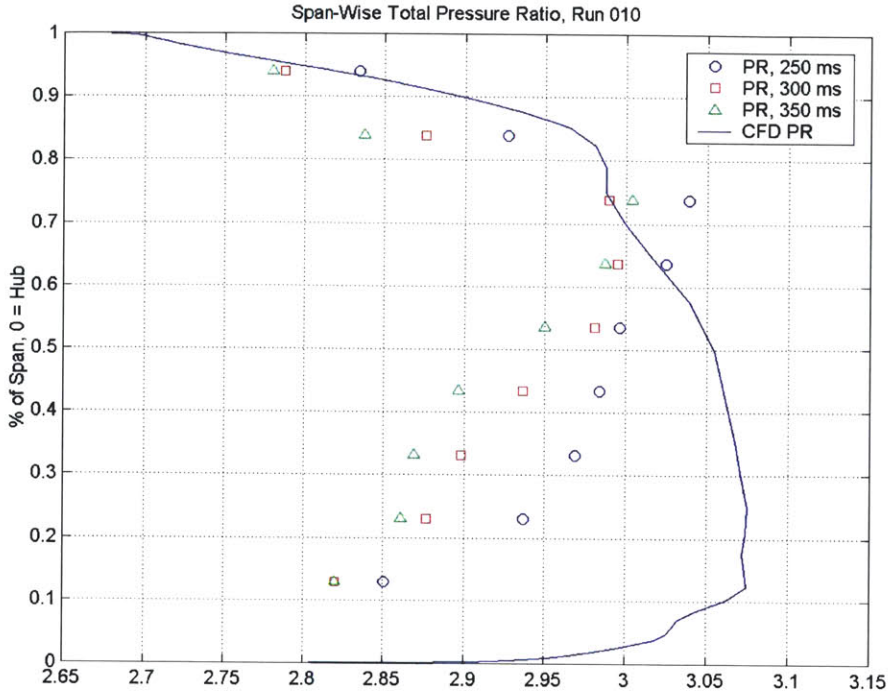

Figure 6.22: Span-wise Total Pressure Profile compared to CFD, Design Point

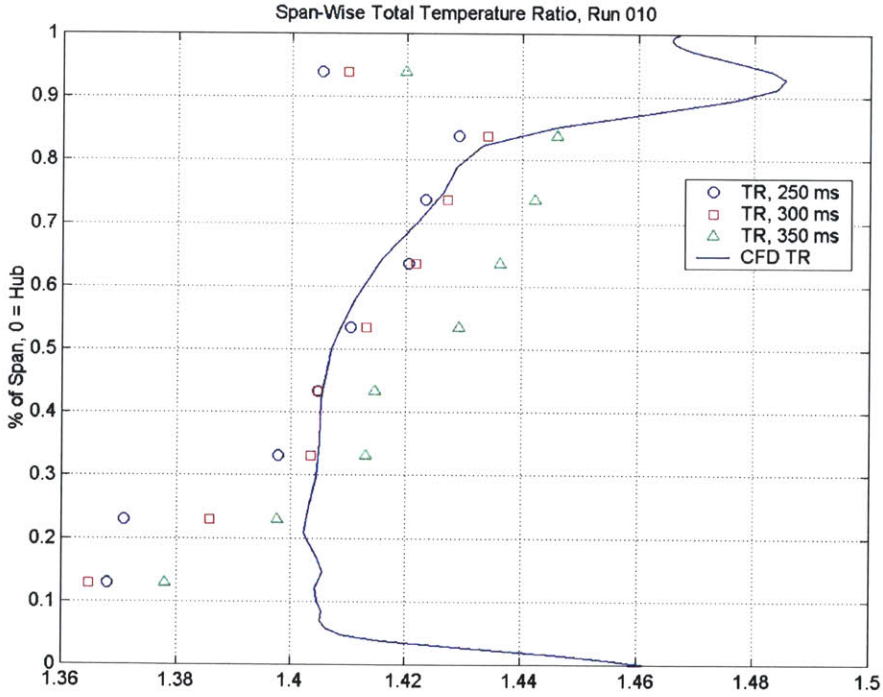

Figure 6.23: Span-wise Total Temperate Profile compared to CFD, Design Point

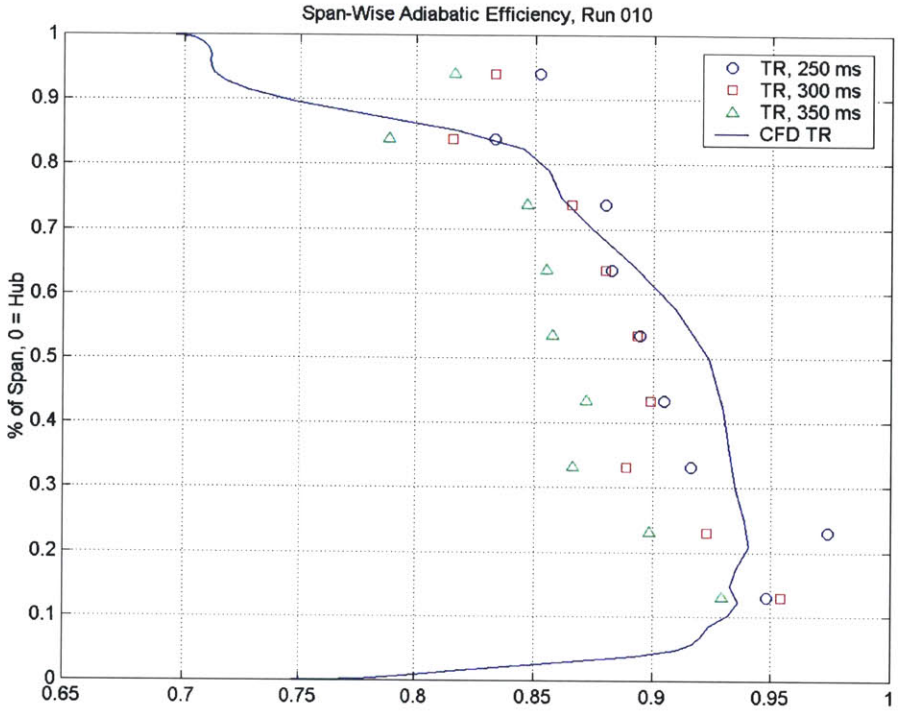

Figure 6.24: Span-wise Adiabatic Efficiency Profile compared to CFD, Design Point

6.5.3 100%-105% Corrected Speeds

Running Rotor One at 100% of its design corrected speed, Rotor Two at 105% of its design corrected speed , and the throttle at the design position (82.44 in^2) resulted in the highest pressure ratio seen during this series of tests. This occurred in Run 009 due to attempts to extrapolate initial conditions from corrected speeds of 90% to corrected speeds of 100%. Figure 6.25 shows the quasi-steady performance of the compressor at this condition. During the test time the total pressure ratio ranged from 3.03 to 2.90 and the adiabatic core efficiency started at 0.887 and dropped to 0.838.

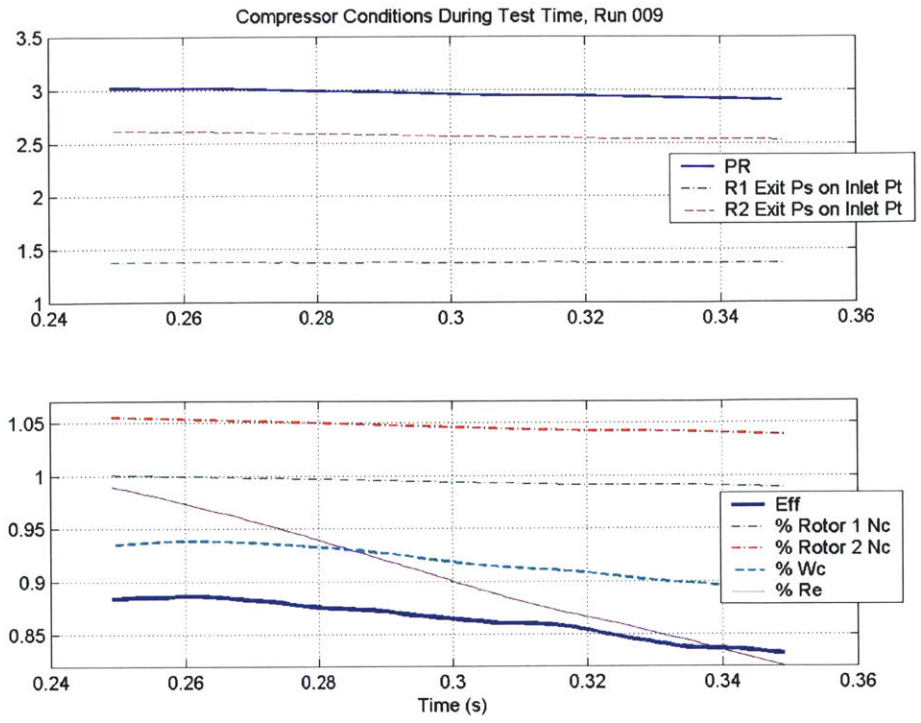

Figure 6.25: Compressor Performance for Run 009

6.5.4 Summary of Performance Results

Table 6.5 lists the results of the CFD and the measured values for two operating points. At the design point the total pressure ratio is 4% lower than the predicted CFD value and the exit static pressure to inlet total pressure ratio is 3% lower than predicted. As can be seen on the map (Figure 6.26) decreasing the throttle area did not increase the pressure ratio. For both cases the measured corrected flow was lower than the CFD prediction. At the 90%-90% run the corrected flow was 2% lower than predicted and at the design point the corrected flow was 6% lower than predicted.

Table 6.6: Comparison of performance parameters for two operating points

	CFD Results [16]				Measured Values					
Corrected Speeds	**PsonPt***	**PR**	**Eff**	**Wc****	**PsonPt**	**PR**	**Eff**	**Wc**	**R1 Nc*****	**R2 Nc**
90%-90%	1.899	2.226	0.810	33.43	2.044	2.329	0.863	34.09	90.4%	90.3%
100%-100%	2.650	3.066	0.884	41.97	2.572	2.934	0.879	39.45	100.7%	100.9%

* PsonPt is the exit static pressure to inlet total pressure ratio

** Wc is the Corrected Flow (lbm/sec/ft^2)

*** Nc is the Corrected Speed as a percent of the design corrected speed

Figure 6.26 is the current compressor map. The values for these points come from an average of the quasi-steady time data during the first three revolutions of Rotor Two after the initial blowdown transient. During three revolutions of rotor two the corrected speeds

are constant to within 0.3% and the inlet correct flow is constant to within 1%. Also, if the axial velocity is assumed constant then the typical through flow time from the upstream instrument window to the downstream instrument window is ~ 0.4 revolutions of Rotor Two. Comparing the predicted CFD line of constant corrected speed, at the design speed, to the measured 100% corrected speed line one can see that the compressor is producing a total pressure ratio 7% lower than predicted. The points on Figure 6.26 with arrows all had the same throttle setting. For the measured 100% corrected speed line the throttle area was changed by 5% from the nominal setting, first more closed, and then more open. At some point the 100% speed line should become vertical. It appears that opening the throttle another 5% will find this vertical section of the speed line. In Figure 6.27 the area-averaged adiabatic core efficiency is plotted vs. corrected flow for each point; along with the CFD predictions. The efficiency of the compressor appears to be better than predicted. Figure 6.28 shows the polytropic core efficiency vs. corrected flow. Error-bars on Figures 6.26-28 indicate the estimated uncertainty for each measurement.

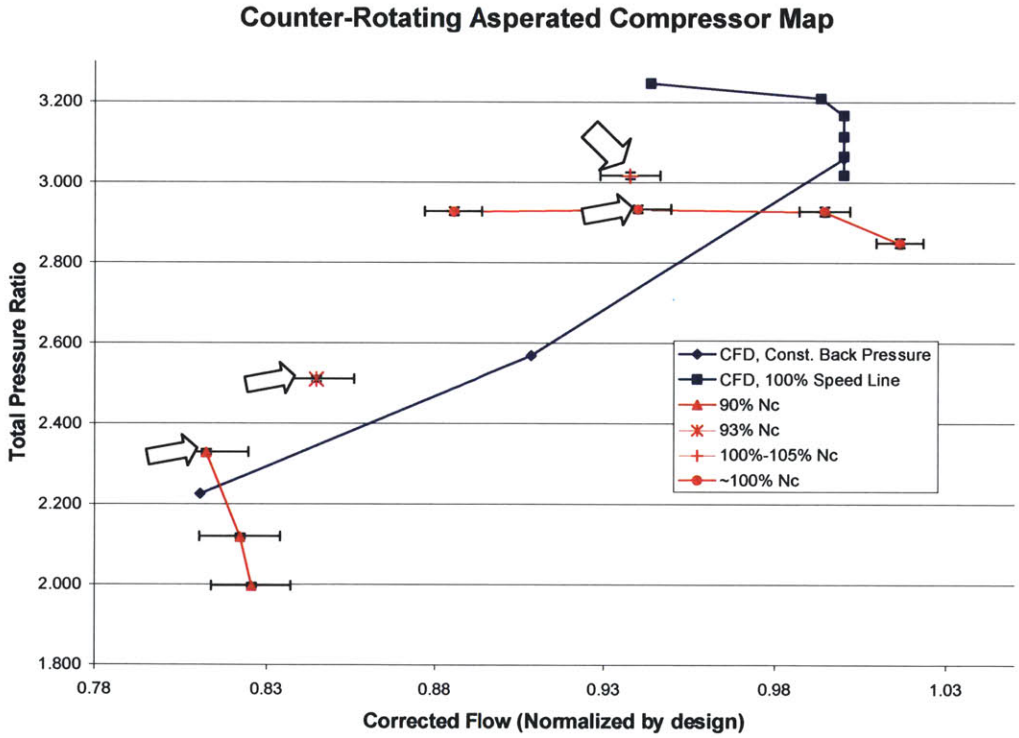

Figure 6.26: Compressor Map, Pressure Ratio vs. Corrected Flow

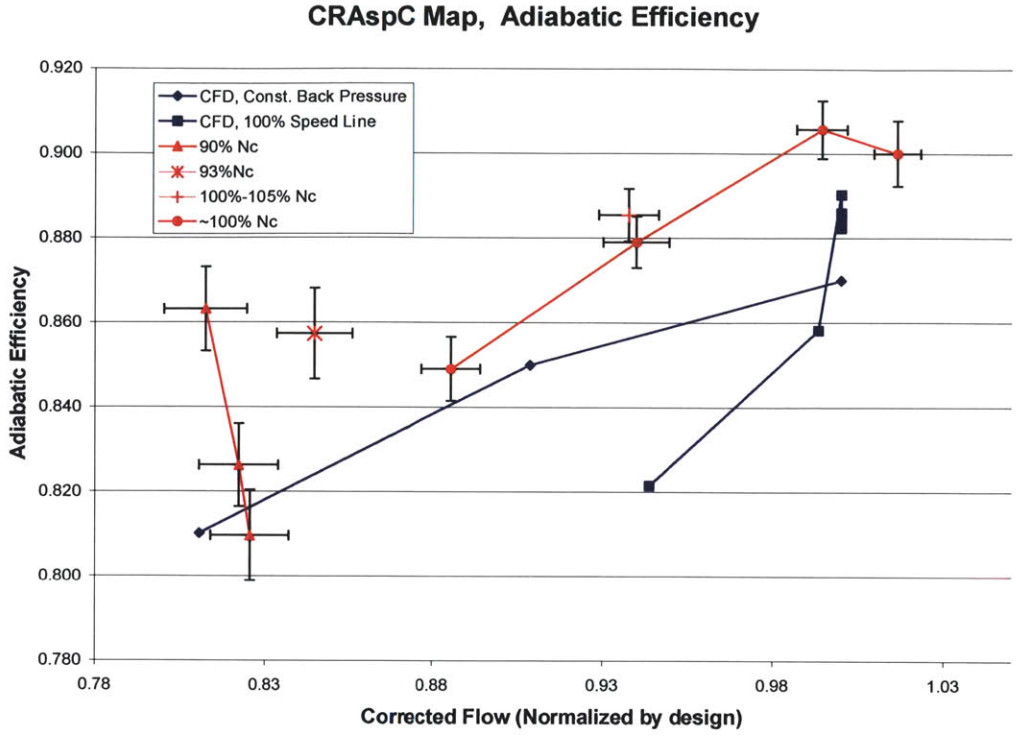

Figure 6.27: Compressor Map, Adiabatic Efficiency vs. Corrected Flow

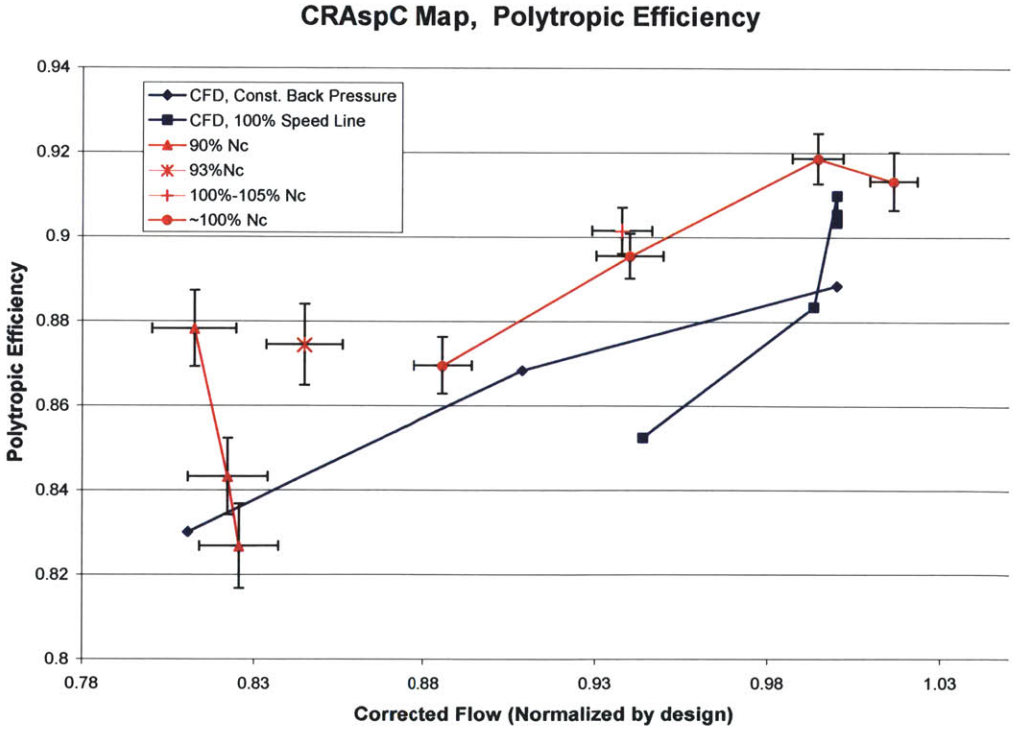

Figure 6.28: Compressor Map, Polytropic Efficiency vs. Corrected Flow

6.5.5 Change in Operating Point during the Test Time

For each run the values that define the operating point of the compressor change from 250 ms to 350 ms. These metrics are the corrected flow entering the compressor, the corrected speeds of the two rotors, the angle of the flow relative to the compressor (this is the angle of a vector made from the inlet velocity and the mid-span wheel speed of Rotor One, shown in Figure 4.1), Reynolds' Number (based on Rotor One chord), and the ratio of the exit static pressure to the inlet total pressure. Table 6.7 lists each of these parameters, how they change, and the average value for each run. A negative 'drop' in Table 6.7 indicates an increase. Corrected flow and corrected speeds are listed as percentages of the design values. The measurement of the exit static pressure to inlet total pressure ratio comes from the high frequency casing static tap. The changes in corrected speeds and Reynolds' agree with the predictions of the lumped parameter model used during the facility design. It was expected that while the pressure ratio across the throttle indicated it was choked, based on 1-D compressible flow theory, the corrected flow across the throttle and into the compressor would remain constant. The change in back pressure ratio seems to indicate that the corrected flow through the throttle is changing and further verify that the 1-D compressible flow model does not hold. A fundamental question that needs to be answered is 'what is the primary source for the changing inlet corrected flow?' If the change in corrected flow is related to something in the facility (i.e. the throttle or the screen) then the data can be treated in a manner where the compressor is considered to be operating in a quasi-steady state through several different operating points. If the source of the change in corrected flow is the compressor then fundamental questions about the compressor must be answered.

Table 6.7: Change in operating conditions during test time

	Wc		Nc Rotor One		Nc Rotor Two		Reynolds' Number		Relative Angle		Back Pressure	
Run	% Drop	Avg.	% Drop	Avg.	% Drop	Avg.	% Drop	Avg.	% Drop	Avg.	% Drop	Avg.
005	2.4%	81.6%	1.2%	89.8%	-0.1%	88.7%	15.4%	8.79E+05	-0.6%	63.6	1.4%	1.69
006	2.3%	81.3%	1.2%	89.6%	0.4%	88.9%	15.4%	8.72E+05	-0.6%	63.7	1.8%	1.82
007	3.6%	79.8%	1.3%	89.8%	1.2%	89.8%	15.3%	8.90E+05	-1.1%	64.2	2.1%	2.02
008	4.0%	82.9%	2.0%	92.9%	2.1%	92.5%	14.3%	9.94E+05	-1.1%	64.0	3.4%	2.17
009	4.9%	91.8%	1.0%	99.4%	1.4%	104.6%	16.9%	8.39E+05	-2.1%	62.5	2.9%	2.57
010	3.8%	92.5%	0.4%	100.5%	0.7%	100.6%	14.9%	6.92E+05	-1.8%	62.4	1.1%	2.55
011	1.9%	87.9%	0.5%	100.4%	0.8%	100.5%	12.7%	6.77E+05	-0.7%	64.0	1.6%	2.55
013	2.8%	98.2%	0.2%	101.5%	0.3%	101.5%	13.6%	7.41E+05	-1.6%	60.6	0.7%	2.53
014	3.0%	100.3%	0.1%	101.7%	0.2%	102.1%	17.0%	7.39E+05	-1.9%	59.9	0.8%	2.45

6.5.5.1 Drop in Efficiency during Test Time

In each test the adiabatic efficiency of the compressor changed during the test time. The drop in adiabatic efficiency was as small as 0.015 and as much as 0.040. For the runs near the design point at 250 ms the compressor was 'good' (based on efficiency) and 'bad' at 350 ms. Thus it is important establish why the efficiency is changing.

An attempt has been made to correlate the change in adiabatic efficiency during test time and the change in inlet Reynolds' number. The inlet Reynolds' number, based on Rotor One chord, varied from run to run and the minimum inlet Reynolds' number for all the runs was ~6 x 10^5. According to Cumpsty a change in adiabatic efficiency can be correlated to a change in Reynolds number by the relationship:

$$(1-\eta) = k \cdot R_e^{-n} \qquad \text{Eqn 6.8 [3]}$$

This relationship has been found to describe hydrodynamically smooth blades with a lower loading coefficient than this compressor. According to Cumpsty up to a Reynolds' number of ~5 x 10^5 n is in the range of 0.10 to 0.13. Above a Reynolds' number of 5 x 10^5 changes in Reynolds' number do not effect the losses of the compressor. Equation 6.6 was manipulated so that k and n could be found by fitting the data, in a least squares manner, for runs 007, 009, and 010. After fitting the model to the data for those runs there is no consistency in the coefficients k and n.. The values for k range from 150 to 1.9 x 10^{12} and the values for n range from 0.53 to 2.24. The values for n are not close to those reported by Cumpsty. This combined with the fact that the Reynolds' number, based on chord, is above the value for which Cumpsty reports that changes in Reynolds' number produce a change in efficiency lead the author to think that the Reynolds' number is not the primary cause for changes in efficiency.

6.5.6 High Frequency Data Analysis

The primary purpose of the two high frequency wall static pressure taps is to assess if the compressors are operating with a rotating stall. The data from these taps was checked after each run and the compressors did not stall during the test time (250 ms to 350 ms). Further analysis of this data demonstrates interesting properties of the compressors, although there is not enough data to make quantitative statements about the phenomenon witnessed. Figure 6.29 shows the exit static pressure to inlet total pressure ratio of the first rotor for 3 revolutions during the test time and the Discrete Fourier Transform of that data. The abscissa of the bottom plot is frequency normalized by the speed of the first rotor. On this scale the frequency of Rotor One is 1 and the Rotor One blade passing frequency is 20. The blade passing frequency of the second rotor is 23. The shock waves that travel upstream from each Rotor Two blade (the peak at 23) have a greater influence in the static pressure measurement than the wakes from Rotor One (the peak at 20). Early in the analysis there were questions about the source of the response peak seen near 3. Kerrebrock suggested that the response could be due to combination tones of the shock waves in Rotor Two; a result of manufacturing variations of the Rotor Two blades. To do ensemble average the time based signal is interpolated so that for each revolution there are N points. For the number of revolutions during the test time (~ 16) the interpolated signal at each of these angular points is averaged. This procedure removes elements of the signal that is not tied to the rotor. Figure 6.30 is the ratio of Rotor One exit static pressure to inlet total pressure ratio ensemble-averaged using the rotor two once-per-revolution signal and its Discrete Fourier Transform. The peak at 3 in Figure 6.30 indicates that the lower frequency peak in Figure 6.29 is tied to Rotor Two.

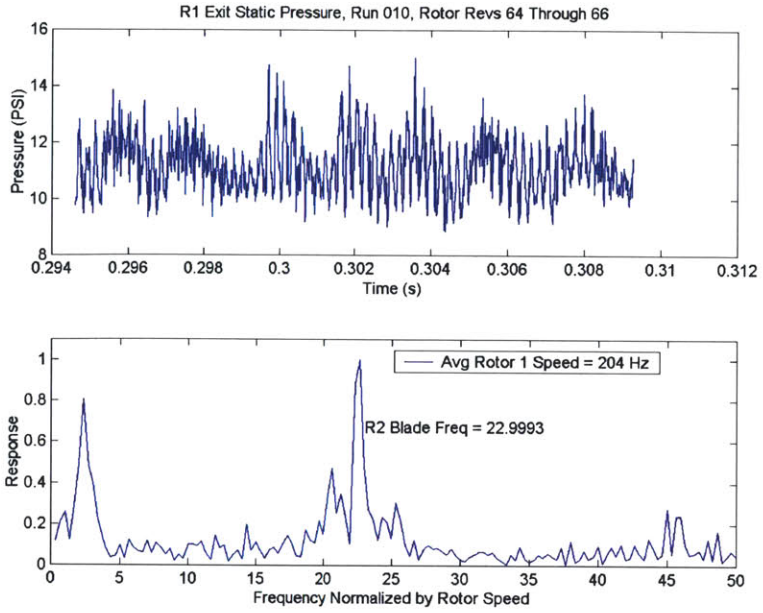

Figure 6.29: High-Frequency wall static pressure measurement between rotors, Run 010

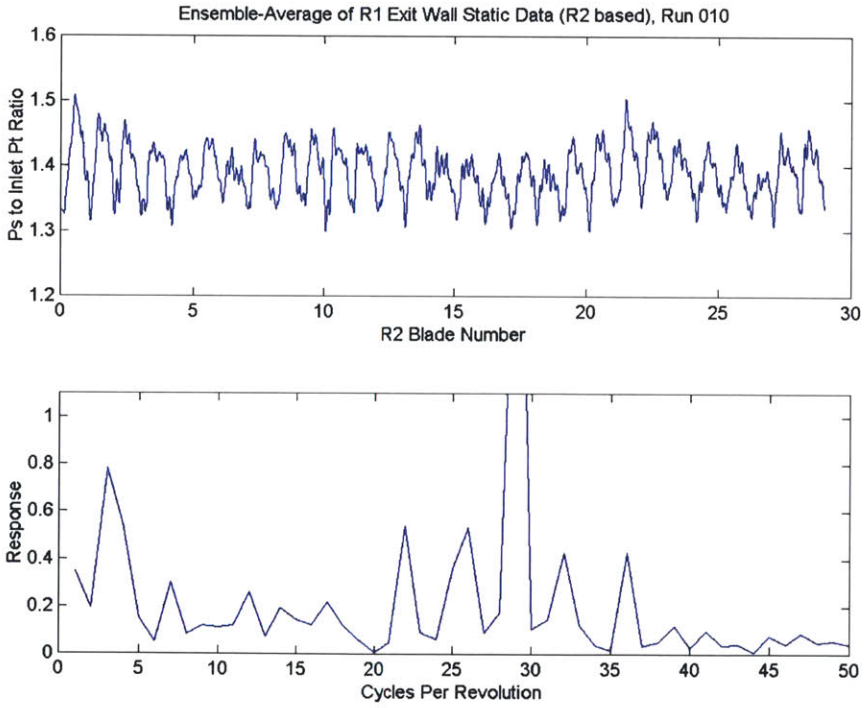

Figure 6.30: High-Frequency wall static pressure, ensemble averaged, Run 010

7 Conclusions and Future Recommendations

7.1 Results

The Counter-Rotating Aspirated Blowdown Compressor Test Facility succeeded in measuring the adiabatic core efficiency of a counter-rotating fan with an uncertainty of ~0.8% by measuring the total temperatures and pressures. The available test time was shorter than desired (~100 ms compared to ~400 ms) because of the drop in supply tank gas temperature but it still exceeded the test time of previous blowdown compressor experiments. Three points were measured on the 90%-90% corrected speed line of the compressor along with 4 points on the 100%-100% corrected speed line. In spite of intentions the compressor was shown to operate with inlet distortions in temperature and pressure. Given the distortion there appeared to be similarities between the CFD and measured performance of the compressor. The measured pressure ratio was ~7% low at the design speed and the adiabatic core efficiency was 1-2% better than predicted.

7.2 Recommendations

The author feels that there is still much that could be learned from this facility. First, it might be of value to industry to finish mapping the compressor. There needs to be more investigation into how varying the corrected speed ratio changes the behavior of the compressor. The compressor has not yet been throttled to stall during the test time so of interest is the corrected flow margin between the design point and the stall point and the stall characteristics of counter-rotating compressor.

7.2.1 Further Analysis

Some of the above questions can be answered through further analysis of the current data. The compressor has entered rotating stall during every run. The high-frequency casing static pressure data during this time could be investigated to learn something about the frequencies of the rotating stall. There is only one circumferential location for this data so there is no information about the number of stall cells. Also caution must be used because typically when the compressor stalls the inlet temperature is so cold that one cannot be certain about the properties of the flow entering the compressor.

The author also feels that improvements need to be made to the lumped parameter model that was used when designing the facility. Improvements would include changing how the compressor is modeled to match what has been observed in tests thus far. This model should also include some estimate of what is occurring in the bleed passage. An improved model has the potential of shedding light on the question of what is causing the change in corrected flow.

7.2.2 Further Measurements

Before another test is run it would be good to replace the pressure screen. This should decrease the inlet distortion. Based on the available data a perforated plate with an open area of 40% provides an adequate loss in total pressure across the screen. In order for the total pressure entering the compressor to be constant to within ±0.5% the open area of the pressure screen must be constant to ±0.5%. In addition to replacing the pressure screen improvements should be made to the bleed flow passage to give a better measurement of the bleed flow. One idea is that an annular sleeve could be inserted into the current bleed flow passage to reduce its volume. This should improve the likelihood of measuring the bleed flow.

In addition to those facility modifications the author would like to see the number of high-frequency pressure measurements increased. High-frequency 4-way pressure probes should be placed behind each rotor [29]. Hopefully the adjustments to the bleed flow passage and the addition of a 4-way probe would allow investigators to find a correlation between the amount of bleed flow and the width of the wake exiting Rotor Two.

Finally, according to the CFD, the aspiration slots set the position of the shock in Rotor Two. Placing several high frequency transducers in an axial pattern above the second rotor would allow for verification of this flow feature. Also adding high frequency wall statics would give insight into rotating stall characteristics.

Works Cited

[1] A.J. Wennestrom, 1990, *Highly Loaded Axial Flow Compressors: History and Current Developments*, Journal of Turbomachinery, Oct 1990, Vol. 112

[2] J.L. Kerrebrock, 2001, *Aircraft Engines and the Gas Turbine;* © Massachusetts Institute of Technology, Cambridge, MA

[3] N.A. Cumpsty, 1989, *Compressor Aerodynamics,* © Longman Scientific & Technical, London U.K.

[4] Dr. Aspi Wadia, Personal Communication

[5] J.F. Onnee, 2005, *Aerodynamic Performance Measurements in a Counter-Rotating Aspirated Compressor;* Masters Thesis, Massachusetts Institute of Technology

[6] J.L. Kerrebrock. *The Prospects for Aspirated Compressors*. MIT – AIAA-2000-2472. 2000

[7] M.A. Saad, 1993, *Compressible Fluid Flow, Second Edition;* © Prentice-Hall Inc, Upper Saddle River, NJ

[8] J.L. Kerrebrock, May 1972, *The M.I.T Blowdown Compressor Facility;* GTL Report No. 108

[9] G.R. Guenette, Jr., 1985, *A Fully Scaled Short Duration Turbine Experiment;* ScD Thesis, Massachusetts Institute of Technology

[10] M. Glynn, Work done under contract October 2003 through January 2004

[11] W.D. Baines & E.G. Peterson, 1951, *An Investigation of Flow through Screens;* Transactions of the ASME

[12] I.E. Idel'chik, 1996, *Handbook of Hydraulic Resistance, Third Edition;* © Begell House Inc., New York, NY

[13] W.C. Young & R.G. Budymas, 2002, *Roark's Formulas for Stress and Strain, Seventh Edition;* © McGraw-Hill, New York, NY

[14] S.S. Rao, 1995, *Mechanical Vibrations 3rd Edition;* © Addison-Wesley Publishing Company, Reading, MA

[15] Personal communication with representatives of Mi-Tech Metals; July, 2004

[16] Ali Merchant, Personal Communication

[17] John Adamczyk, APNASA Solutions

[18] Fritz Neumayer, Personal Communication

[19] M. Glynn, Work done under contract June 2004

[20] May 9, 2005, *TWI Knowledge Summary: Electron-Beam Welding Equipment;* © The Welding Institute, http://www.twi.co.uk/j32k/protected/band_3/ksas001.html

[21] Ultraminiature IS Pressure Transducer, XCQ-062 Series Spec. Sheet; www.kulite.com

[22] National Instruments Product Information, www.ni.com

[23] E. Ower & R.C. Pankhurst, 1977, *The Measurement of Airflow, Fifth Edition;* © Pergamon Press Inc., Elmsford, NY

[24] United Sensor Corporation, www.unitedsensorcorp.com

[25] L.N. Cattafesta, 1988, *An Experimental Investigation of the Effects of Inlet Radial Temperature Profiles on the Aerodynamic Performance of a Transonic Turbine Stage,* Master's Thesis, © Massachusetts Institute Technology

[26] NIST Mixture Property Database Ver. 9.08, 1992, © US Department of Commerce, National Institute of Standards and Technology; Boulder, CO

[27] W.G. Cornell, 1958, *Losses in Flow Normal to Plane Screens;* Transactions of the ASME, May 1958

[28] HW Coleman & WG Steele, 1999, *Experimentation and Uncertainty Analysis for Engineers 2nd Edition,* Wiley-Interscience, New York, NY

[29] B.J. Schuler, 2001, *Experimental Investigation of an Aspirated Fan Stage,* Doctoral Thesis, © Massachusetts Institute Technology

Appendix A: Blowdown Equations

This derivation was first done by Kerrebrock and later expanded by Guenette. We assume an isentropic expansion through the valve, that the flow through the pressure screen is choked, that the supply tank acts as a stagnation plenum, and that properties inside the tank are uniform.

Start with conservation of mass

$$V_S \cdot \left(\frac{d}{dt} \rho_S(t) \right) = \text{mdot}$$

Noting that mass flow out of supply tank equals mass flow through choked screen

$$V_S \cdot \left(\frac{d}{dt} \rho_S(t) \right) = W_{Sc} \cdot \frac{A_{Sc} P_S(t)}{\sqrt{Rg \cdot T_S(t)}}$$

$$V_S \cdot \left(\frac{d}{dt} \rho_S(t) \right) = W_{Sc} \cdot A_{Sc} \rho_S(t) \cdot \sqrt{Rg \cdot T_S(t)}$$

For an Isentropic process:

$$\theta(t) = \frac{\rho(t)}{\rho(0)} = \left(\frac{T(t)}{T(0)} \right)^{\frac{1}{\gamma - 1}} = \left(\frac{P(t)}{P(0)} \right)^{\frac{1}{\gamma}}$$

$$V_S \cdot \rho_S(0) \cdot \left(\frac{d}{dt} \theta(t) \right) = W_{Sc} \cdot A_{Sc} \cdot \rho_S(0) \cdot \sqrt{Rg \cdot T_S(0)} \cdot \theta(t)^{\frac{\gamma+1}{2}}$$

$$\theta(t)^{\frac{-(\gamma+1)}{2}} \cdot \left(\frac{d}{dt} \theta(t) \right) = \frac{W_{Sc} \cdot A_{Sc}}{V_S} \cdot \sqrt{Rg \cdot T_S(0)}$$

Integrate over time:

$$\int_{t=0}^{t=t} \theta(t)^{\frac{-(\gamma+1)}{2}} \cdot \left(\frac{d}{dt} \theta(t) \right) dt = \int_{t=0}^{t=t} \frac{W_{Sc} \cdot A_{Sc}}{V_S} \cdot \sqrt{Rg \cdot T_S(0)}\, dt \qquad \theta(0) = 1$$

$$\frac{2}{1-\gamma} \theta(t)^{\frac{(1-\gamma)}{2}} - \frac{2}{1-\gamma} = \frac{W_{Sc} \cdot A_{Sc}}{V_S} \cdot \sqrt{Rg \cdot T_S(0)}\, t$$

$$\theta(t) = \left(1 + \frac{t}{\tau_b} \right)^{\frac{-2}{\gamma-1}} \qquad \tau_b = \left[\frac{(\gamma - 1) W_{Sc} \cdot A_{Sc}}{2 \cdot V_S} \cdot \sqrt{Rg \cdot T_S(0)} \right]^{-1}$$

Appendix B: Uncertainty Analysis Derivations

Uncertainty Propagation In Corrected Flow Measurement

The through the temperature and pressure range of flow into the compressor the gas mixture used in the facility does not follow the ideal gas law. During the test time the relationship between temperature, pressure, and density vary from the ideal gas law as much as 2%. In order to derive analytical expressions for the impact of measurement uncertainties on the uncertainty of the corrected flow the gas mixture will be assumed to follow the ideal gas law with constant thermodynamic properties such as γ.

The Corrected Flow is:

$$Wc = \frac{\dot{m} \cdot \sqrt{\frac{R_g \cdot T_t}{R_{Air} \cdot T_{t\,Ref}}}}{A_c \cdot \frac{P_t}{P_{t\,Ref}}}$$

$$\dot{m} = f(\gamma, M) \frac{A_C \cdot P_T}{\sqrt{R_g \cdot T_T}}$$

$$f(\gamma, M) = \frac{\sqrt{\gamma} \cdot M}{\left(1 + \frac{\gamma - 1}{2} M^2\right)^{\frac{\gamma+1}{2\cdot(\gamma-1)}}}$$

$$M = \sqrt{\frac{2}{\gamma - 1}\left(\left(\frac{P_t}{P_s}\right)^{\frac{\gamma-1}{\gamma}} - 1\right)}$$

combining these:

$$Wc = \frac{P_{t\,Ref}}{\sqrt{R_{Air} \cdot T_{t\,Ref}}} \frac{\sqrt{\gamma} \cdot M}{\left(1 + \frac{\gamma - 1}{2} M^2\right)^{\frac{\gamma+1}{2\cdot(\gamma-1)}}}$$

The relative uncertainty in the Corrected Flow measurement is:

$$\left(\frac{U_{Wc}}{Wc}\right)^2 = \left(\frac{M}{Wc}\frac{\partial Wc}{\partial M}\right)^2 \cdot \left(\frac{U_M}{M}\right)^2 + \left(\frac{\gamma}{Wc}\frac{\partial Wc}{\partial \gamma}\right)^2 \cdot \left(\frac{U_\gamma}{\gamma}\right)^2$$

$$\frac{M}{Wc}\frac{\partial Wc}{\partial M} = 1 - \frac{(\gamma + 1) \cdot M^2}{2 \cdot (1 + \frac{\gamma - 1}{2} M^2)}$$

$$\frac{\gamma}{Wc}\frac{\partial Wc}{\partial \gamma}=\frac{1}{2}-\gamma\left[\frac{1}{4}\cdot\frac{\gamma+1}{\gamma-1}\frac{M^2}{(1+\frac{\gamma-1}{\gamma}M^2)}-\frac{\ln(1+\frac{\gamma-1}{2}M^2)}{(\gamma-1)^2}\right]$$

Mach Number Uncertainty:

$$(\frac{U_M}{M})^2=\left(\frac{P_t}{M}\frac{\partial M}{\partial P_t}\right)^2(\frac{U_{Pt}}{P_t})^2+\left(\frac{P_s}{M}\frac{\partial M}{\partial P_s}\right)^2(\frac{U_{Ps}}{P_s})^2$$

$$\frac{P_t}{M}\frac{\partial M}{\partial P_t}=\frac{1}{2}\frac{\gamma-1}{\left(\frac{P_t}{P_s}\right)^{\frac{\gamma-1}{\gamma}}-1}\frac{\left(\frac{P_t}{P_s}\right)^{\frac{\gamma-1}{\gamma}}}{\gamma};\qquad \frac{P_s}{M}\frac{\partial M}{\partial P_s}=\frac{-1}{2}\frac{\gamma-1}{\left(\frac{P_t}{P_s}\right)^{\frac{\gamma-1}{\gamma}}-1}\frac{\left(\frac{P_t}{P_s}\right)^{\frac{\gamma-1}{\gamma}}}{\gamma}$$

$$\frac{\gamma}{M}\frac{\partial M}{\partial \gamma}=\frac{\gamma}{2}\frac{\gamma-1}{\left(\frac{P_t}{P_s}\right)^{\frac{\gamma-1}{\gamma}}-1}\left[\frac{-1}{(\gamma-1)^2}\left(\left(\frac{P_t}{P_s}\right)^{\frac{\gamma-1}{\gamma}}-1\right)+\frac{1}{\gamma^2(\gamma-1)}\left(\frac{P_t}{P_s}\right)^{\frac{\gamma-1}{\gamma}}\ln\left(\frac{P_t}{P_s}\right)\right]$$

Thus, the analytical expression for the uncertainty in the corrected flow measurement is:

$$(\frac{U_{Wc}}{Wc})^2=\left[1-\frac{(\gamma+1)\cdot M^2}{2\cdot(1+\frac{\gamma-1}{2}M^2)}\right]^2\cdot\left[\frac{1}{2}\frac{\gamma-1}{\left(\frac{P_t}{P_s}\right)^{\frac{\gamma-1}{\gamma}}-1}\frac{\left(\frac{P_t}{P_s}\right)^{\frac{\gamma-1}{\gamma}}}{\gamma}\right]^2\left(\frac{U_{Pt}}{P_t}\right)^2+\ldots$$

$$\left[1-\frac{(\gamma+1)\cdot M^2}{2\cdot(1+\frac{\gamma-1}{2}M^2)}\right]^2\cdot\left[-\frac{1}{2}\frac{\gamma-1}{\left(\frac{P_t}{P_s}\right)^{\frac{\gamma-1}{\gamma}}-1}\frac{\left(\frac{P_t}{P_s}\right)^{\frac{\gamma-1}{\gamma}}}{\gamma}\right]^2\left(\frac{U_{Ps}}{P_s}\right)^2+\ldots$$

$$\left[\left(\frac{1}{2}-\gamma\left[\frac{1}{4}\cdot\frac{\gamma+1}{\gamma-1}\frac{M^2}{(1+\frac{\gamma-1}{\gamma}M^2)}-\frac{\ln(1+\frac{\gamma-1}{2}M^2)}{(\gamma-1)^2}\right]\right)^2+\ldots\right.$$

$$\left.\left(1-\frac{(\gamma+1)\cdot M^2}{2\cdot(1+\frac{\gamma-1}{2}M^2)}\right)^2\cdot\left(\frac{\gamma}{2}\frac{\gamma-1}{\left(\frac{P_t}{P_s}\right)^{\frac{\gamma-1}{\gamma}}-1}\left[\frac{-1}{(\gamma-1)^2}\left(\left(\frac{P_t}{P_s}\right)^{\frac{\gamma-1}{\gamma}}-1\right)+\frac{1}{\gamma^2(\gamma-1)}\left(\frac{P_t}{P_s}\right)^{\frac{\gamma-1}{\gamma}}\ln\left(\frac{P_t}{P_s}\right)\right]\right)^2\right]\left(\frac{U_\gamma}{\gamma}\right)^2$$

Uncertainty Propagation in Adiabatic Efficiency

As with the corrected flow uncertainty analysis the fluid is also considered to be an ideal gas for this analysis

The expression for adiabatic efficiency when the flow is an ideal gas, and properties are assumed constant:

$$\eta = \frac{\pi^{\frac{\gamma-1}{\gamma}} - 1}{\tau - 1}$$

η - adiabatic efficiency,
τ - total temperature ratio,
π - total pressure ratio,
γ - ratio of specific heats

The absolute uncertainty in the adiabatic efficiency is:

$$U_\eta^2 = \left(\pi \frac{\partial \eta}{\partial \pi}\right)^2 \left(\frac{U_\pi}{\pi}\right)^2 + \left(\tau \frac{\partial \eta}{\partial \tau}\right)^2 \left(\frac{U_\tau}{\tau}\right)^2 + \left(\gamma \frac{\partial \eta}{\partial \gamma}\right)^2 \left(\frac{U_\gamma}{\gamma}\right)^2$$

Taking the derivatives:

$$\frac{\partial \eta}{\partial \pi} = \frac{\gamma - 1}{\gamma(\tau - 1)} \cdot \pi^{\frac{-1}{\gamma}}, \qquad \frac{\partial \eta}{\partial \tau} = \frac{1 - \pi^{\frac{\gamma-1}{\gamma}}}{(\tau - 1)^2}, \qquad \frac{\partial \eta}{\partial \gamma} = \frac{\pi^{\frac{\gamma-1}{\gamma}} \ln(\pi)}{\gamma^2(\tau - 1)}$$

Relating temperature ratio and pressure ratio to upstream and downstream measurements:

$$\left(\frac{U_\pi}{\pi}\right)^2 = \left(\frac{U_{Pup}}{Pup}\right)^2 + \left(\frac{U_{Pdn}}{Pdn}\right)^2$$

$$\left(\frac{U_\tau}{\tau}\right)^2 = \left(\frac{U_{Tup}}{Tup}\right)^2 + \left(\frac{U_{Tdn}}{Tdn}\right)^2$$

Thus

$$U_\eta^2 = \left(\pi \cdot \frac{\gamma - 1}{\gamma \cdot (\tau - 1)} \cdot \pi^{\frac{-1}{\gamma}}\right)^2 \cdot \left(\left(\frac{U_{PtUp}}{Pt_{Up}}\right)^2 + \left(\frac{U_{PtDn}}{Pt_{Dn}}\right)^2\right) \ldots$$

$$+ \left(\tau \cdot \frac{1 - \pi^{\frac{\gamma-1}{\gamma}}}{(\tau - 1)^2}\right)^2 \cdot \left(\left(\frac{U_{TtUp}}{Tt_{Up}}\right)^2 + \left(\frac{U_{TtDn}}{Tt_{Dn}}\right)^2\right) + \left(\frac{\pi^{\frac{\gamma-1}{\gamma}} \cdot \ln(\pi)}{\gamma \cdot (\tau - 1)}\right)^2 \cdot \left(\frac{U_\gamma}{\gamma}\right)^2$$

Uncertainty Propagation in Corrected Speed

Corrected Speed is defined as:

$$Nc = \frac{N \cdot \pi \cdot D}{\sqrt{R_g \cdot T_t}}$$

Taking the derivatives, and plugging into the equations for Relative Uncertainty yields

$$\left(\frac{U_{Nc}}{Nc}\right)^2 = \left(\frac{U_N}{N}\right)^2 + \frac{1}{4}\left(\frac{U_{Tt}}{T_t}\right)^2 + \frac{1}{4}\left(\frac{U_{Rg}}{R_g}\right)^2$$

The uncertainty in the speed measurement is due to quantization error in the 80 MHz counter cards.

At full speed the relative error in the speed measurement is ~2.7×10^{-6} for Rotor One and ~2.3×10^{-6} for Rotor Two.

Appendix C: Measurement Uncertainties

Pressure Uncertainties that Result form Probe Geometry

Values based on Equations 5.2 and 5.3

Table C.1: Relative uncertainties in pressure measurements due to probe geometry

			Relative Uncertainties		
Run	Inlet Mach	Exit Mach	Up Pt	Up Ps	Down Pt
005	0.535	0.441	0.17%	0.14%	0.26%
006	0.492	0.439	0.17%	0.14%	0.21%
007	0.425	0.429	0.16%	0.13%	0.15%
008	0.424	0.451	0.18%	0.15%	0.15%
009	0.432	0.519	0.24%	0.19%	0.16%
010	0.436	0.521	0.24%	0.19%	0.16%
011	0.433	0.485	0.21%	0.17%	0.16%
013	0.456	0.570	0.30%	0.23%	0.18%
014	0.478	0.593	0.32%	0.25%	0.20%

Pressure Transducer Qualification

After the tests where run the pressure transducers were calibrated to check their linearity. This was done by evacuating the system taking data for 60 seconds at vacuum then venting atmospheric air in. The venting in process was done in steps. The Heise 015 was used as the standard during the calibration, after the indicated Heise 015 pressure was steady to with 0.001 psi for greater than 40 seconds more air was let into the facility to move to the next calibration point. Figure C.1 shows the Heise pressure during the entire qualification test. The range of the qualification was limited to vacuum to 1 atm because 15 psi is the maximum rated pressure difference across the upstream transducers. This meant that although the upstream transducers were qualified over their entire range the downstream transducers were only qualified for 1/3 of their range. The voltage data during the time the Heise reading was constant was averaged to find the transducer non-linearity for that point, the standard deviation of that data, labeled as 'noise' was assumed to be the uncertainty due to noise of the transducer and the signal conditioners. This data is listed in Tables C.2 and C.3.

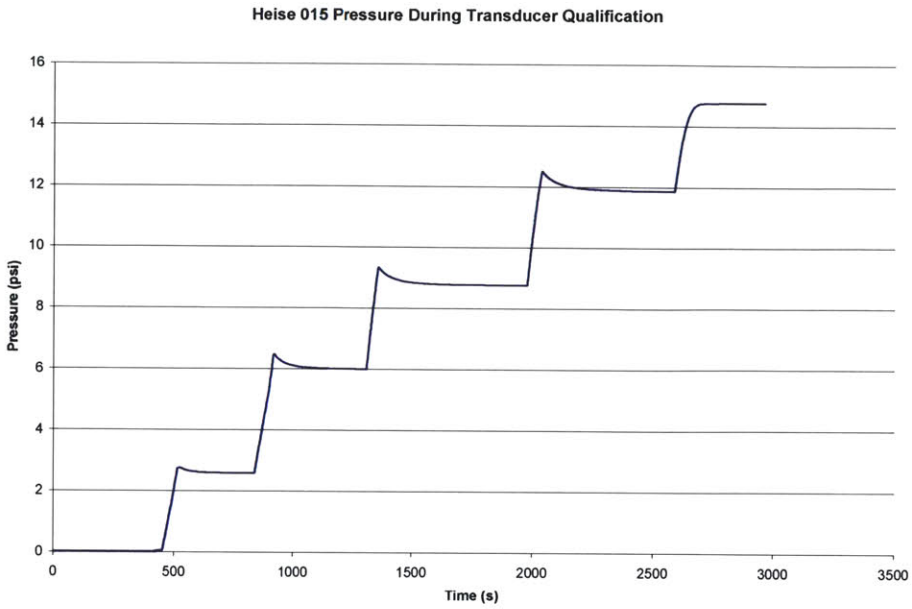

Figure C.1: Pressure history of Heise 015 during transducer qualification

Table C.2: Qualification Data For Upstream Pressure Transducers

Upstream Transducer Uncertainties		
Name	**Linearity**	**Noise**
PT0A	0.12%	0.77%
PT1A	0.10%	0.35%
PDMP	0.50%	0.10%
PT2ZR01	0.12%	0.14%
PT2ZR02	0.16%	0.17%
PPT2C	0.15%	0.20%
PT2ZR04	0.09%	0.17%
PT2ZR05	0.11%	0.15%
PPS2C	0.12%	0.24%
PT2ZR07	0.12%	0.24%
PT2ZR08	0.14%	0.15%
PT2A	0.27%	0.19%
PS2A	0.10%	0.30%
PPT2A	0.14%	0.33%
PPS2A	0.16%	0.28%
PT2B	0.12%	0.13%
PS2B	0.12%	0.33%
PT2C	0.10%	0.15%
PS2C	0.11%	0.11%
PW1	0.09%	0.14%
PPT2B	0.09%	0.15%
PPS2B	0.09%	0.16%
Average	**0.14%**	**0.22%**

Table C.3: Qualification Data for Downstream Pressure Transducers

Down Stream Transducer Uncertainties		
Name	**Linearity**	**Noise**
PT5A	0.05%	0.91%
PPT5A	0.06%	0.16%
PPS5A	0.02%	0.16%
PT5ZR01	0.06%	0.20%
PT5ZR02	0.02%	0.31%
PT5ZR03	0.03%	0.23%
PT5ZR04	0.08%	0.32%
PT5ZR05	0.06%	0.37%
PT5CR01	0.16%	0.19%
PT5CR02	0.13%	0.18%
PT5CR03	1.11%	0.49%
PT5CR04	0.18%	0.14%
PT5CR05	0.10%	0.24%
PS3HS	0.13%	0.47%
PS5AHS	0.09%	0.14%
Average	**0.15%**	**0.30%**

Summary of Pressure Uncertainties

Table C.4: Up Stream Total Pressure Uncertainty

Total Upstream Total Pressure Uncertainty				
Run	**Head Loss**	**Linearity**	**Noise**	**Total**
005	0.17%	0.12%	0.18%	0.28%
006	0.17%	0.12%	0.18%	0.28%
007	0.16%	0.12%	0.18%	0.27%
008	0.18%	0.12%	0.18%	0.28%
009	0.24%	0.12%	0.18%	0.33%
010	0.24%	0.12%	0.18%	0.33%
011	0.21%	0.12%	0.18%	0.30%
013	0.30%	0.12%	0.18%	0.37%
014	0.32%	0.12%	0.18%	0.39%

Table C.5: Down Stream Total Pressure Uncertainty

Total Down Stream Total Pressure Uncertainty				
Run	Head Loss	Linearity	Noise	Total
005	0.26%	0.19%	0.27%	0.42%
006	0.21%	0.19%	0.27%	0.39%
007	0.15%	0.19%	0.27%	0.36%
008	0.15%	0.19%	0.27%	0.36%
009	0.16%	0.19%	0.27%	0.37%
010	0.16%	0.19%	0.27%	0.37%
011	0.16%	0.19%	0.27%	0.37%
013	0.18%	0.19%	0.27%	0.38%
014	0.20%	0.19%	0.27%	0.38%

Table C.6: Up Stream Static Pressure Uncertainty

Total Upstream Static Pressure Uncertainty				
Run	Head Loss	Linearity	Noise	Total
005	0.14%	0.13%	0.21%	0.29%
006	0.14%	0.13%	0.21%	0.28%
007	0.13%	0.13%	0.21%	0.28%
008	0.15%	0.13%	0.21%	0.29%
009	0.19%	0.13%	0.21%	0.32%
010	0.19%	0.13%	0.21%	0.32%
011	0.17%	0.13%	0.21%	0.30%
013	0.23%	0.13%	0.21%	0.34%
014	0.25%	0.13%	0.21%	0.35%

Summary of Temperature Uncertainties

The sources of these uncertainties are discussed in detail in "Aerodynamic Performance Measurements in a Counter-Rotating Aspirated Compressor" [5]

Table C.7: Summary of Absolute Temperature Uncertainty

Sensor Name	Uncertainty (K)				
	Recovery	Conduction	Radiation	Calibration	Total
TCKSU001	0.025	0.005	0.112	0.048	0.124
TCKSU002	0.025	0.005	0.112	0.058	0.129
TCKSU007	0.025	0.005	0.112	0.055	0.127
TCKRU001	0.025	0.073	0.112	0.041	0.142
TCKRU002	0.025	0.073	0.112	0.038	0.141
TCKRU003	0.025	0.073	0.112	0.04	0.142
TCKRU004	0.025	0.073	0.112	0.039	0.141
TCKRU005	0.025	0.073	0.112	0.042	0.142
TCKRU006	0.025	0.073	0.112	0.04	0.142
TCKRU007	0.025	0.073	0.112	0.038	0.141
TCKRU008	0.025	0.073	0.112	0.039	0.141
TCKRU009	0.025	0.073	0.112	0.039	0.141
TCKRU010	0.025	0.073	0.112	0.043	0.143
TCKRU011	0.025	0.073	0.112	0.042	0.142
TCKSD001	0.0065	0.0005	0.299	0.071	0.307
TCKSD002	0.0065	0.0005	0.299	0.036	0.301
TCKSD003	0.0065	0.0005	0.299	0.065	0.306
TCKRD001	0.0065	0.014	0.299	0.033	0.301
TCKRD002	0.0065	0.014	0.299	0.028	0.301
TCKRD003	0.0065	0.014	0.299	0.034	0.301
TCKRD004	0.0065	0.014	0.299	0.034	0.301
TCKRD005	0.0065	0.014	0.299	0.037	0.302
TCKRD006	0.0065	0.014	0.299	0.06	0.305
TCKRD007	0.0065	0.014	0.299	0.326	0.443
TCKRD008	0.0065	0.014	0.299	0.054	0.304
TCKRD009	0.0065	0.014	0.299	0.047	0.303
TCKRD010	0.0065	0.014	0.299	0.062	0.306
TCKRD011	0.0065	0.014	0.299	0.097	0.315

Summary of Gas Mixture Uncertainties

For all the reported performance values the gas tables that are used assume that the gas mixture is the design gas mixture. The gases are mixed in the supply tank by partial pressures. The gases are at room temperature while mixing and pressures do not exceed 2 atm thus the gases are assumed to be ideal and the mole fraction of each gas is the same as its partial pressure in the mixture. The uncertainty in γ and R_g is assumed to be the same as the error in the mole fraction of the mixture compared to the design mole fraction. This uncertainty is summarized in Table C.8

Table C.8: Uncertainty in gas mixture

Run	First gas filled	P 1st (psia)	Final P (psia)	X CO2	X Ar	Absolute Error in Mixture
005	CO2	16.750	34.140	49.06%	50.94%	0.15%
006	CO2	16.820	34.280	49.07%	50.93%	0.16%
007	CO2	16.820	34.230	49.14%	50.86%	0.23%
008	Ar	19.910	38.750	48.62%	51.38%	0.29%
009	CO2	16.840	34.410	48.94%	51.06%	0.03%
010	CO2	14.280	29.110	49.06%	50.94%	0.15%
011	CO2	14.320	29.270	48.92%	51.08%	0.01%
013	CO2	14.380	29.370	48.96%	51.04%	0.05%
014	CO2	14.300	29.180	49.01%	50.99%	0.10%

Appendix D: Blowdown Test Details

Sequence of Test Operations

1. Check Facility
   1.1. Verify that everything is sealed, instruments in place, throttle set correctly
2. Pull Vacuum
   2.1. Verify that the cooling water for the pump is on.
   2.2. Verify that the facility is approaching vacuum at the appropriate rate and there are no leaks.
   2.3. Turn on reference vacuum pump
      2.3.1. verify that pressure transducers respond when back pressure is swapped from vacuum to atmosphere
      2.3.2. verify that all transducers operate within the voltage range of the A/D
3. Perform Pre-Fill Calibrations
   3.1. Details of calibration procedures follow
4. Turn on water and heaters for gas fill system heat exchangers
   4.1. Ensure that the drive motors and water heaters are not on at the same time
5. Open appropriate valves on the CO_2 and the Ar bottle farms
6. Use pressure from an Ar bottle to hold the fast-acting valve closed with ~200 psi
7. Fill the supply tank to a value greater than the desired initial pressure
   7.1. Fill first with CO_2, after reaching desired pressure wait until the output of the Heise 150 is constant for at least 1 minute
      7.1.1. Record the supply tank pressure and temperature
   7.2. Fill with Ar to a value that is calculated based on the filled CO_2 pressure
      7.2.1. Record pressure after the Heise 150 is constant for at least 1 minute, multiple fills might be required to get the design mixture ratio
8. Perform Post-Fill Calibrations
9. Open the A/D program and the motor control program
   9.1. Input and double check appropriate variables for each
10. Arm the fast-acting valve with ~600 psi of pressure
    10.1. If there is a problem while accelerating the rotors firing the valve will decelerate the rotors faster than the motor drives can brake them
11. Begin accelerating the rotors
12. With the A/D program begin logging 'pre-test data'
13. While the rotors are spinning vent the supply tank until it is at the desired initial pressure and record ambient temperatures and pressures
14. Once both rotors are at the set speed set them both to 'coast' and immediately fire the valve
15. After ~5 seconds use the motor drives to brake the rotors
16. ~5 minutes after the rotors have stopped spinning perform the Post-Test Calibrations
17. "Safe" the facility
    17.1. Vent system to atm or begin pulling vacuum for next test
    17.2. Close all valves on the bottle farms
    17.3. Depressurize the fast-acting valve
    17.4. Turn off power to motor drives

Calibration Method

Two point calibrations of each pressure transducer occur three times during each test. The calibrations occur before the supply tank is filled (Pre-Fill Cal), with the entire tunnel in vacuum; after the supply tank is filled (Post-Fill Cal), with every transducer except for the supply tank transducers in vacuum; and several minutes after the test (Post-Test Cal), with the entire tunnel at one pressure level somewhere between vacuum and atmospheric. During all of these calibrations the pressure in the dump tank and the supply tank is measured with Heise absolute pressure transducers that were calibrated to be accurate to 0.15% of their range. The two pressure difference points are created by opening a valve that switches the reference pressure from vacuum to atmosphere. The reference vacuum pressure is measured using a Varian Type 053 Vacuum Gauge and atmospheric pressure in the lab is measured right before the calibration by switching the dump tank Heise from the dump tank to atmospheric.

In addition to the Heise absolute transducers two SensoTec absolute pressure transducers are supply and dump tanks and attached to the same A/D card as the other pressure transducers. There are 100 ms between when the A/D system starts logging data and when the valve begins opening. Data from the SensoTecs is averaged during this time to establish the initial pressures in the facility. This information is then used with the scales calculated from the two points in the calibrations to establish a zero for each transducer.

Of the three calibrations only the Post-Test Cal calibrates the transducers in a manner similar to the operation range. During the Pre and Post-Fill Cals the calibration range is from zero to negative one atmosphere. These calibrations are used to check the stability of the transducers and as an extra check that all the transducers are responding before the test. When the data is reduced the scale and zero calculated from the Post-Test Cal are used.

Appendix E: Raw Data Documentation

This appendix documents the raw data for Run 013. Also documented are metrics for what is happening within the facility, more details on data reduction, and what happens after the test time.

Raw Data

Figure E.1 is the pressures of the supply tank (PT0A, STEC 150) and the total pressure in the valve (PT1A).

Figure E.2 is the mid-stream upstream single total pressure measurements.

Figure E.3 is the upstream static pressure measurements; wall taps and pitot.

Figure E.4 is the upstream total pressure rake measurements, for all rakes the probe numbered '1' is at the hub.

Figure E.5 is the upstream total temperature single measurements, the thermocouples are not calibrated below 212° K.

Figure E.6 is the upstream total temperature rake measurements, the thermocouples are not calibrated below 212° K.

Figure E.7 is the casing static pressure measurements. PS3HS is between the rotors and PS5AHS is behind Rotor Two.

Figure E.8 is the pitot probe in the middle of the downstream span.

Figure E.9 is the down stream total pressure measurements.

Figure E.10 is the downstream total temperature measurements.

Figure E.11 is the pressures in the dump tank, the STEC050 transducer is in a different location than PDMP, which explains the variation.

Figure E.12 is the pressure in the bleed flow.

Figure E.13 is the speeds of each rotor.

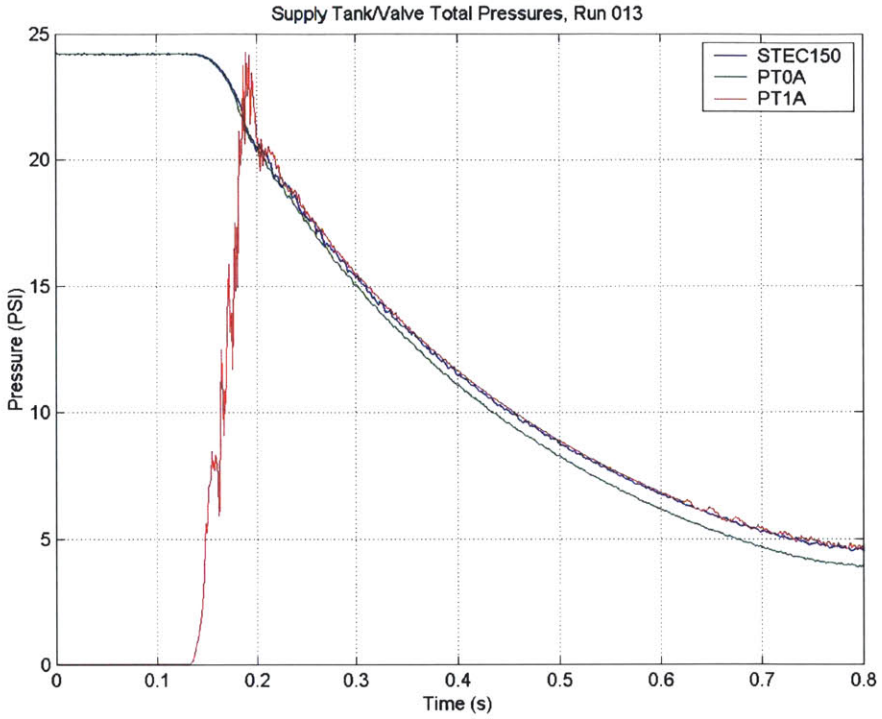

Figure E.1: Supply Tank Pressures, Run 013

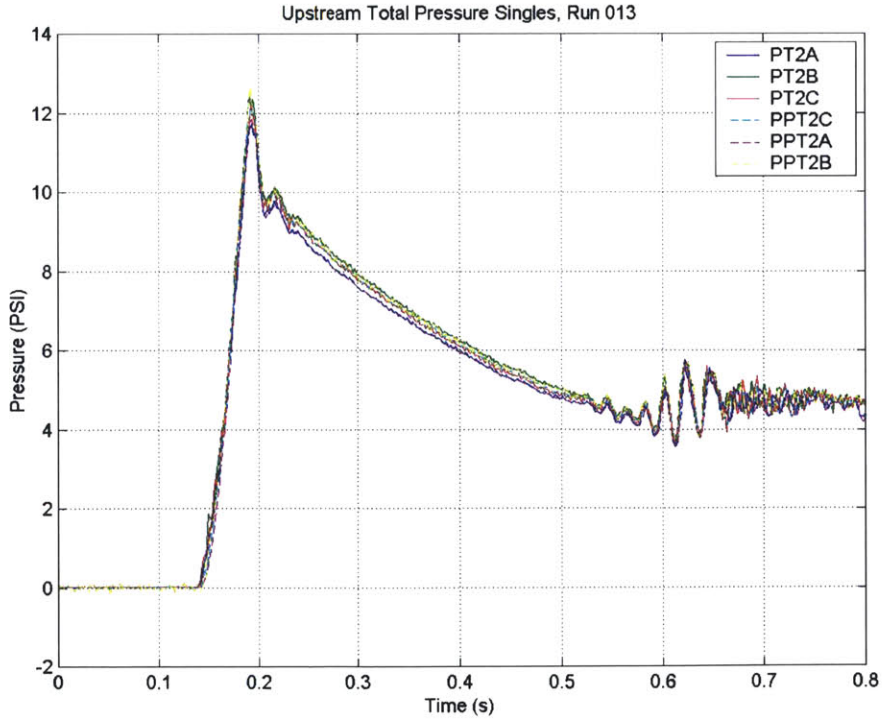

Figure E.2: Upstream Total Pressure Singles, Run 013

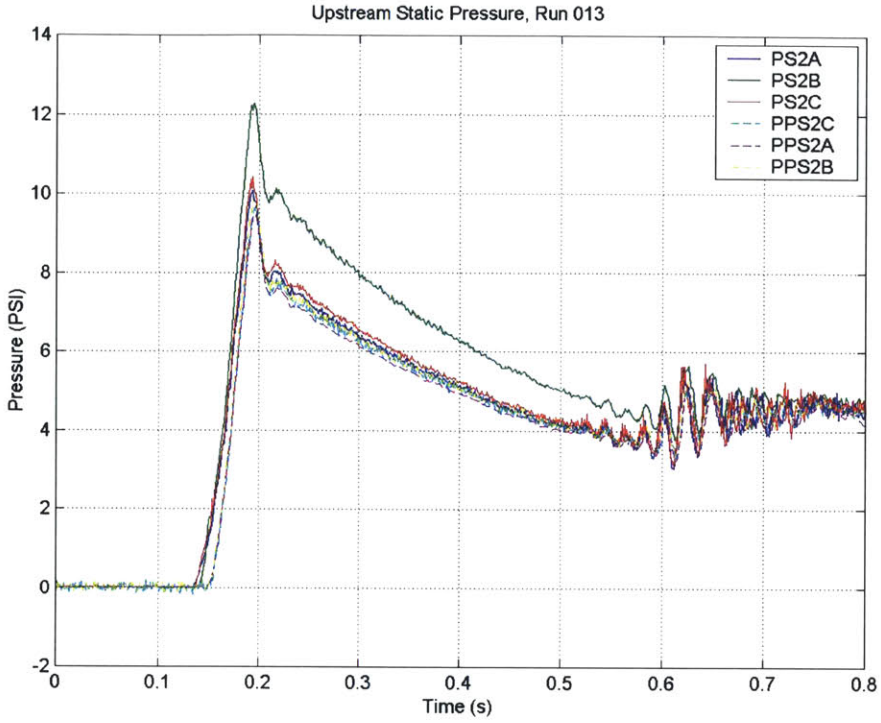

Figure E.3: Upstream Static Pressures, Run 013

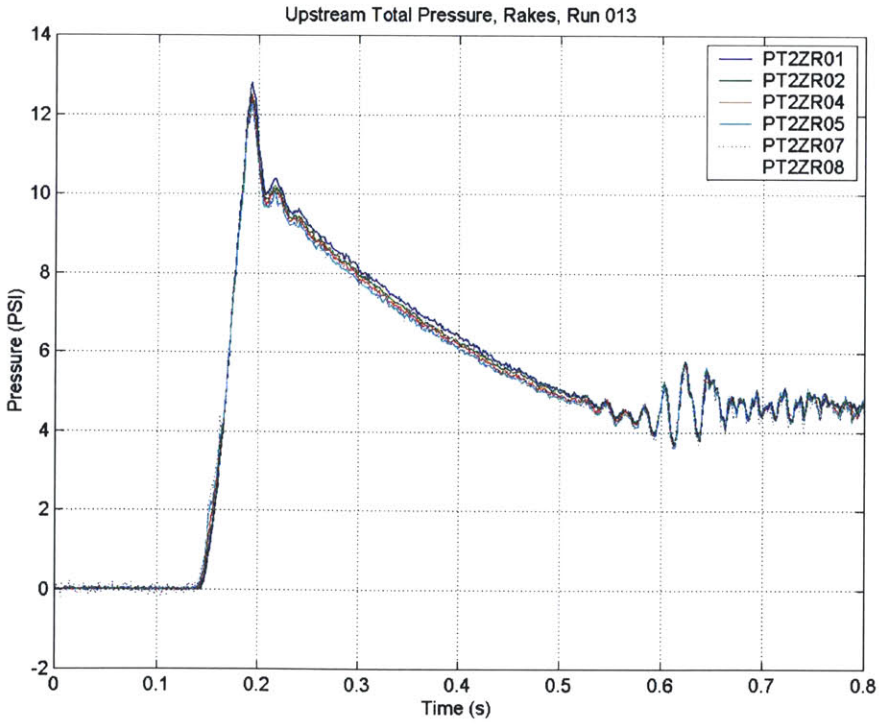

Figure E.4: Upstream Total Pressure, Rakes Run 013

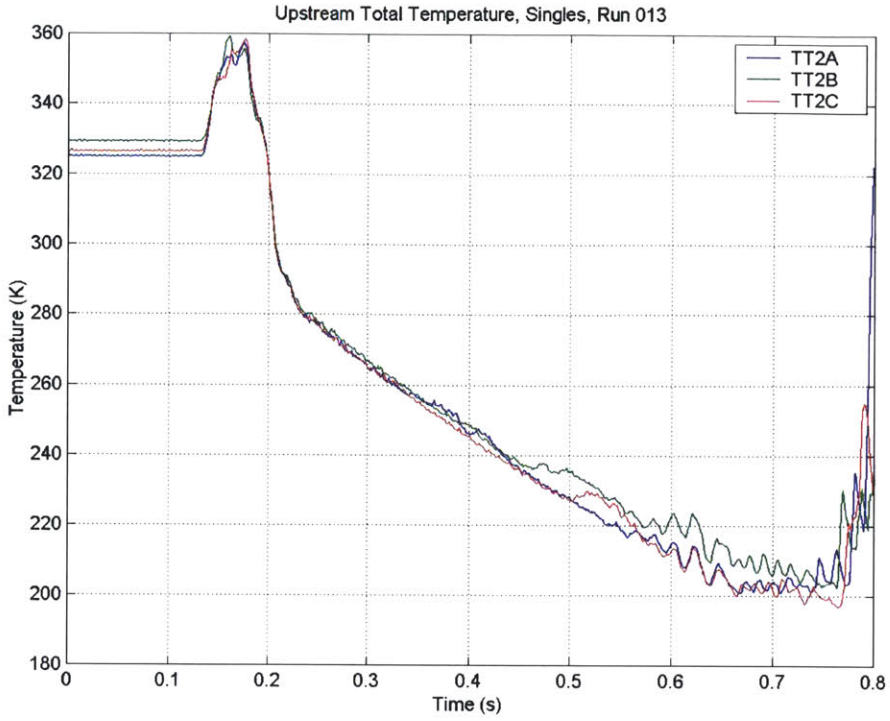

Figure E.5: Upstream Total Temperature Singles, Run 013

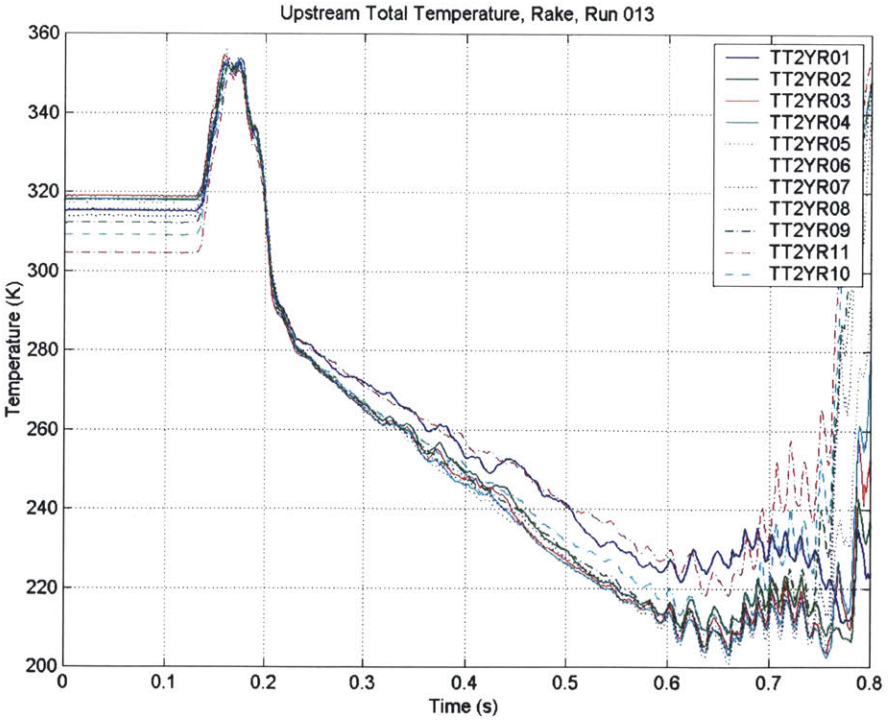

Figure E.6: Upstream Total Temperature Rake Measurements, Run 013

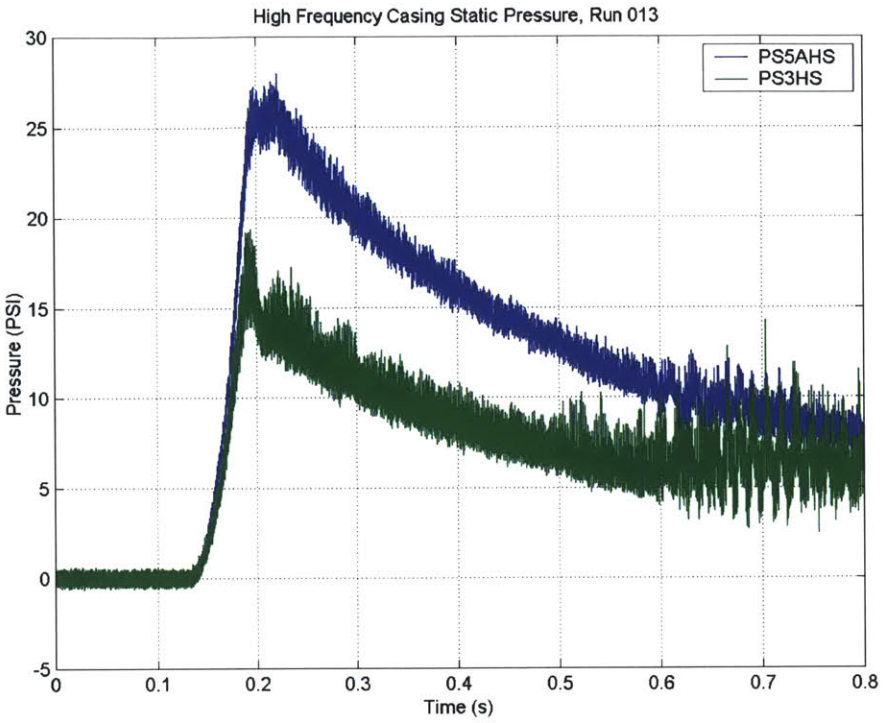

Figure E.7:High frequency casing static pressure measurements, Run 013

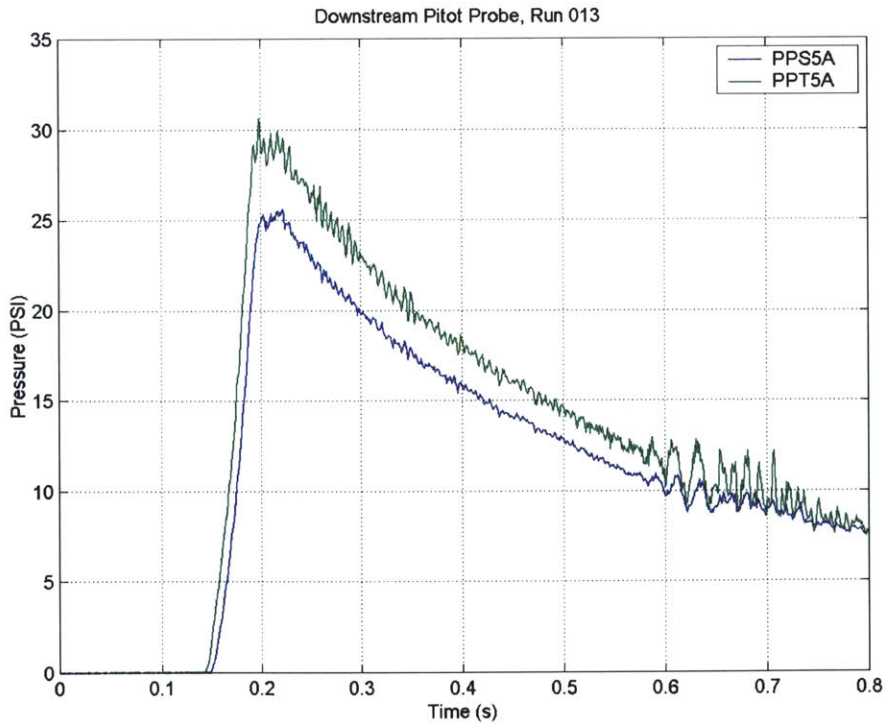

Figure E.8: Downstream mid-stream Pitot Probe, Run 013

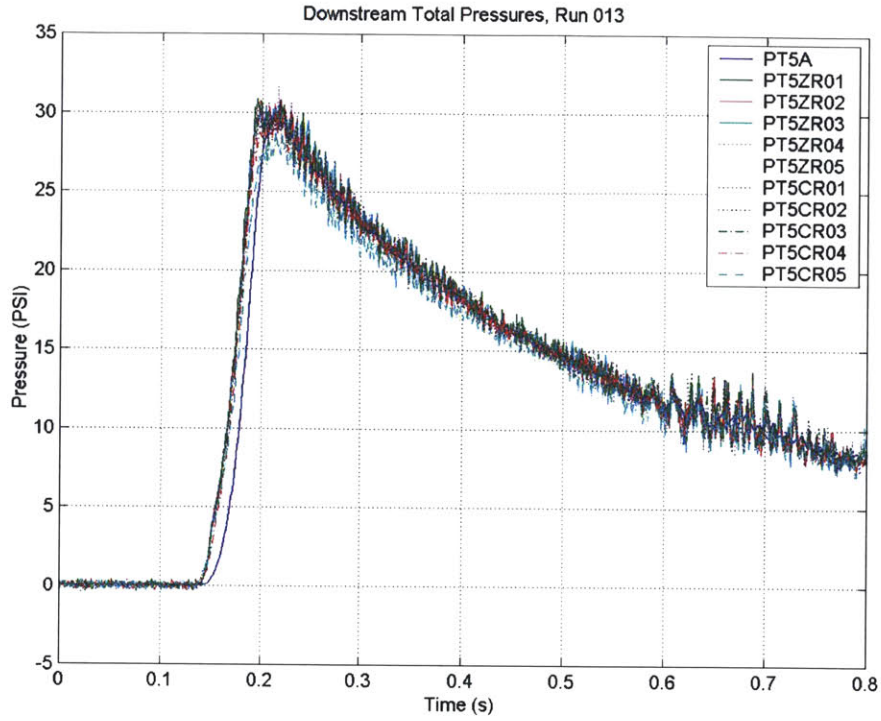

Figure E.9: Downstream Total Pressures, Run 013

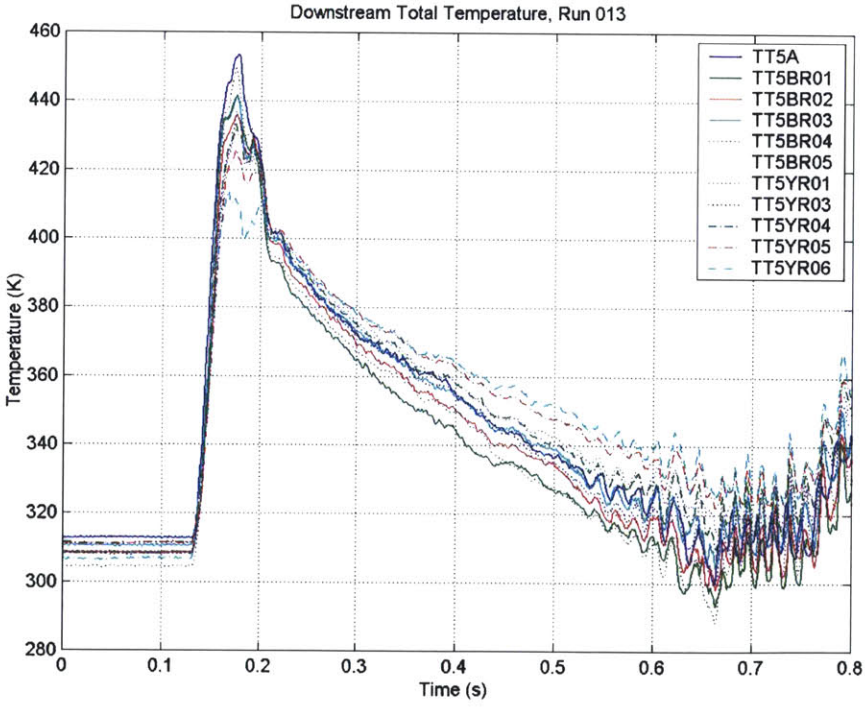

Figure E.10: Downstream Total Temperatures, Run 013

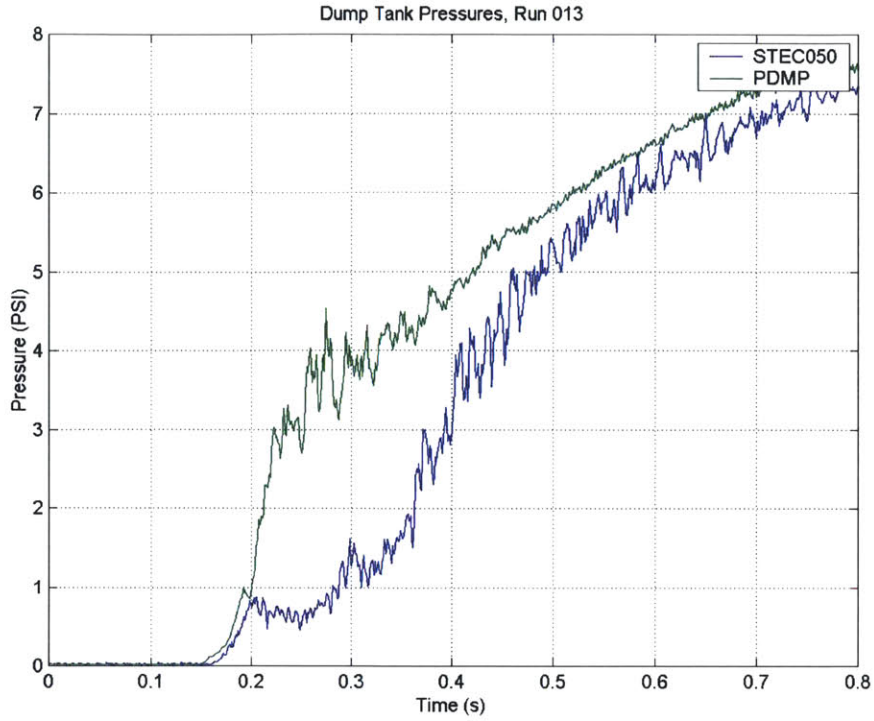

Figure E.11: Dump Tank Pressures, Run 013

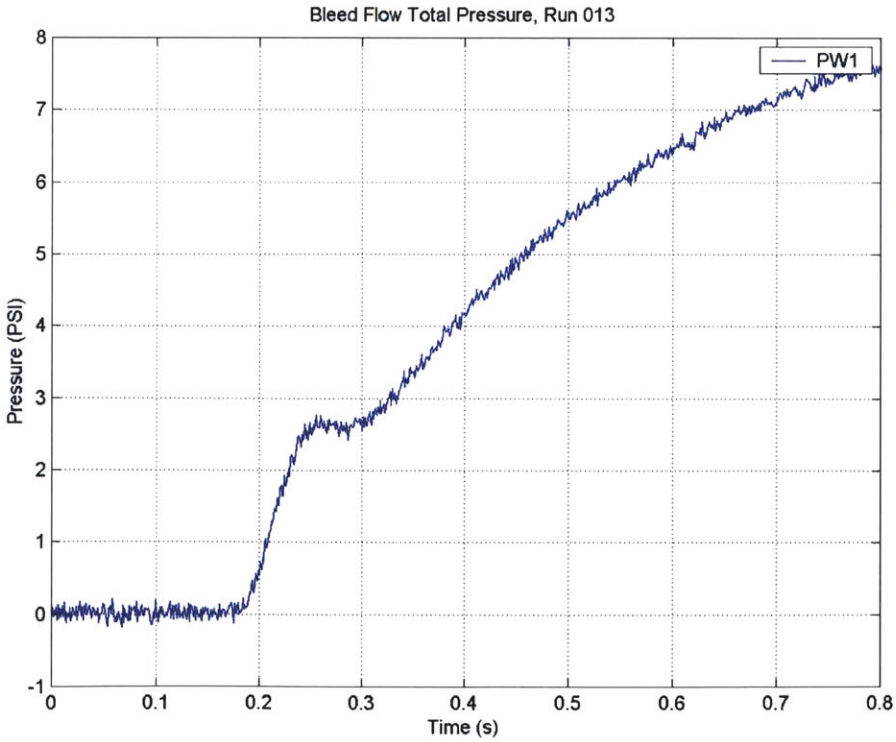

Figure E.12: Bleed Flow Total Pressure, Run 013

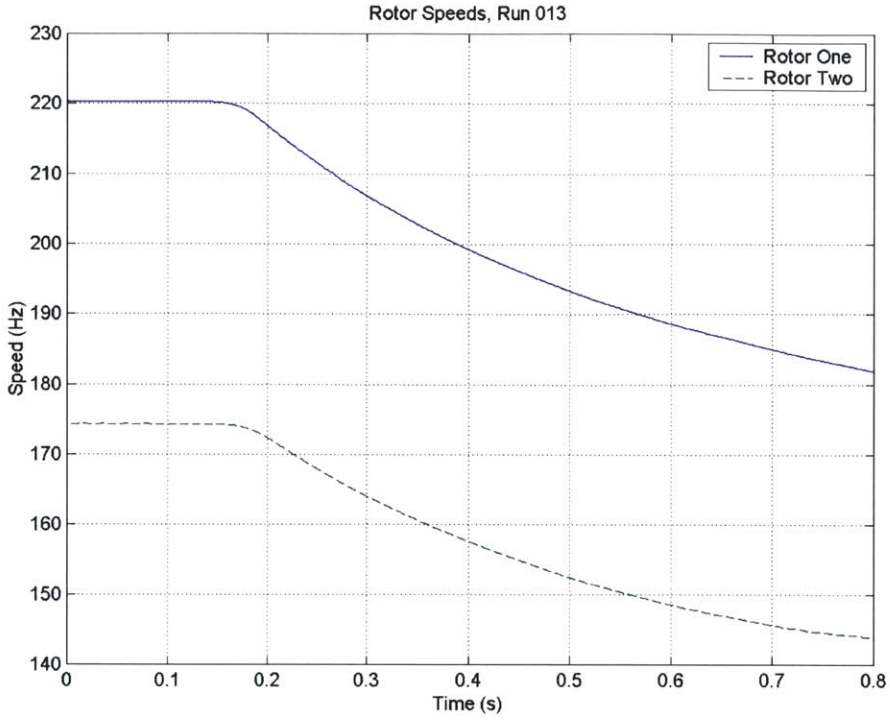

Figure E.13: Rotor speeds during Run 013

Facility Conditions & Test Time Selection

Figure E.14 is the corrected speeds of each rotor, normalized by the design corrected speeds. Figure E.15 is the corrected speeds during the test time. Between 250 ms and 350 ms the corrected speeds vary by less than 0.5% for Run 013. Constant corrected speed is one criteria when deciding what the test time is.

Figure E.16 is the pressure ratios across the screen, the pressure ratio across the screen, and the pressure ratio across the bleed flow passage (Rotor Two exit total pressure divided by the bleed passage total pressure). The horizontal line is the approximate minimum pressure ratio for choked flow. It was thought that while the throttle and screen were choked the corrected flow into the compressor would be constant. The pressure ratio across the bleed passage is currently the only way to make any statement about the bleed flow. As long as this passage is choked the corrected bleed flow should be constant. Figure E.17 is the entropy entering the compressor normalized by entropy at 250 ms. This plot verifies that the blowdown is occurring isentropically, as the model assumes, and that the instruments are well calibrated.

Selecting the 'test time' is arbitrary. The throttle must be choked, the corrected speeds must be constant to within some value (1% of the design was used), the initial compression wave must have passed and the upstream temperature of the gas must be

greater than 225° K. 250 ms to 350 ms was selected as a test time for each run because these parameters were met and using the same test time for each run simplified reduction and comparisons from one run to another.

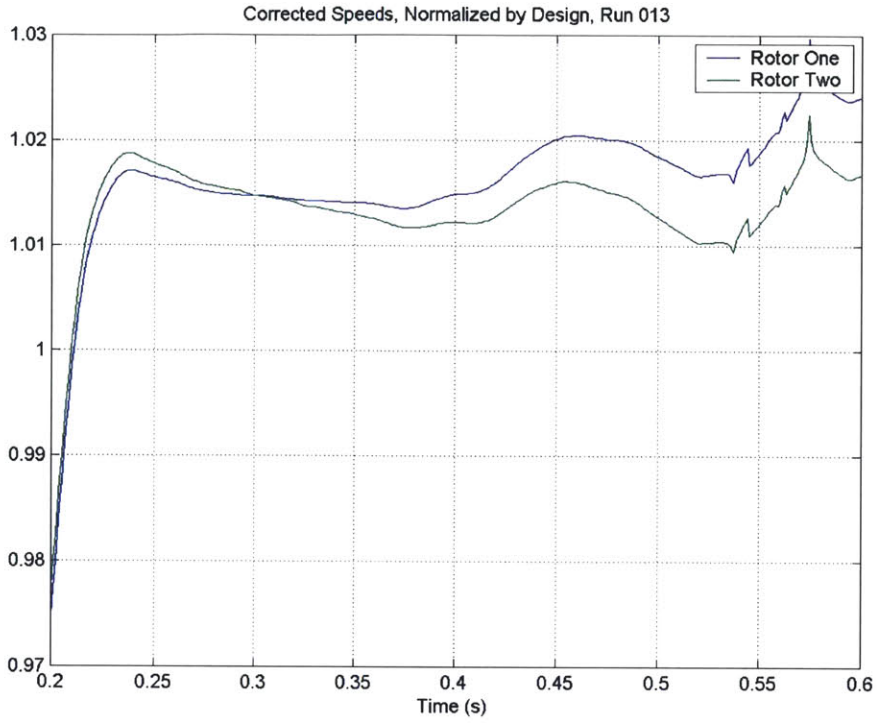

Figure E.14: Corrected Speeds During Run 013

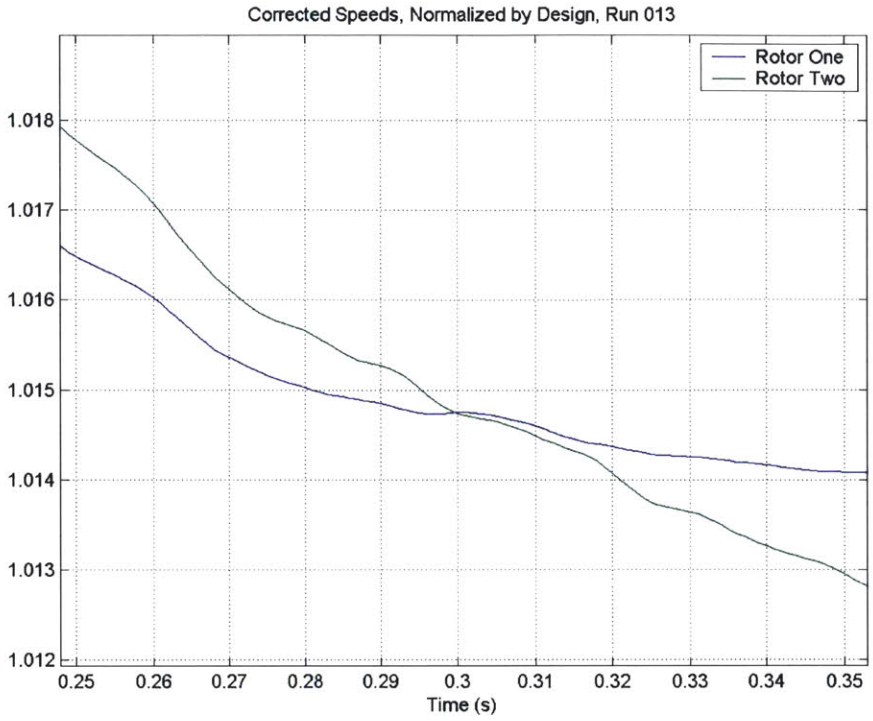

Figure E.15: Corrected speeds between 250 ms and 350 ms for Run 013

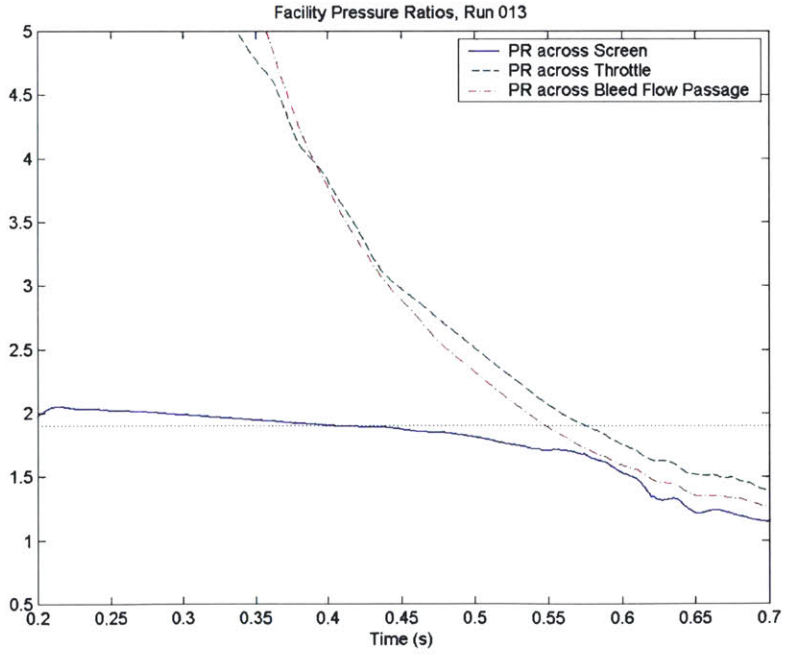

Figure E.16: Important pressure ratios in the facility for Run 013

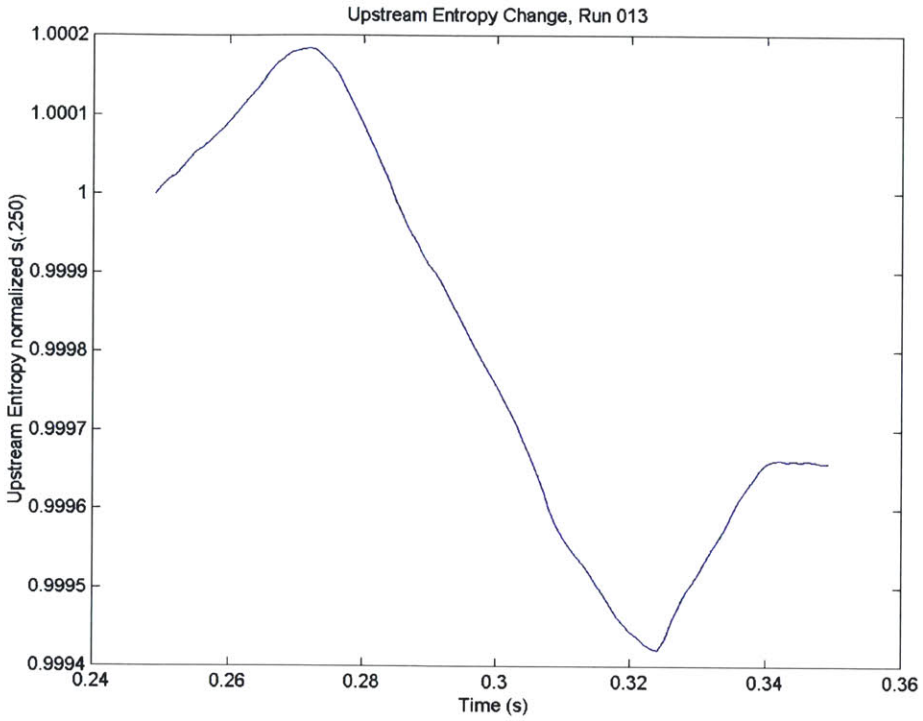

Figure E.17: Entropy entering Compressor, normalized by *s*(0.250), Run 013

Corrected Flow

When available the three upstream pitot probes are used to determine the corrected flow in each window in the manner described in Section 6.2.2. For each window the total temperature and total pressure are assumed to be constant radially and circumferentially. The average upstream conditions are determined by a mass flow weighted average of each of the window measurements. Figure E.18 through E.20 are the mass flow, corrected flow, and Mach number for each window during the test time. Also plotted is the mass flow weighted average value.

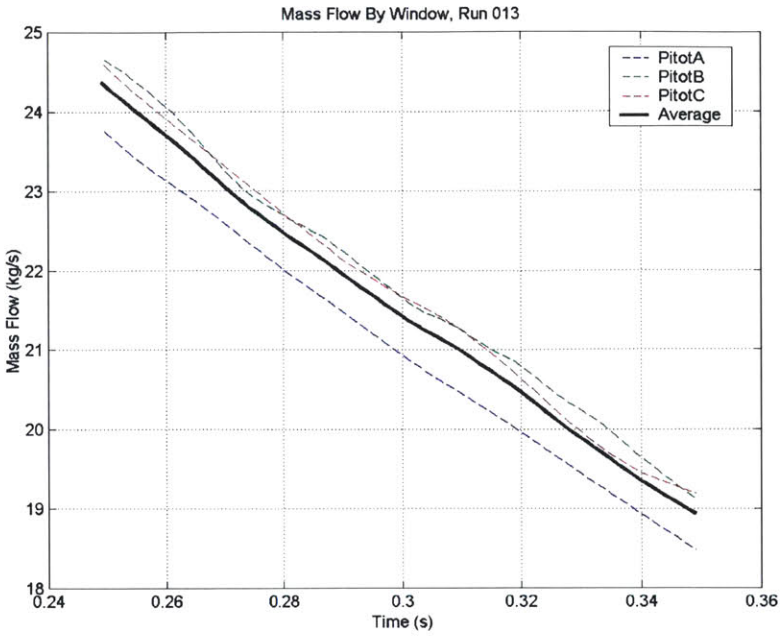

Figure E.18: Mass flow at each measurement location, Run 013

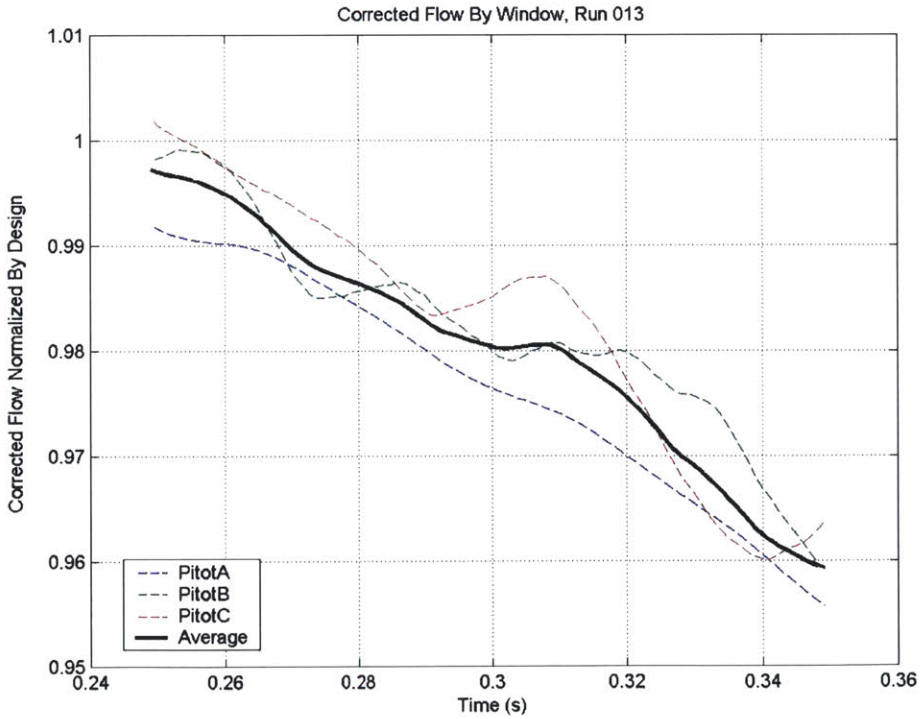

Figure E.19: Corrected flow normalized by the design value at each measurement location, Run 013

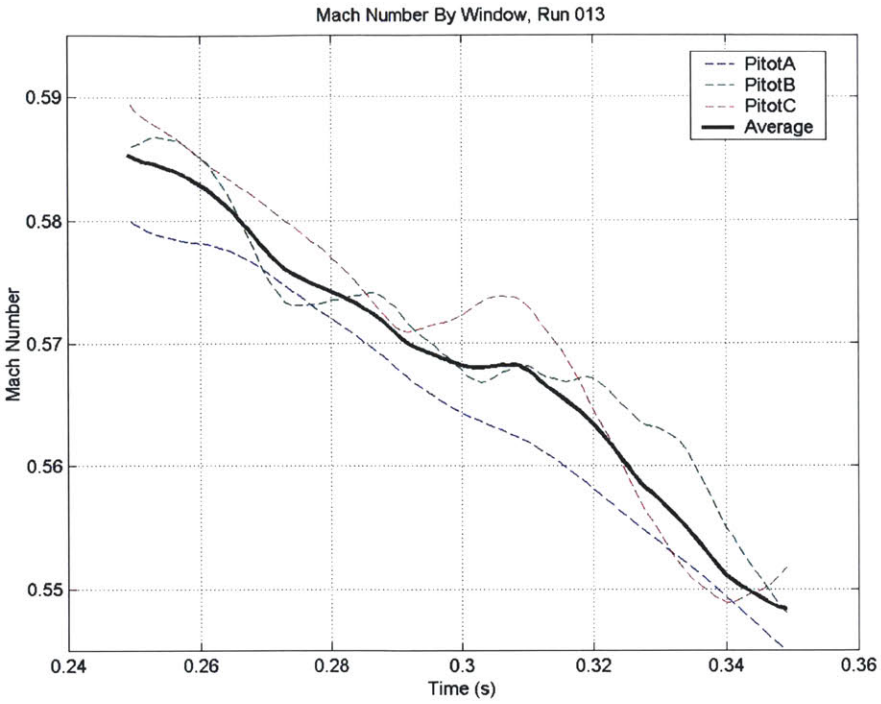

Figure E.20: Mach Number at each measurement location, Run 013

Pressure Ratio & Temperature Ratio

Figure E.21 is the pressure ratio and temperature ratio for Run 013 between 150 ms and 700 ms. After the initial transient the pressure ratio has a flat parabolic profile and around 500 ms the compressor begins to stall (the stall can be seen in Figure E.12).

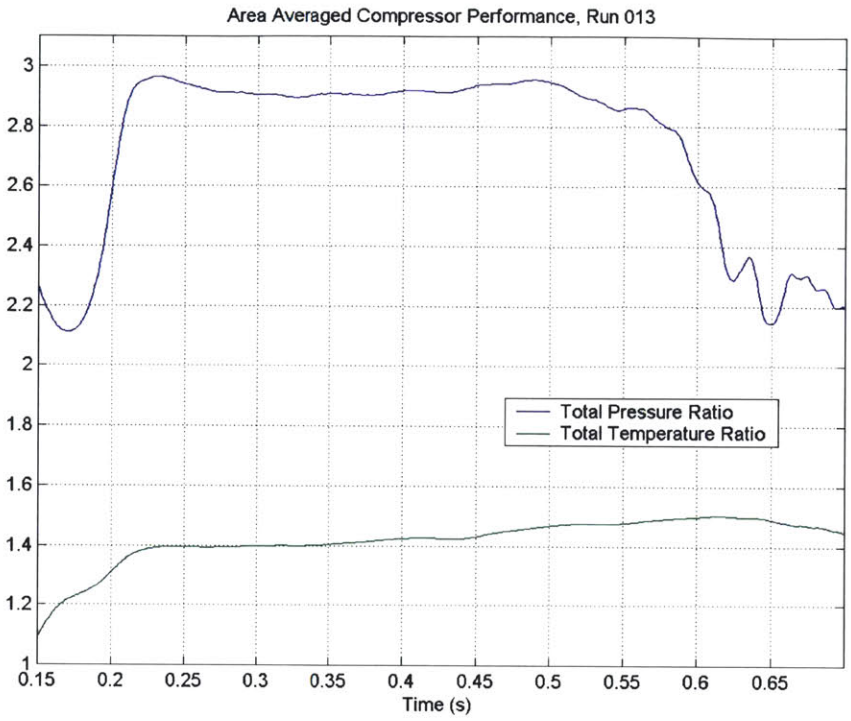

Figure E.21: Pressure Ratio and Temperature Ratio during Run 013

Figure E.22 shows the adiabatic efficiency, corrected flow normalized by the design value, and Reynolds' number normalized by the Reynolds' number used for analysis. The time range for the plotted data is shorter than that of Figure E.20 because below the lowest temperature of the NIST table is 250° K.

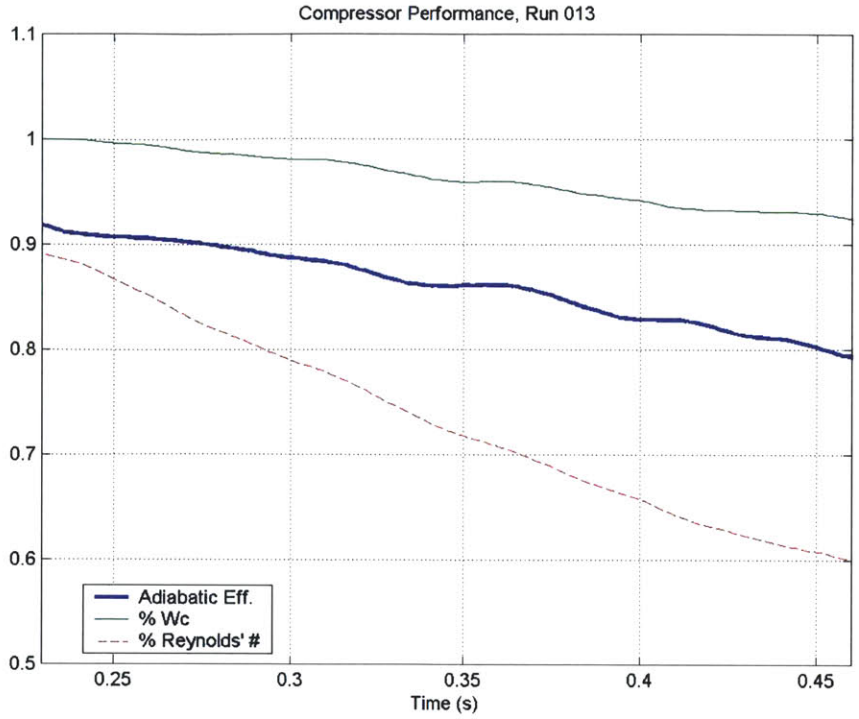

Figure E.22: Adiabatic efficiency, average inlet corrected flow, and inlet Reynolds' number for Run 013